An Iodine Based Thermal Optical Frequency Reference using NICE-OHMS Detection

June 30, 2016

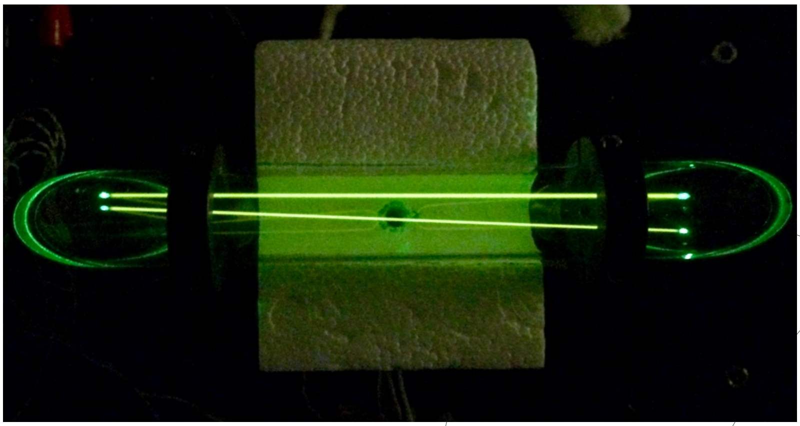

Niels Bohr Institute, University of Copenhagen

Author
Sigrid Skovbo Adsersen

Supervisor
Jan W. Thomsen

Contents

List of Figures

List of Tables

Abstract

The work presented in this thesis is dedicated to the construction of a thermal optical frequency reference based on iodine ($^{127}I_2$). The motivation for developing a simple and robust optical frequency reference is found in the demand for such systems in current space technology and high speed coherent optical commumunication. A fractional uncertainty of 8.6 $\times 10^{-12}$ at one second of integration and ultimately 3 $\times 10^{-15}$ has previously been achieved in iodine based frequency references. [3], [8]. The setup designed during the work presented in this thesis plans to further improve, and at least match, this uncertainty. The setup is designed to make use of cavity enhanced absorption spectroscopy followed by phase detection of the molecules. With our new experimental setup design it has been possible to conduct the measurements at pressures one to two orders of magnitude lower than in previous experiments with comparable sample sizes, thereby reducing the broadening effects originating from the pressure. A new cavity design supporting a large beam waist that will allow further reduction in pressure as well as eliminate the current system limitations arising from the transit time broadening. This setup is introduced and tested, along with the experimentally realized parameters. Furthermore, it is the first reported experiment to employ the NICE-OHMS detection scheme on iodine. The theoretical description of both the sample and the setup, along with the experimentally realized parameters, and suggestion for future improvements of the setup are presented. The preliminary measurements presented in this work were corrupted by an impure sample and a highly unstable laser. Correction to these have been employed and measurement results are expected in the near future.

Resumé

Denne afhandling er dedikeret til udviklingen af en termisk, iod-baseret ($^{127}I_2$), optisk frekvens reference. Motivationen bag udviklingen af et simpelt og robust frekvensreferencesystem findes blandt efterspørgslen efter sådanne systemer i den nuværende rumteknologi og højhasighed optisk kommunikation. En fraktionel usikkerhed på 8.6 $\times 10^{-12}$ integreret over 1 sekund og ultimativt 3 $\times 10^{-15}$ er tidligere opnået for iodbaserede frekvensreferencer [3], [8]. Det eksperimentelle design præsenteret i denne opgave er udviklet med henblik på at forbedre, og som minimum tilsvare, denne usikkerhed. Forsøgsopstillingen gør brug af kavitetsforbedret absorptionsspektroskopi efterfulgt af fasedetektion af molekylerne. Med vores nye forsøgsopstilling har det været muligt at udføre målingerne ved tryk der er en til to størrelsesordner lavere end i forsøg med lignende prøvestørrelser, og derved reducere de trykrelaterede forbredningseffekter. Et nyt kavitetsdesign der understøtter en bred stråle der vil muliggøre yderligere trykreduktioner, og desuden eliminere den nuværende begrænsende forbredningseffekt der stammer fra transittidsforbredningen. Denne opstilling introduceres og testes, og dets eksperimentelt realiserede parametre præsenteres. Endvidere er forsøget det første raporterede der gør brug af NICE-OHMS måleteknikken i iod. Den teoretiske beskrivelse af både prøven og forsøgsopstillingen præsenteres samt de eksperimentelt realiserede parametre, og forslag til fremtidige forbedringer. De foreløbige resultater har været præget af en forurenet prøvet og en højst ustabil laser. Forbedringer af disse er implementeret, og resultater fra forsøget forventes i den nærmeste fremtid.

Acknowledgements

When I first sat foot in the laboratory in the basement at the Niels Bohr Institute in the autumn of 2014, I had little idea of the challenge that layed ahead. In front of me stood an empty optical table, where I was to build a working optical clock within the span of a master thesis. And it turned out to be quite a challenge, with technical obstacles and challenges showing up. Without having much prior experience with hands-on experimental physics, I would like to express my deepest graditude towards the Quantum Metrology Group.

Martin Romme Henriksen has been an endless resource of guidance and support when it comes to building and understanding electrical circuits. His help has been essential in my personal skill development.

Stefan Alaric Schäffer was the first to introduce me to the difficult, yet exciting, reality of building optical cavities. Before the beginning of my masters, I had only encountered text book examples, but with his collaboration I succeeded in describing and building a compact, and relatively high finesse, beam-expander cavity, which will set the foundation for future molecular clocks in our group.

Despite working on completely different experiments than mine, Bjarke Takashi Røjle Christensen has never failed to contribute his knowledge, advice and encouragement throughout the whole span of my thesis.

Stefan Rathmann has been the latest edition to the group. Though never having worked together on any of the experiments, I am thankful for the good spirit and humor he brings to the lab. And for being forgiving for my lack of any tidiness when it comes to work desks.

The electronics workshop has been an ever helpful resource when it comes to advice on the design and manufacturing of electronics that has been essential to my experiment. I would especially like to thank Axel Boisen and Jimmy Cali Hansen for always being helpful, patient, and friendly, regardless the extend of the work needed to be done.

Lastly, my greatest gratitude goes to my supervisor, Jan W. Thomsen, for having included the group in the first place. Jan has always served as an inspirational and encouraging supervisor. I first found my interest in optics after following Jan's course during my bachelor degree, which I am extremely thankful for.

Besides my group, I owe great thanks to my friends, family and boyfriend for helping me throughout the span of my thesis. A special thanks goes to Jasmine MacKenzie for tirelessly proofreading my thesis and enforcing the oxford comma. My parents, Torkil and Kirsten, have never failed to express their encouragement, support, and enthusiasm about my work, despite having no clue of what I'm actually doing (I guess laser science just sound inherently cool). My sister, Clara, has always forced me to refine my explanatory skills due to her curious nature. She is courageous and stubborn, and I am very proud of her. I would like to thank Eva Brottmann Hansen for all our coffee breaks and inspiring quotes such as *”you really know it's weekend when you're all alone at the office all day writing your thesis. I like that”*. Those breaks have made the whole writing period much more lively. I would like to thank Natalia Havelund for spontaneous wine-dates, Anette

Andersen for delicious dinner-dates, Ane Baden for sharing her alwas pragmatic outlook on things, Line Juutilainen and Ela Uğur for being part of our study-trio through the first years of studying. Anne Nielsen for being just an awesome friend in general, who can turn a frown upside down in seconds. Finally, I would like to thank my boyfriend, Mads, for simply lighting up the end if each day in the office or lab, it being a good one or a bad one. You are the best person I know ♡

Ultracold Atoms and Quantum Metrology Group, May 2016

1 Introduction

Science has since its birth been a revolutionairy subject. The ever ongoing strive to dive into nature's fundamental script has been revolutionized more than once during the past couple of centuries. In the 1600s, Isaac Newton taught us about gravity. That our feet were planted solid on the ground due to mass of the earth pulling us down. A couple of hundred years later, in 1900s, Einstein taught us that time was relative, and that space and time were two sides of the same coin - space-time. The force of gravity was now suddenly introduced as the curvature of this space-time. Hubble made the discovery that the universe around us was expanding. That our neighbouring galaxies were rushing away at grave speeds, making our earth and solar system seem even tinier than what it may already have seemed at the time. Adding to this was a new theory of black holes, proposed by Einsten. Mass of such high density that the gravitational pull would not even allow light to escape. As the universe became increasingly mysterious, Niels Bohr fathered quantum mechanics. The true nature of the fundamental bricks of our universe, the atoms, was deemed indescribable to us, and a whole new paradigm was introduced. One atom could be two places simultaneously. Light interacted with matter. The energy state of matter was quantized.

All the scientific revolutions and shifts of paradigms made over the past century has fuelled the fire for modern day science, and through the search for the degree of truth in this new world view, technology has experienced an equal growth in capability. With every new paradigm came new ideas to test the validity of the extraordinary claims made in this new world view. One of the most famous claims by the general theory of relativty is the fact that time moves slower in larger gravitional fields. This effect is actually so pronounced that with the current technology, the gravitaional shift over a height difference in the centimeter range is measurable [28]. But how?

One of the demands made to technology has been its ability to perform precise, accurate and reliable measurements, and the measure of time is one of the quantities that we can measure with the most precision and accuracy [10]. In fact, it is the duration of one second that determines the length of one meter [3], which is defined as the length travelled by light in vacuum in 1/300000 of a second. The most reliable clocks available today are known as atomic clocks, and takes advantage of the interaction between light and matter, as described by Bohr's theory of quantum mechanics. Optical clocks present such high accuracy, that time can now be measured with an accuracy of 18 digits [26]. The amount of digits may seem excessive, but it is in those 18 digits that the gravitational shift is measured. The duration of one second does not seem to have a large impact of the average day-to-day life, but, adding a digit to the accuracy of a measurement is equivalent to adding pixels to a photograph. The more pixels used, the more details are revealed. What may have looked like noise in a system before, may hold information about new, undescribed systems. With such high accuracies, the persuit and pushing of new frontiers in science is possible. It opens the possibility to further test hypotheses made by Einstein such as gravitational waves that made their first confirmed appearance in early 2016 [27], or even test whether or not constants such as the fine structure constant or Plancks constant, are in fact constant in time.

Besides the benefits within fundamental research, the ability to build high accuracy and stable optcial clocks, also known as optical frequency standards, has had a great impact in the technology used in our everyday lives. The GPS system, for instance, relies on being able to counteract the shift in time arising from the change in gravitational potential due to the height difference between the surface of the earth and the orbit of the satellite.

The need for optical clocks transcends the laboratories. The work done in this thesis has been dedicated to buidling an optical clock, that is both simple and robust in design, but still offers a stability that is compatible with the current standard used to define the second, and can be applied in, e.g., space applications. One of the main missions is to design a clock that does not require trapping or cooling of atoms. The task has not been without its challenges, and as the experiment progressed, new sets of hurdles seemed to show up. The whole progress has been held back by impure molecular samples and highly unstable laser sources. The following chapters will serve to illumitate the underlying motivation for (thermal) optical frequency standards, introduce the theory of the physics constituting the foundation of a thermal frequency reference as well as give insight to the experimental techniques brought to practice when realizing an optical frequency reference. Furthermore, the extended setups built to compensate for the highly unstable laser source is also introduced. Lastly, a chapter dedicated to the future improvements of the experiment to work as a guide for future students is included.

In Sec. 2 the basic concepts of optical clocks and the mechanism constuting optical clocks are introduced. This is followed by an introduction to optical cavitites and their role in the work done during this thesis in Sec. 3. In Sec. 4 the NICE-OHMS technique used to realize a molecular based optical frequency reference is layed out. In Sec. 5 the reference itself, iodine, is presented along with some of its optical properties and the general energy-level structure of diatomic molecules is introduced. The experimental setup is presented in Sec. 6 along with the experimentally realized parameters and the preliminary results. A series of proposals for future improvements of the setup is given in Sec. 7. In Sec. 8 a brief conclusion on the work done during this thesis is presented.

2 Frequency Standards

A frequency standard can be many things. Anything that repeats itself periodically actually, but depending on the intended use, different requirements are made. For instance, the duration of a day may not need precision down to the second in the average everyday life, but rather minutes, hours, or even just the sun setting and rising on the horizon may be sufficient. If however, a 100 m race is to judge a winner, a scale based on seconds, and in most cases even milliseconds, is crucial. More scenarios can easlily be thought of, where the subdivison of time becomes increasingly important.

The relation between frequency and time is given by:

$$\nu = \frac{1}{T}, \tag{2.1}$$

ν is the frequency in units of Hz [1/s], and T is the repetition time, i.e., the time it takes for the given system to repeat its behaviour. If a system is said to be periodic, it is often referred to as an oscillator. An oscillatory motion is something that varies periodically. If an oscillator has a frequency of, e.g., 100 Hz, the varying motion repeats itself 100 times per second. If the frequency of the oscillator is 1000, the motion repeats itsef a 1000 times pr. second and so forth. Some of the oscillators used in modern days science have frequencies in the microwave and optical range corresponding to frequencies of 10^9 Hz and 10^{12} Hz, respectively.

A frequency standard, also known as a frequency reference, represents a system that has such a well defined frequency, that it works as a measure that other frequencies can be calibrated against. Most measurements performed in science are done against a time- or frequency scale, making precise, accurate and stable frequency references the beating heart of modern science and technology. It is important to note the subtle difference between the terms "accurate" and "precise". A device or a measurement may be precise but not accurate, and vice versa. If a measurement is accurate but not precise, the overall mean of the outcome is close to the true value being measured, but the ensemble of measurements has a wide spread. If a measurement is precise, but not accurate, the outcome yields the same result repeatedly with little variety, but the measured value has an offset from the true value, see Fig. 1. The last last requirement for a frequency reference is stability. The stability ensures that the reference does not drift in time.

A wide selection of frequency references are present, such as mechanical, quartz resonators, microwave resonators, or optical clocks. In Fig. 2 from [10] the progress in relative frequency uncertainty is shown. The relative uncertainty in frequency is the ratio between the the frequency at which the oscillator oscillates, compared to the uncertainty, or spread, of that frequency. For instance, an oscillator can oscillate at 100 Hz ± 1 Hz. This would give a relative uncertainty of 10^{-2}.

It is evident from the figure that the optical clocks are amongst the best candidates as frequency standards. This is partly due to the fact that optical frequencies are extremely high, in the 10^{12} Hz (THz) regime, and because the linewidth, i.e., the relative uncertainty typically is of the order of 10^3 Hz (kHz). Optical frequency standards are often build as atomic- or molecular clocks where the transitions between atomic- or rovibrational states, respectively, serves as the frequency discriminator. A review of the conceptual

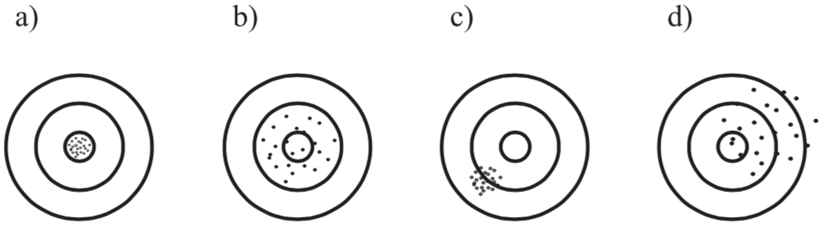

Figure 1: Figure from [10]: Different examples of measurements that showcase the difference between af precise and accurate. (a) shows a measurement that is both precise and accurate. It is precise due to the small variations in output, and it is accurate as the measured quantity mimmics that of the target value. In (b) the measurement is accurate, but not precise. The general output shows great variations, but the mean of all measured values still correspond to the target value. (c) shows a measurement that is precise, but not accurate. The output shows little variation, but the output has an offset from the target value. Finally, (d) shows a measurement that is not presice nor accurate.

understandig as well as the realization of optical frequency standards will be presented in the following section.

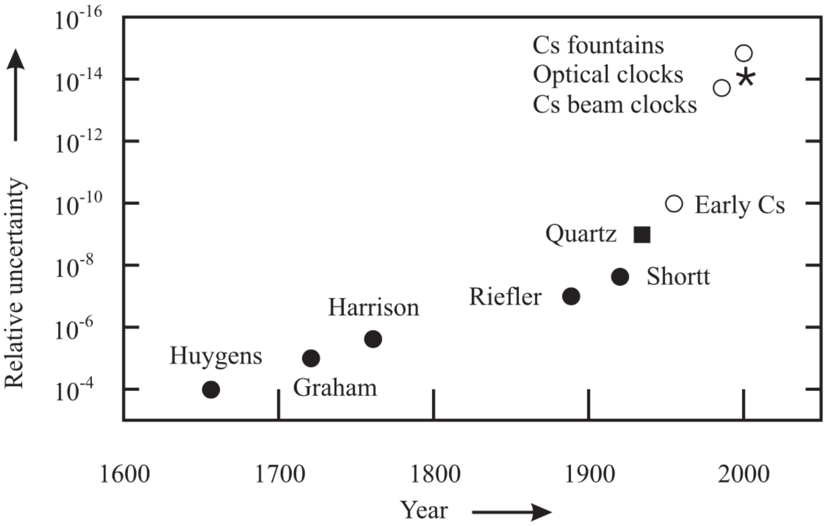

Figure 2: Figure from [10]: The performance of different frequency references. As technology and experimental methods improve, so does the performance as the relative uncertainty of the reference go down. The best frequency references are those in the optical regime.

2.1 Optical and Atomic Frequency Standards

Optical clocks work, as the name indicates, in the optical frequency regime. Though optical laser sources can be made extremely narrow, i.e., precise, they may suffer from drift in frequency, making them longterm unstable. Therefore, optical clocks has to stabilized against some kind of external reference that ensures the stability. This can either be done agains a high finesse cavity, which will be introduced in the next section, or by using an atom or molecule as the frequency discriminator. As the work done in this thesis is dedicated to the construction of a thermal frequency molecular-based reference, the physics constituting such a clock will be presented in this section.

Atomic- or molecular clocks form the pinnacle in terms of stable frequency references. This is due to the mechanism upon which the whole foundation for the clock is built: light-matter interaction. One of the motivations behind using optical clocks as frequency discriminators is the reproduceability. The optical properties of a given atom or molecule will not change, regardless of where in the universe the the atom is placed. Light-matter interaction has a broad variety of applications in anything from lasers to quantum information systems, just to name a few.

The energy state of matter, such as atoms and molecules, are quantum mechanically described by quantized energy levels. The energy levels can be made up of, e.g., electronic states or vibrational states, but for the purpose of introducing the concept of atomic and molecular clocks, the mathematical description of energy levels is saved for sec. 5.1.1. A conceptual schematic example of an atom occupying different energy states is shown in Fig. 3. The atom can change its energy state by absorbing a photon. Photons are elementary particles that mediate electromagnetic radiation and is used to quantize the energy states of electromagnetic radiation, such as light. When the atom absorbs the photon, the energy is transfered from the light to the atom, which in turn jumps to a higher energy level. The energy of a photon is given by:

$$E_{ph} = \hbar\omega_{ph}, \tag{2.2}$$

with $\omega_{ph} = 2\pi\nu_{ph}$ being the angular frequency of the light and $\hbar$ is Planck's constant. The photon can only be absorbed by the atom if the energy of the photon matches the energy difference between the two energy levels the atom can occupy, i.e., the photon energy has to match the transition energy. As the energy is defined through frequency, a transition in an atom defines the optical properties of the atom.

The energy states may not be completely well defined, but rather can be thought of as being fuzzy. The uncertainty in the energy states defines the transition linewidth. The linewidth of the transition is intimately linked to the lifetime of the atom being in the excited state through Heisenberg's uncertainty principle:

$$\Delta E \Delta t \geq \frac{\hbar}{2}. \tag{2.3}$$

If the energy difference, ΔE, between the ground- and exited or excited- and final state is very well defined, the lifetime is long, and vice versa. The Heisenberg uncertainty relation puts a lower limit to how well defined a given transition energy can be. When the atom de-excites it can happen by emitting a photon. This is called spontaneous emission. If the excited atom interacts with a photon that matches the energy of a transition in the atom, the atom will de-excite and emit a new photon matching the incoming photon, both in phase, frequency and direction. The exitation and de-excitation of an atom or molecule through the absorption and emission of electromagnetic radiation can be described as a damped harmonic oscillator dissipating energy. A quantum mechanical description can also be derived, but for now a classic approach will do. A damped harmonic oscillator may be described mathematically as [9]:

$$U(t) = U_0 e^{-\frac{\Gamma}{2}t} \cos(\omega_0 t), \tag{2.4}$$

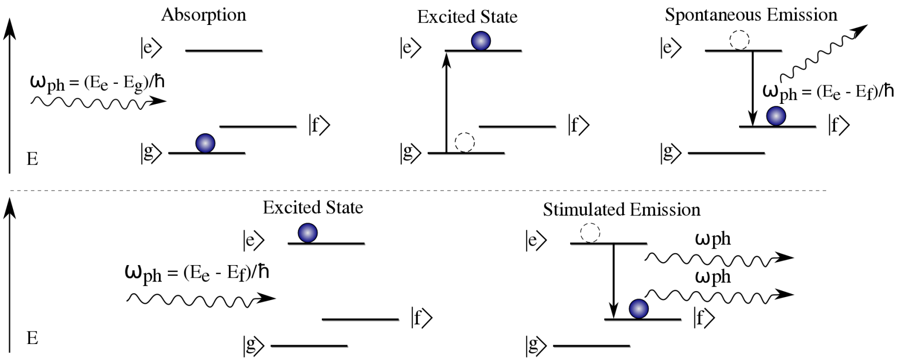

Figure 3: Schematics showing an atom absorbing and re-emitting a photon. In the top frame, the atom is in its energetic ground state denoted |g⟩. The excited state is separated from the ground state by some energy difference. The atom can become excited by absorbing a photon whose energy matches the energy difference between the ground- and excited state, denoted |e⟩. The atom will stay in the excite state for a given periode of time, until it spontaneously decay to some final stage |f⟩. When decaying spontaneously, the atom emits a photon, whose energy match the energy difference between the excited- and final state, in some random direction. In the bottom frame, the atom is already in the excited state when a photon with an energy corresponding to the difference between the excited- and final state interacts with the atom, making it decay and emit a photon identical in frequency, phase, and direction with the incoming photon. This process is known as stimulated emission, as the de-excitation of the atom is stimulated by the incoming photon.

where $U(t)$ describes the oscillator amplitude evolving in time, Γ is the decay rate and ω_0 is the oscillator frequency. U_0 is the initial amplitude of the oscillation. Taking the Fourier transform of $U(t)$ yields the frequency spectrum of the harmonic oscillator:

$$\mathcal{F}(U(t)) = A(\omega) = \int_{-\infty}^{\infty} U(t) e^{i\omega t} d\omega. \tag{2.5}$$

Assuming $U(t) = 0$ for $t \leq 0$, i.e., the oscillation starts at $t = 0$, and rewriting $\cos(\omega_0 t)$ in terms of exponentials, we get:

$$\begin{aligned} A(\omega) &= \int_0^{\infty} U_0 e^{-\frac{\Gamma}{2}t} \left(\frac{e^{i\omega_0 t} + e^{-i\omega_0 t}}{2} \right) e^{i\omega t} d\omega \\ &= \int_0^{\infty} \frac{U_0}{2} e^{\frac{-\Gamma}{2}t} e^{i(\omega+\omega_0)t} d\omega + \int_0^{\infty} \frac{U_0}{2} e^{\frac{-\Gamma}{2}t} e^{i(\omega-\omega_0)t} d\omega \\ &= \frac{U_0}{2} \left(\frac{1}{i(\omega-\omega_0)+\frac{\Gamma}{2}} + \frac{1}{i(\omega+\omega_0)+\frac{\Gamma}{2}} \right). \end{aligned} \tag{2.6}$$

We assume $\omega \approx \omega_0$, i.e., the second term only contributes little and is therefore neglected. The expression is rewritten and reduced to:

$$A(\omega) = \frac{U_0}{2} \frac{-i(\omega-\omega_0)+\frac{\Gamma}{2}}{(\omega-\omega_0)^2 + (\frac{\Gamma}{2})^2}. \tag{2.7}$$

Eq. 2.7 can be split into a real and imaginary part:

$$\begin{aligned} \Re(A(\omega)) &= \frac{U_0}{2} \frac{\Gamma/2}{(\omega-\omega_0)^2 + (\Gamma/2)^2} \\ \Im(A(\omega)) &= -\frac{U_0}{2} \frac{(\omega-\omega_0)}{(\omega-\omega_0)^2 + (\Gamma/2)^2}. \end{aligned} \tag{2.8}$$

The real part shows the frequency spectrum and the imaginary part describes the dispersion. The frequency spectrum hold the frequencies that the atom or molecule can absorb, and the imaginary part corresponds to the phase shift. The frequency spectrum has a Lorentzian lineshape. In Fig. 4 we see that the damping constant Γ corresponds to the Full-Width-at-Half-Max, FWHM, of the real part of eq. (2.7). Thus, Γ represents the linewidth of the transition. Since Γ corresponds to a width in frequency, $\Delta\omega$, the inverse of Γ can be thought of as the lifetime of a certain state or oscillation:

$$\Delta\omega = \Gamma = \frac{1}{\tau}, \tag{2.9}$$

which also implies that $\Delta\omega\tau = 1$. This can be interpreted as another version of Heisenberg's uncertainty principle. Looking at eq. (2.9) we see that the lifetime of a state goes up as the linewidth narrows.

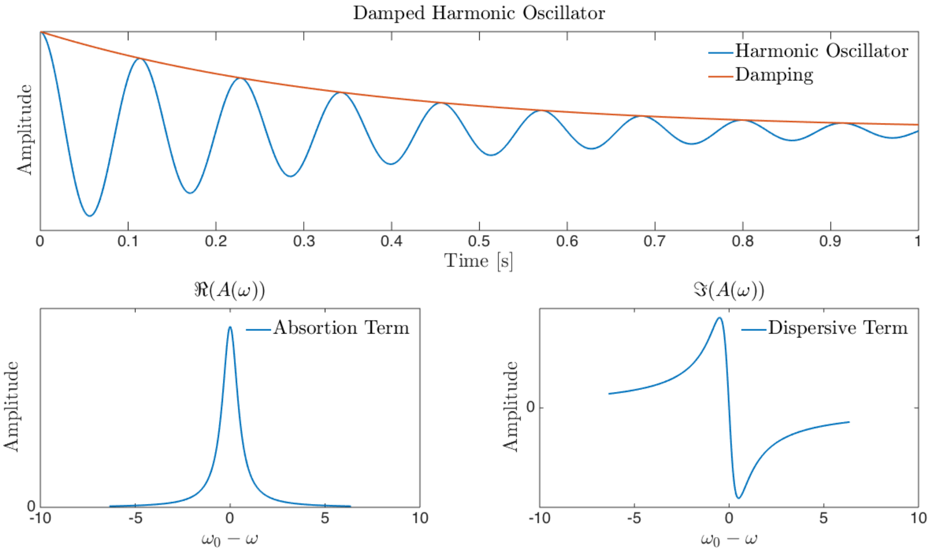

Figure 4: A radiating dipole modelled as a damped harmonic oscillator. The top plot show the timely evolution of the oscillator amplitude. The bottom plots show the absorbtion term and dispertion term, respectively. The absorption term corresponds to the frequency spectrum of the oscillator, and the dispersive term corresponds to the phase shift.

The quality of a harmonic oscillator is given as the ratio of the energy stored ind the oscillating motion and the dissipated energy. In [10], the Q-factor is derived:

$$Q = \frac{\omega_0}{\Gamma}. \tag{2.10}$$

Optical frequencies are in the THz regime, i.e., $\omega_0 \sim 10^{12}$ Hz, and the linewidth of atomic or molecular transitions can be of the order kHz, making the Q-factor of the system extremely high.

The linewidth of transitions in atoms and molecules can be measured by shining light though a sample of interest, and recording the transmitted signal. However, in order to use a transition in either an atom or a molecule, efforts must be made in order not to broaden the linewidth of the transition when measuring. Various broadening effects come into play when performing spectroscopic measurements. A couple of the most influential broadening effects will be introduced in Sec. 6.5, but the largest obstacle to overcome is the broadening attributed to the velocity atoms or molecules, which will result in Doppler broadening of the line profile. The nature of Doppler broadening as well as the measuring scheme designed to eliminate the Doppler broadening is introduced in the following section.

2.1.1 Saturated Absorption Spectroscopy

In reality, when measuring the linewidth of a given transition in an absorbing medium, it is often much wider than the natural linewidth Γ. Broadening effects can be plentiful, but the most dominant one is the Doppler broadening. Doppler broadening is present whenever the absorbing atoms or molecules, referred to as absorbers for generality, have a non-zero velocity compared to the laboratory's frame of reference, resulting in them being either red- or blue detuned from the photons frame of reference:

$$\omega = \omega_0 \pm kv, \tag{2.11}$$

where v is the molecular velocity relative to the beam, ω_0 is the frequency observed in the laboratory frame of reference, ω is the frequency in the absorber's frame of reference and $k = \omega/c = 2\pi/\lambda$ is the wavevector magnitude, see Fig. 5. The Doppler broadening can be written as:

$$\frac{\omega - \omega_0}{\omega_0} = \frac{v}{c}. \tag{2.12}$$

At large speeds, the Doppler broadening will become more and more dominate, which is a significant problem when performing spectroscopy on thermal samples where the velocity of the absorbers is high. The broadened linewidth is no longer a Lorentzian, but rather a Gaussian profile [23]. The lineprofile of a Doppler broadened absorber is given by [23]:

$$g_D(\omega)d\omega = \frac{c}{u\omega_0\sqrt{\pi}} \exp\left\{ -\frac{c^2}{u^2}\left(\frac{\omega - \omega_0}{\omega_0}\right)^2 \right\}. \tag{2.13}$$

Here $u = \sqrt{2k_{\mathrm{B}}T/M}$ is the most probable speed of the absorber, and k_{B} and M is Boltzmanns constant and the mass of the absorber, respectively. The speed of the absorbers, v, follow a Maxwell-Boltzmann distribution.

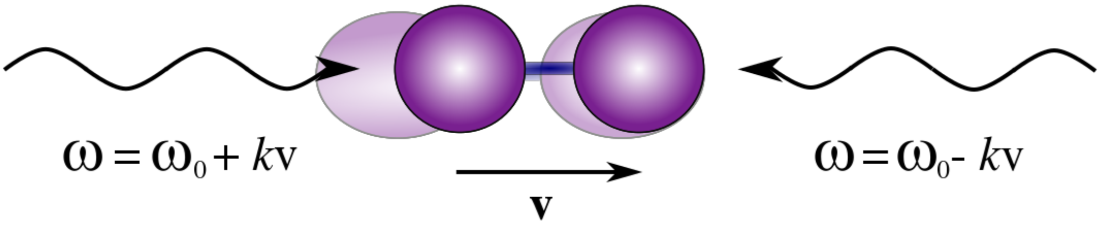

Figure 5: An absorber, in this case a molecule, travelling with velocity $\mathbf{v}$. The photon interacting with the molecule will see a broadened absorption profile, broadened by $\omega_0 \pm k\mathrm{v}$, depending on the direction of the beam. k is the size of the wavevector of the light, and v is the speed.

The Dopppler broadened linewidth is several orders of magnitude wider compared to the natural linewidth. In, e.g., Sodium where the 3s-3p transition has a natural linewidth of 10 MHz, the Doppler broadened lineprofile is 1600 MHz at room temperature [23]. A simulated example of a Doppler broadened profile is shown in Fig. 6.

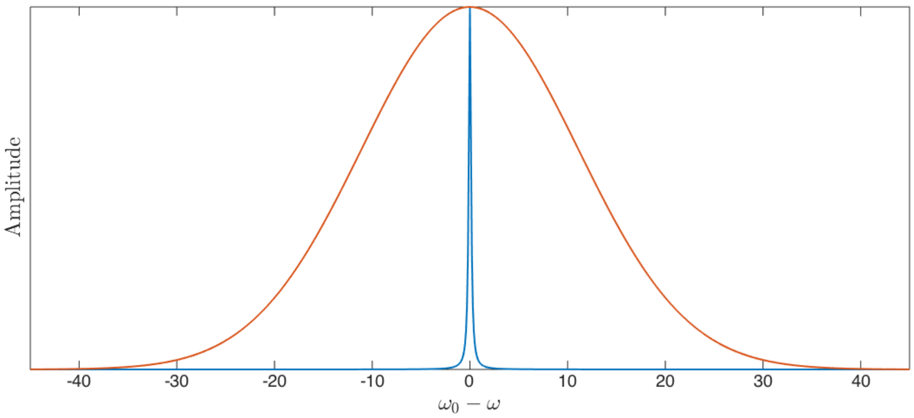

Figure 6: A simulated example of a Doppler broadened absorption profile. The orange curve shows the broadened line profile, and the blue shows the natural linewidth of the absorber. Due to the speed of the absorbers, the absorption profile change from a narrow Lorentzian, to a much wider Gaussian profile. The width of the Doppler broadened absorption profile can be several thousand times wider than the natural linewidth of the absorber [23]. Doppler broadening is one of the most pronounced broadening effects in spectroscopy performed on thermal samples, i.e., in samples where the absorbers have a large nonzero velocity.

Saturated absorption spectroscopy (SAS) is a clever way of circumventing Doppler broadening of the transitions in a molecular- or atomic sample. This is done by having a counter propagating pump- and probe beam. The pump beam serves to saturate the absorbers, and the probe beam will then see less absorption at the saturated transition, revealing the spectral properties of the absorber. Because the two beams are travelling in opposite directions, the signal obtained will be that of the molecules moving perpendicular to the beam direction. The pump- and probe beam are identical in frequency, and usually stem from the same laser source. An example of a SAS setup is shown in Fig. 7: two beams are split into two different paths using a 90:10 beamsplitter, and then recombined and overlapped at the sample of interest. The signal from the probe beam is then picked up by a photodiode. A simulated example of a SAS signal is shown in Fig. 8.

The cost of performing SAS is that most of the absorbers will end up not contributing to the saturated signal. This is due to the fact that the asorbers move around in the sample region in random directions, and only a fraction of them will have a zero velocity component in the direction perpendicular the interrogating beams. The number of molecules being interrogated can be evaluated by integrating the fraction of molecules that move with a velocity perpendicular to the beam direction, and the molecules with a velocity corresponding to $v = \Gamma/k$ in the same direction as the interrogation beams. Here Γ is the spectral linewidth of the transition being interrogated and $k = 2\pi/\lambda$ is the wave vector magnitude of the light emitted. If the beam is moving in the z-direction, the number of molecules contributing to the saturated absorption signal can be evaluated by [23]:

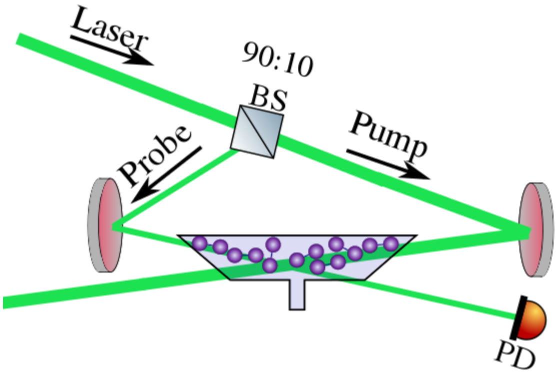

Figure 7: A generic example of a setup used in saturated absorption spectroscopy. A laser is split into two different paths using a 90:10 beamsplitter (BS) and are recombined at the sample of interest, pictured as a molecular vapor sample in this setup. The more powerful pump beam serves to excite the molecules. The probe beam will see less absorption when interacting with the all ready excited molecules. This will show up as Lorentzian peaks in the signal recorded by the photodetector (PD). A simulated example of a spectra obtained using SAS is shown in Fig. 8.

$$\int_{-\infty}^{\infty}\int_{-\infty}^{\infty}\int_{-\Gamma/k}^{\Gamma/k} f(v)dv_x d_y dv_z = \pi^2\sqrt{\frac{M}{\pi 2k_BT}}\int_{-\Gamma/k}^{\Gamma/k}\exp\left(\frac{-Mv_z^2}{2k_BT}\right)dv_z. \tag{2.14}$$

Usually, the number of absorbers contributing to the signal is reduced to a few percent [23]. The signal from the saturated absorbers is thus smaller than that of the Doppler broadened profile. Therefore, when perfoming saturated spectroscopy, large samples are preferred in order to compensate for the decrease in signal.

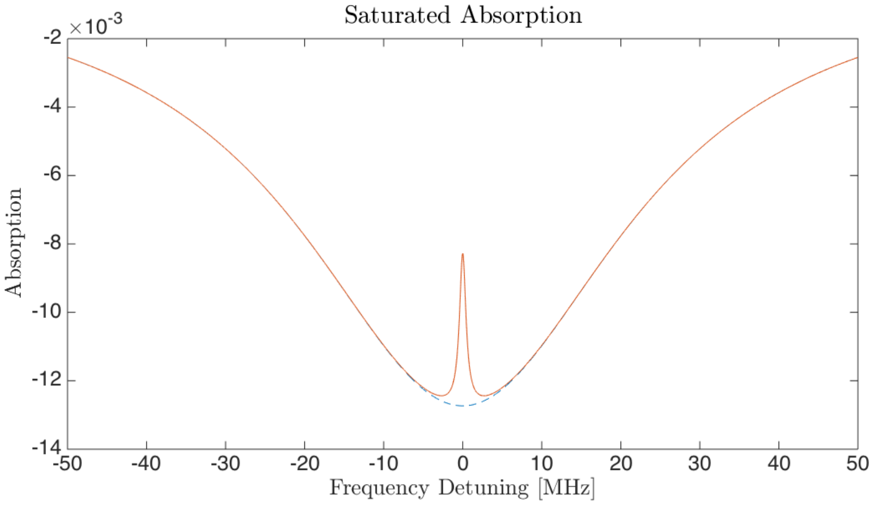

Figure 8: A simulated example of a SAS signal. The blue dashed line shows the Doppler broadened absorption, and the orange line shows the satuated absorption. The saturated peak sin on top of the Doppler broadended line profile.

Once the Doppler broadening has been eliminated, other broadening effects come into play and can serve to corrupt the signal. Amongst these we find power broadening, pressure broadening and transit time broadening. These will be introduced in more detail in Sec. 3.3.2.

2.2 Pracitcal Applications of Atomic- or Molecular Frequency Standards

As already mentioned, one of the main advantages of using an atomic- or molecular medium as frequency reference is the fact that they do not drift in time. The energy levels in atoms or molecules do not change in time, making them the ultimate frequency discriminator. An atomic- or molecular based frequency reference will be immune to changes in environment, meaning that a clock based in Copenhagen will oscillate at the same frequency as a clock based anywhere else in the universe, e.g., in a satellite. By knowing the frequency of the transition in an absorber placed on earth, the shift in time due to the change in gravitational field between the surface of the earth and a satellite in orbit can be accounted for, by referring the frequency measured by an identical absorber placed on board the satellite [4].

Since the dawn of atomic clocks a vast amount of efforts have been made in order to push the limits of performance both in terms of what frequencies can be used, but also in terms of stability. One of the current obstacles is to provide atomic- or molecular clocks that are simple, robust, and stable, so that they can work and be applied outside the laboratory, for example, on board satellites.

Each GPS satellite in orbit is equipped with an atomic clock on board that is synchronized to an atomic clock on ground, to counteract any shifts in time induced by the change in gravitational field, see Fig. 9. Without these corrections the performance of the GPS system would be very unreliable with an error of several meters pr. minute accumulating [4]. The current clocks used in GPS systems are Rubidium-based and works in the GHz regime. Thus, if an atomic- or molecular clock in the THz regime could be employed, the quality factor of the oscillator automatically increase by a facor of a thousand due to the increase in frequency. Competing with a Rubidium clock, however, is not as straight forward as one might imagine. A Rubidium clock is cheap and compact, which further serves to motivate the goal of constructing a molecular clock that can demonstrate the same robustness, but outperform in terms of stability and precision.

The use of atomic- or molecular frequency references for space applications is not limited to GPS. Fundamental research investigating gravitational waves plans on implementing an atomic or molecular clock as a frequency reference used in laser interferometry designed to detect gravitational waves. The Laser Interferometer Space Antenna project, LISA, is one of the experiments under design in need of a stable, optical clock in order to further investigate gravitational waves [5].

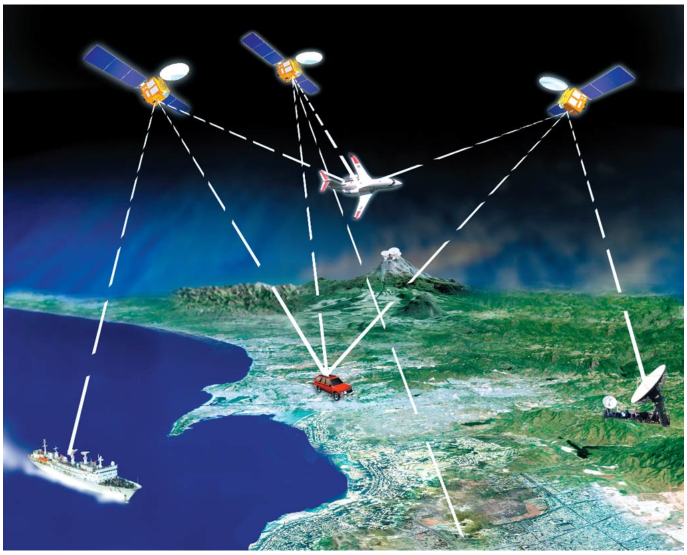

Figure 9: GPS-satellites. The GPS system works by having three satellites measure the distance to an object, and reference the coordinate to each other. Therefore, it is crucial that the inner clock in each sattelite is syncronized. Furthermore, due to change in the gravitational field between the surface of the earth and the satellites in orbit, general relativity dictates that time moves slighty faster in orbit that on earth. The clock therefore also has to be precise enough to compensate for the shift in time due to the shift in gravitational field. Figure from [31].

3 Optical Cavities

Optical cavities play an essential role in the setup built during this thesis. The employment of an optical cavity is the key to acheiving a spectroscopic setup that can defy restrictions arising from the sample size limiting the signal obtainable. In this chapter the concept of optical cavities will be introduced together with the intended practical usage and motivation behind including optical cavities in spectroscopy.

3.1 Simple Cavity Model

In its simplest form, an optical cavity, also known as an optical resonater, is a two-mirror configuration separated by a distance L, in between which an electromagnetic field is reflected back and forth, see Fig. 10. Each mirror has a reflection and a transmission coefficient denoted r_1, t_1 and r_2, t_2 for mirror 1 and 2, respectively. The reflection and transmission coefficient determines how much of the incident field amplitude is reflected or transmitted. The electromagnetic field is described by its amplitude and its phase. The phase is described by using $\exp(i(\omega t - \bar{\mathbf{k}} \cdot \bar{\mathbf{r}}))$ and is chosen to be 1 at the mirror surface. ω is the frequency of the field, $\bar{\mathbf{k}}$ is the wave vector, and $\bar{\mathbf{r}}$ is the distance travelled by the light.

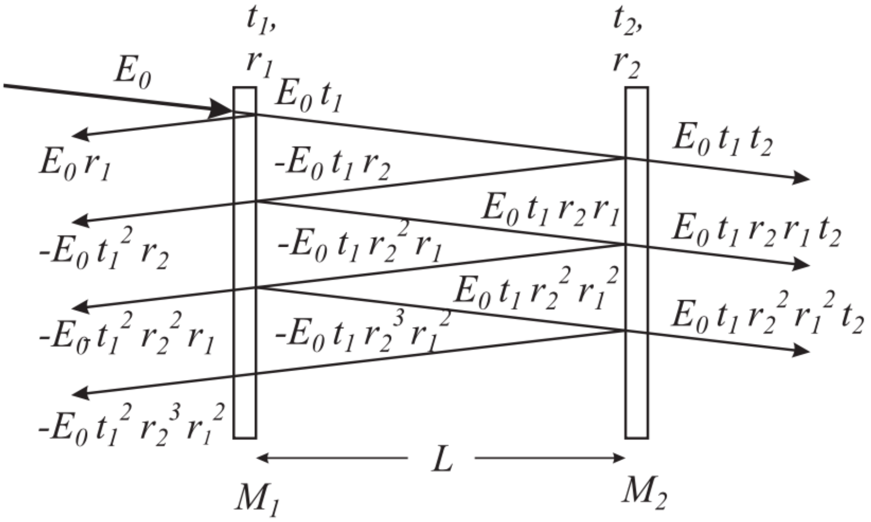

Figure 10: An electric field reflected back and forth between two flat mirrors with reflection and transmission coefficients r_1, t_1 and r_2, t_2 for mirror 1 and 2, respectively. Figure from [10].

The field transmitted by the cavity can be evaulated by collecting the terms to the right of mirror 2. Each time the field has circulated between the mirrors, it picks up a phase factor of $\exp(\bar{\mathbf{k}} \cdot \bar{\mathbf{r}}) = \exp(-i(\omega/c) \cdot 2L)$. When all the terms are collected, it can be expressed as a geometrical series, the derivation is shown in Appendix A. The expression for the transmitted field is reduced to:

$$E_T = E_0 \frac{t_1 t_2 \left(e^{i\omega L/c} - r_1 r_2 e^{i\omega L/c}\right)}{1 + r_1^2 r_2^2 - 2 r_1 r_2 \cos(\omega 2L/c)}, \tag{3.1}$$

and hence, as the power transmitted by the cavity is proportional to the square of the transmitted field we get:

$$E_T E_T^* = E_0^2 \frac{t_1 t_2}{1 + r_1^2 r_2^2 - r_1 r_2 \cos(2\omega L/c)}. \tag{3.2}$$

Here the phaseshift can be identified as $\Delta\phi = 2\omega L/c$. Using this, we can define the spacing between the resonance frequencies of the cavity:

$$\Delta\phi = 2\pi = 2\omega L/c \rightarrow \Delta\nu = \frac{c}{2L} \equiv FSR. \tag{3.3}$$

Where $\nu = \omega/2\pi$ is the frequency of the E-field. This frequency difference $\Delta\nu$ is known as the free spectral range (FSR). The FWHM of the field is approximated by [10]:

$$\delta\nu = \frac{1 - r_1 r_2}{\pi\sqrt{r_1 r_2}} \frac{c}{2L}. \tag{3.4}$$

The FSR and the FWHM gives rise to a new cavity parameter that is a measure of the goodness of the cavity, known as the finesse:

$$F = \frac{FSR}{FWHM} = \frac{\pi\sqrt{r_1 r_2}}{1 - r_1 r_2}. \tag{3.5}$$

For the case of the transmitted intensity, r_1 and r_2 is subsituted by r_1^2 and r_2^2.

The frequencies supported by the cavity is determined by the length of the cavity [9]:

$$\text{L}{=}n\frac{\lambda}{2}, n = 1, 2, ... \tag{3.6}$$

where $\lambda = 2\pi c/\omega$ is the wavelength of the electromagnetic wave. The requirement for constructive interference can thus be fulfilled by varying either the cavity length or the wavelength of the light. The physical picture can be compared to that of a guitar string, which supports certain musical notes determined by the length of the string - a change in length will change the tone.

So far we have only considered the reflection and transmission of a generic field between two flat mirrors. In order to describe the mode of the field inside the cavity, more math is needed. Before going any further it is safe to assume that the mode must have the following propterties: the mode has to reproduce itself after one roundtrip such that it does not interfere with itself destructively, and the mode must have some kind of beam like shape, i.e., it must be confined in the transverse plane defined by the mirrors, in order to not be larger than the physical mirrors. With these assumptions, the equation that the field must satisfy is the paraxial wave equation [9]:

$$\left(\nabla_T^2 + 2ik\frac{\partial}{\partial z}\right) E = 0. \tag{3.7}$$

Here $k = 2\pi/\lambda$ is the wave vector magnitude of the field, and ∇_T^2 is the transverse Laplacian, defined as $\nabla_T^2 = \partial_x^2 + \partial_y^2$ for a beam propagating in the z-direction. A trial solution of the following form can be introduced:

$$\varepsilon(\mathbf{r}) = Ae^{ik(x^2+y^2)/2q(z)} e^{ip(z)}, \tag{3.8}$$

where A is the amplitude, and $q(z)$ and $p(z)$ are beam parameters to be determined. Plugging this into the paraxial wave equation, the following differential equation is found:

$$\left[\frac{k^2}{q(z)^2}(x^2+y^2)\left(\frac{dq(z)}{dz}-1\right)-2k\left(\frac{dp}{dz}-\frac{i}{q(z)}\right)\right]\varepsilon=0. \tag{3.9}$$

This equation is satisfied if

$$\begin{aligned}\frac{dq(z)}{dz}-1&=0,\\ \frac{dp}{dz}-\frac{i}{q(z)}&=0.\end{aligned} \tag{3.10}$$

Integrating for $q(z)$ and $p(z)$, one finds:

$$\begin{aligned}q(z)&=q_0+1\\ p(z)&=i\ln\left(\frac{q_0+z}{q_0}\right).\end{aligned} \tag{3.11}$$

Here $q_0=q(z=0)$, and we assume that $p(0)=0$. Now, the beam parameter $q(z)$ can be chosen such that the final field has the same properties as that of a Gaussian beam:

$$\frac{1}{q(z)}=\frac{1}{R(z)}+\frac{i\lambda}{\pi w(z)^2}, \tag{3.12}$$

this gives:

$$e^{(x^2+y^2)/2q(z)}=e^{\frac{ik(x^2+y^2)}{2R(z)}}e^{\frac{(x^2+y^2)}{w(z)^2}}. \tag{3.13}$$

$R(z)$ is the front wave curvature of the beam, and $w(z)$ is the waist radius of the beam, and corresponds to the radius of the radial distribution of the field mode. A Gaussian beam is completely characterized by the beam waist at the narrowest point, which is found at $R(z)=\infty$. From this, the following parameters can be derived [9]:

$$\begin{aligned}R(z)&=z+\frac{z_0^2}{z},\\ w(z)&=w_0\sqrt{1+\frac{z^2}{z_0^2}},\\ z_0&=\frac{\pi w_0^2}{\lambda}.\end{aligned} \tag{3.14}$$

where a new parameter introduced, z_0, is the Rayleigh length, defined as the distance that satisfies $w(z_0)=\sqrt{2}w_0$. Using these identities in $p(z)$, we find:

$$e^{ip(z)}=\frac{1}{1+iz/z_0}=\frac{1}{\sqrt{1+z^2/z_0^2}}e^{i(\tan^{-1}(z/z_0))}. \tag{3.15}$$

Substituting x^2+y^2 for r^2, the complete solution to the paraxial wave equation is then written as

$$\varepsilon(r,z)=\frac{Ae^{i(kz-\tan^{-1}(z/z_0))}}{\sqrt{1+z^2/z_0^2}}e^{ikr^2/2R(z)}e^{-r^2/w(z)^2}. \tag{3.16}$$

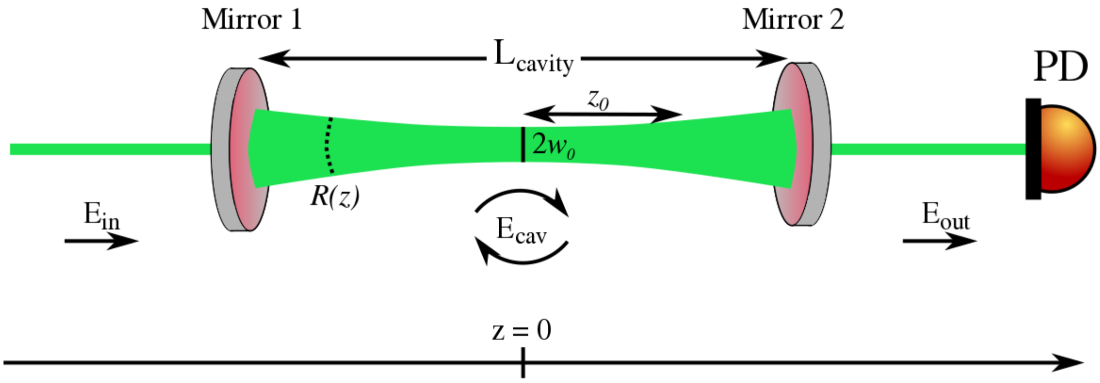

Figure 11: Two mirrors separated by distance L_{cavity} supporting a Gaussian mode. The mode of the electromagnetic field builds up when the requirement for constructive interference is satisfied. The mode in the cavity is characterized by the beam radius denoted w_0, which is determined by the radius of curvature of the mirrors and the cavity length.

A cavity supporting a Gaussian beam is shown in Fig. 11. There are other modes that fulfill the requirements introduced with the paraxial equation. These are introduced and briefly discussed in Appedix A.

The field transmitted by the cavity can be monitored using a photodiode (PD). A PD is sensitive to the power of the field given in eq. (3.2). A typical cavity transmission signal for a well-aligned cavity is shown in Fig. 12.

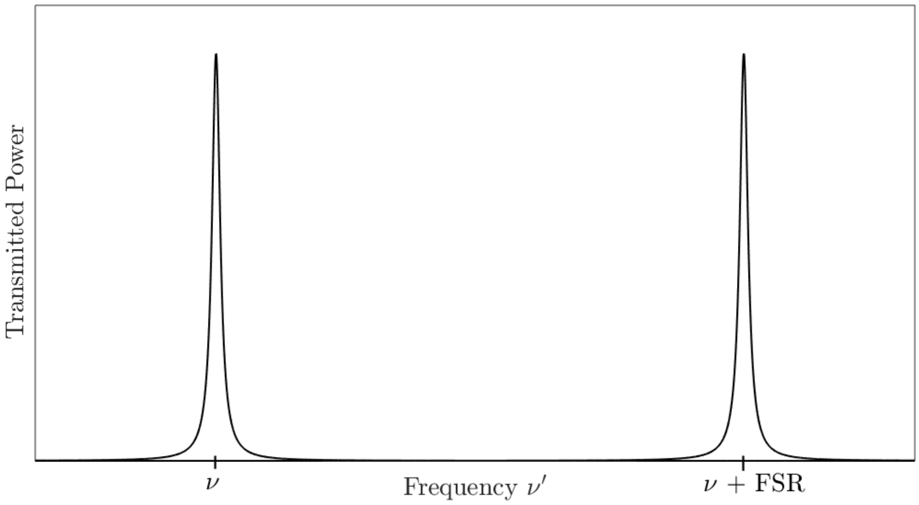

Figure 12: A simulated example of what a signal that is transmitted by a cavity may look like. The x-axis show what frequencies are coupled into the cavity. When the frequency ν' matches the resonance condition for a standing wave, the power transmitted will show up as a peak in frequency, with its width defined by eq. (3.4). Both the modes supported at ν and at $\nu + FSR$ are shown. The signal recorded by the PD will show a Lorentzian peak and is proportional to the field squared. The frequency supported can be varied by changing the cavity length.

3.1.1 Finesse, Mode Matching & Resonator Stability

The finesse of an optical cavity has already been touched upon in the previous section. The most basic definition, is defined as the ratio between the FSR and the FWHM of the supported modes, e.g., the width of the modes shown in Fig. (12):

$$\begin{aligned} F &= \frac{FSR}{FWHM} \\ &= \frac{\pi\sqrt{R}}{1-R}. \end{aligned} \tag{3.17}$$

Where $R = r^2$ is the reflection coefficient if the intensity of the field. The transmission of the intensity is likewise expressed as the square of the transmition of the field, i.e., $T = t^2$. The finesse of the cavity can also be approximated by reviewing the round trip loss [2]:

$$F = \frac{2\pi}{\text{Loss}} = \frac{2\pi}{2T + 2A}, \tag{3.18}$$

where T is the mirror transmission coefficient of the intensity and A holds any additional losses arising from scattering or absorption in the mirrors. A is usually assumed neglible for a low finesse cavity where $T \gg A$.

As technology has advanced and mirror reflectivity can be made close to 1, cavities with a finesse of the order of several hundred thousands and up have been demonstrated [9]. The cavities used in this project have had two very different purposes and thus the two cavities have very different requirements for the finesse. These will be discussed in Sec. 6.4 and 6.7. Cavities with extremely high finesses can themselves be used as frequency references. In fact, optical cavities with linewidths in the mHz regime and short-term fractional instability on the 10^{-16} level have been demonstrated [24]. The current limitations in stability of such cavity systems is limited by the thermal motion of the mirrors.

Essential to the performance of an optical cavity is the coupling of light into the cavity. The beam that is to be coupled into the cavity, has to have a profile that matches the mode supported by the cavity, i.e., the waist $w(z)$ and front wave curvature $R(z)$ of the beam has to be the same as the waist supported by the cavity and the radius of curvature (ROC) of the mirrors. The waist is ultimately determined by the ROC of the mirrors and their separation. This is known as *mode matching.* Using the identies in eq. (3.14) and demanding that $R(z)$ matches the mirrors' ROC at a distance equal to the cavity length, the desired waist radius can be calculated:

$$w_0 = \left[\frac{\lambda \left[\left(\frac{2ROC-d}{4} \right) d \right]^{1/2}}{n\pi} \right], \tag{3.19}$$

where d is the cavity length, n is the index of refraction of the medium inside the cavity, which is typically air. λ is the wavelength of the light coupled in. Typical waist values vary from 100 μm to 1 mm.

Whether or not a cavity can support a stable mode is determined by the mirror separation and the mirror ROC. If a cavity mode is unstable, the light will escape the cavity before any field build up takes place. In order to support a stable mode, the cavity must satisfy the following relation, [9]:

$$0 \leq g_1 g_2 \leq 1, \tag{3.20}$$

where $g_1 = 1 - d/ROC_1$ and $g_2 = 1 - d/ROC_2$. ROC_i is the ROC of mirror i. This stability relation must not be confused with the fractional instability of the cavity. The term in eq. (3.20) is simply a measure of whether or not it is possible to support a stable cavity mode in the first place. If $ROC > 0$ the mirror is said to be concave where as $ROC < 0$ is convex. If $g_1 g_2 = 0$ or 1 the resonator is on the verge of becoming unstable and even the slightest change in alignment or length will make the system unstable, e.g., a configuration of two flat mirrors, i.e., ROC $= \infty$ will be undesireable. One could also imagine a cavity with the mirrors separated only by a few microns. This setup will also be undesireable, as the sligthes change in cavity length that may arise from temperature fluctuations of the mirrors will destabilize the cavity. It is thus preferable to have a system that has the properties $0 < g_1 g_2 < 1$.

3.2 Cavity Locking Scheme

Cavities support constructive interference when the requirement of eq. (3.6) is fulfilled. Therefore, efforts must be made to counteract even small changes in length, such that the cavity can support a standing wave at all times. This is known as cavity locking, as the cavity is locked at a certain length. For most practical applications locking the cavity to ensure constant constructive interference is sought after. To maintain constant constructive interference the variations cavity length must be controlled in order to counteract the noise from the surroundings. Noise can stem from, e.g., change in temperature or vibrations in the cavity foundation (the table upon which the cavity is placed) that introduce disturbances in the cavity length and cause drift. In order to stabilize to the point at which constuctive interference is present an *error signal* must be generated.

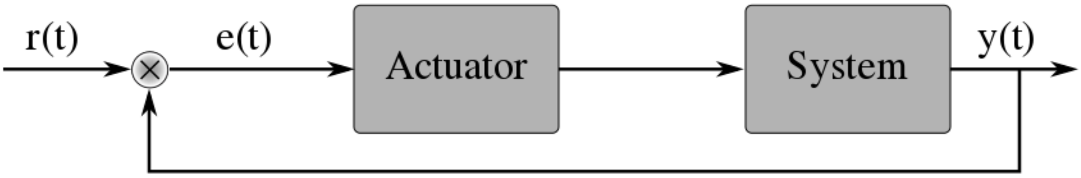

Figure 13: Block diagram of a feedback loop. A system is acted upon by some actuator and yields a measurable output y(t). The output is then compared to a controlsignal r(t), from which the error signal is generated. The error signal is fed to the actuator, which in turn acts on system to make the system output mimic that of the control signal.

An error signal can be described as a signal that contains information about how far from a desired state a given system is. The state of the system could either be a certain temperature, or in the case of optical cavities, a certain cavity length that supports constructive interference. As a generic example, consider the follwing scenario: a system, which can be anything from an optical cavity to a hob on a stove, delivers some kind of measurable output, e.g., optical power build up or hob temperature, that varies with time, denoted y(t). The goal is to be able to control the system, and thereby the system output. The systems state can be changed or controlled through an actuator, which could be a device that changes the cavity length or a knob on the stove that change the hob temperature.

If a desired state of the system is chosen, i.e., a signal to which the output is compared against, denoted r(t), one is interested in knowing how far away from the desired state the system currently is. This can be calculated by subtracting the system output and the control signal, generating an error signal: e(t) = r(t) - y(t). The error signal can then be applied to the actuator, which in turn, if designed properly, will serve to bring the system to the desired state. When e(t) = 0, there is a complete correspondence between the actual state of the system and the control signal. When the error signal is used to correct the system state, we refer to it as a feedback loop, as it works as a feedback mechanism. A schematic of a feedback loop is shown in Fig. 13. The sign of the error signal helps determine what actions should be applied to the system to bring the system back to its desired state, e.g., for an optical cavity, the sign of the error signal can reveal whether or not the change in cavity length should be negative or positive, i.e., shorter or longer.

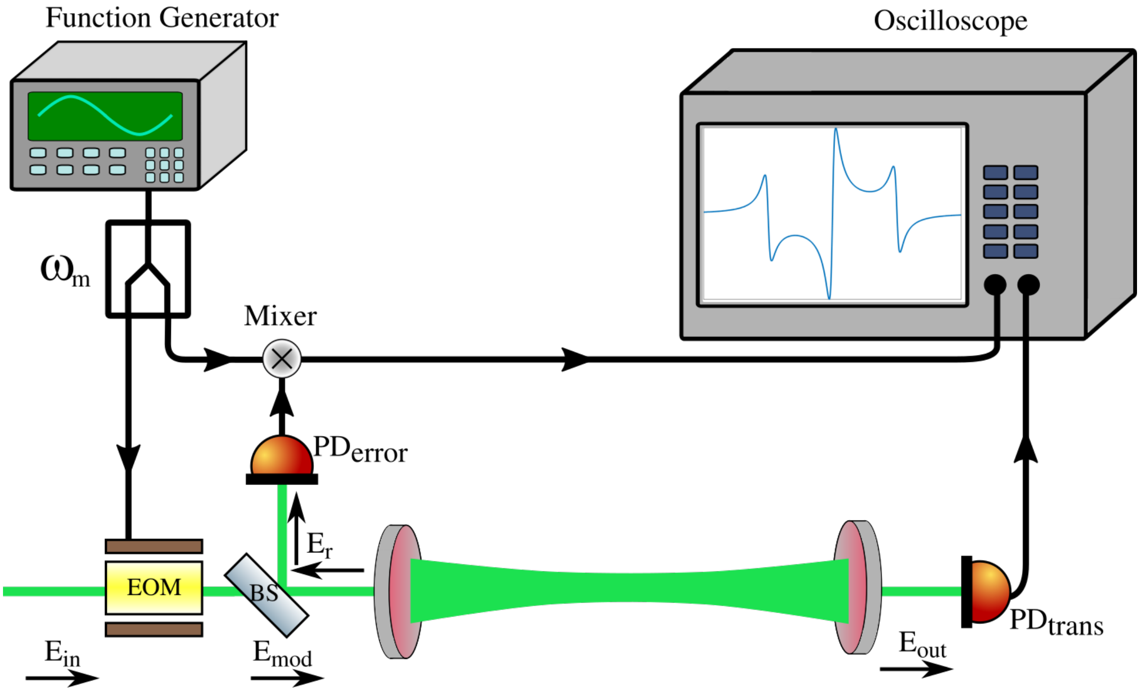

Figure 14: PDH setup scheme: a beam is modulated using an EOM, and is then coupled into the cavity. the modulation frequency is ω_m. The field reflected from the cavity is picked up by $\mathrm{PD_{error}}$, and demoluted at ω_m. An example of the generated error signal is shown on the oscilloscpe. The cavity transmission signal, which is not shown in this figure, is picked up by $\mathrm{PD_{trans}}$.

The locking scheme used in this thesis is the Pound-Drever-Hall locking scheme (PDH). The general setup used to generate the PDH error signal is shown in Fig. 14. The PDH technique relies on frequency modulation of the light coupled into the cavity, and detection of the light reflected from the cavity. Frequency modulation is achieved using an Electro-Optic-Modulator (EOM). The EOM consists of an electro-optic crystal placed inbetween two metal plates working as a capacitor. A time-varying sinusiodal voltage is applied over the crystal making the index of refraction vary in time. The modulation amplitude is proportional to the modulations index δ. A field described by $E = E_0 \exp(i\omega t) + c.c.$, will after being modulated by an EOM be described by:

$$E_{mod} = E_0 \exp\left(i\left(\omega t + \delta \sin(\omega_m t)\right)\right) + c.c. \tag{3.21}$$

The modulated E-field can be described using Bessel functions:

$$e^{i\delta \sin(\theta)} = \sum_{n=-\infty}^{\infty} J_n(\delta) e^{in\theta}, \tag{3.22}$$

where the following holds true

$$J_{-n}(\delta) = (-1)^n J_n(\delta), \tag{3.23}$$

where $J_n(\delta)$ is the n'th order Bessel function, see Fig. 15.

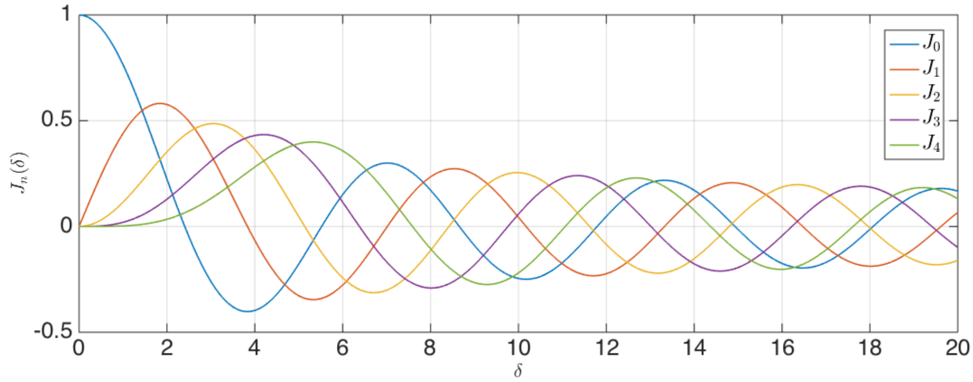

Figure 15: Bessel functions of the first kind for n = 1 to 4. For $\delta < 1$, contributions from n>1 can be assumed to be small.

The modulation index δ is much less than 1 for the sytem treated in this work. This implies that contributions to the total field for n>1 can be left out, as the amplitude of the higher order Bessel function shown in Fig. 15 are small for $\delta \ll 1$. Using eq. (3.22) and expanding for n = 0 to 1, we get the expression for the first order sidebands and the original field:

$$E_{mod} = E_0 \left[J_0(\delta) e^{i\omega t} + J_1(\delta) e^{i(\omega+\omega_m)t} - J_1(\delta) e^{i(\omega-\omega_m)t} \right] + c.c., \tag{3.24}$$

i.e., the original field and two smaller sidebands with opposite phase placed at $\pm\omega_m$. As shown in Fig. 14, the error signal is generated by picking up the field reflected of the cavity incoupling mirror. The reflection coefficient is given by $r(\omega) = \frac{E_r}{E_0}$. The field amplitude reflection coefficient $r(\omega)$ of the cavity is frequency dependent. This is analogous to the transmitted power being frequency dependent as described in Sec. 3.1. More light is coupled into the cavity when the frequency of field is supported. Expressed in terms of the detuning from resonance, the amplitude refelction coefficient can be written as [10]:

$$r(\Delta\omega) = \frac{-\Delta\omega(\Delta\omega + i\Gamma/2)}{(\Gamma/2)^2 + \Delta\omega^2}. \tag{3.25}$$

Here Γ is the linewidth of the cavity and $\Delta\omega = \omega - \omega_0$ is the detuning from cavity resonance. The reflected field is expressed in terms of $E_r = r(\omega)E_0$. Combining this with eq. (3.24), we get:

$$E_r = \frac{E_0}{2} \left[r(\omega) J_0(\delta) e^{i\omega t} + r(\omega+\omega_m) J_1(\delta) e^{i(\omega+\omega_m)t} - r(\omega-\omega_m) J_1(\delta) e^{i(\omega-\omega_m)t} \right] + c.c. \tag{3.26}$$

The signal picked up by $\mathrm{PD}_{\mathrm{error}}$ in Fig. 14 picks up the reflected field and generates a photocurrent that is proportional to the square of the reflected field:

$$i_{PD} \propto E_r E_r^*. \tag{3.27}$$

When expanding, the equation for i_{PD} contains terms oscillating at $2\omega_m$ [10], but due to the de-modulating of the signal at ω_m, the final DC-signal is only sensitive to fields oscillating in the vicinity of ω_m, as all terms containing $2\omega_m$ will average to zero, [10]:

$$i_{PD} \propto J_0(\delta)J_1(\delta)\left[A(\Delta\omega)\cos(\omega_m t) + D(\Delta\omega)\sin(\omega_m t)\right], \tag{3.28}$$

where $A(\Delta\omega)$ and $D(\Delta\omega)$ are defined as:

$$D(\Delta\omega) = -4\frac{\omega_m^2(\Gamma/2)\Delta\omega\left[(\Gamma/2)^2 - \Delta\omega + \omega_m^2\right]}{\left[\Delta\omega^2 + (\Gamma/2)^2\right]\left[(\Delta\omega+\omega_m)^2 + (\Gamma/2)^2\right]\left[(\Delta\omega-\omega_m)^2 + (\Gamma/2)^2\right]} \tag{3.29}$$

$$A(\Delta\omega) = 4\frac{\omega_m^2(\Gamma/2)\Delta\omega\left[(\Gamma/2)^2 + \Delta\omega + \omega_m^2\right]}{\left[\Delta\omega^2 + (\Gamma/2)^2\right]\left[(\Delta\omega+\omega_m)^2 + (\Gamma/2)^2\right]\left[(\Delta\omega-\omega_m)^2 + (\Gamma/2)^2\right]}, \tag{3.30}$$

with Γ being the linewidth of the cavity. The A- and D component of the signal are both plottet in Fig. 16. The D-component has a large and steep slope making it sensitive to changes in the cavity output, making it useful as the error signal.

When $D(\Delta\omega) = 0$, constructive interference of the field coupled in is supported in the cavity. A feedback loop can then be employed to push the system back to its desired state, i.e., adjust the cavity length that supports constructive interference, whenever $D(\Delta\omega)$ differs from zero.

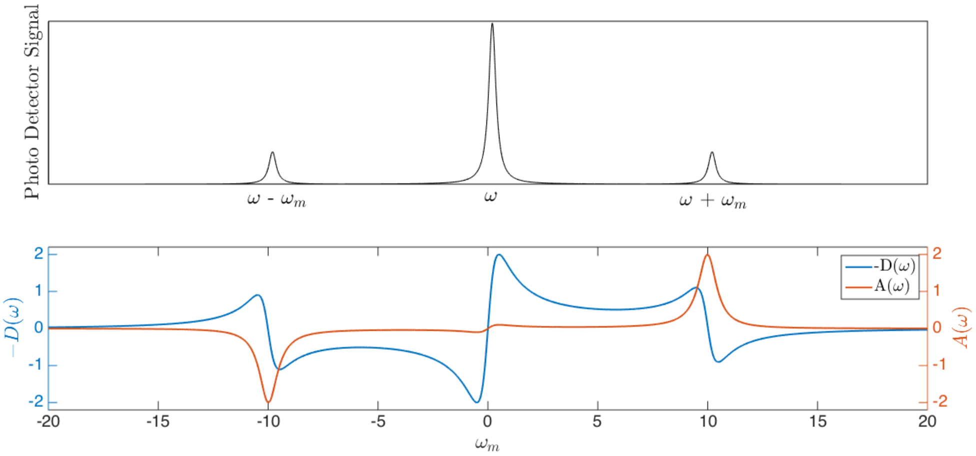

Figure 16: A simulated PDH signal: The top frame shows the transmitted signal as picked up by the PD denoted $\mathrm{PD}_{\mathrm{trans}}$ in Fig. 14. The two sidebands are located at ± $\Delta\omega$ arise from the frequency modulation. The bottom frame show the A(ω)- and -D(ω) components of the PDH error signal. The parameters used are ω_m = 10 MHz and Γ=1/10ω_m.

3.3 Cavity-Enhanced Absorption Spectroscopy

Optical cavities plays an important role in the experiment performed in this thesis. Optical cavities can serve to enhance spectroscopic signals, as the many roundtrips made by the light trapped inside the cavity effectively enhance the interaction with the sample of interest. Traditionally, when performing saturated absorbtion spectroscopy as shown in Sec. 2.1.1, the signal-to-noise ratio can only be enhanced by either having a very large sample, or by operating at high pressure to ensure a high sample density.

Cavity Enhanced Absorption Spectroscopy (CEAS) is a clever way of performing saturated absorption spectroscopy without compromising the compactness of the setup and still eliminate the Doppler broadening discussed earlier, as the interrogation beam overlaps with itself. The basic idea is to place the sample of interest in an optical cavity, typically in a Brewster cut cell as pictured in Fig. 17 or as a cloud of laser cooled atoms. Due to the nature of the experiment performed in this thesis, all future coverage on CEAS will assume a sample cell is being used. When a sample cell is introduced into a cavity, additional losses are introduced with it. These, along with experimental details are discussed in sec. 6.4. The absorption signal, as in conventional saturated absorption measurements, depends on the number of absorbing molecules, which can be varied by modulating the internal cell pressure. The molecular absorption is denoted as α in Fig. 17.

When employing CEAS it is possible to have both a compact setup with a small sample while still lowering the pressure, due to an effective enhancement of the interrogation length by the cavity. This opens the opportunity to have a setup that will show both great performance, but also be compact. This chapter will introduce the physics of CEAS and present the idea and realization of a beam expander cavity that allows for further reduction of broadening effects. Additionally, CEAS allows for the employment of the NICE-OHMS technique, which will be elaborated in Sec. 4.1.

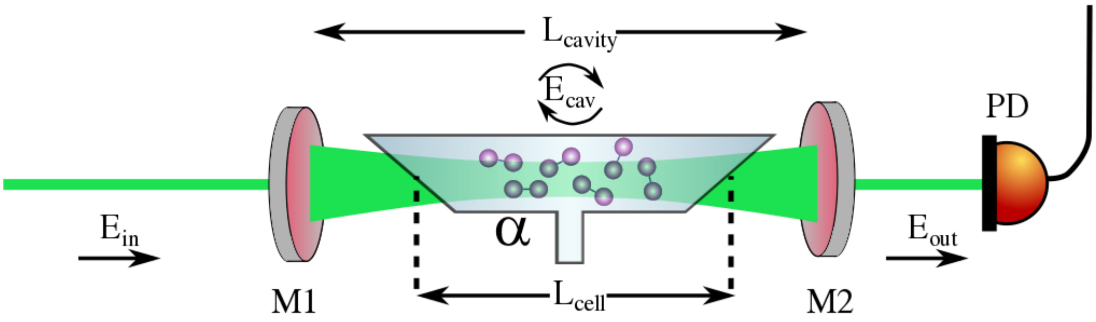

Figure 17: CEAS setup. A sample cell with a weakly absorbing vapor is placed inside a cavity. The absorption through the sample is denoted α and is given in units if inverse lenght, m^{-1} . A field is coulped into the cavity to interact with the sample and the spectroscopic signal is recorded by monitoring the cavity output. The cavity serves to enhance the interrogation length of the sample. The finesse of the cavity is heavily dependent on the number of absorbing molecules, as the sample introduces extra loss when absorbing the photons.

3.3.1 Enhanced Power & Interrogation Length

Due to the field building up inside the cavity the intra cavity power will be enhanced compared to the power in coupling power [2]:

$$\frac{P_c}{P_{in}} = T\left(\frac{1}{T+A}\right)^2, \tag{3.31}$$

where P_c is the intra-cavity power, P_{in} is the power coupled into the cavity, T and A holds the mirror transmission and absorption and scattering off the mirrors, P_c is the intra-cavity power, and P_{in} is the power coupled into the cavity. Comparing this to eq. (3.18), we find:

$$F = \frac{\pi}{T+A}, \tag{3.32}$$

which implies:

$$T + A = \frac{\pi}{F}, \tag{3.33}$$

resulting in:

$$P_c = P_{in}T\frac{1}{(\pi/F)^2} = P_{in}T\frac{F^2}{\pi^2}, \tag{3.34}$$

i.e., the power build-up in the cavity is proportional to the transmission times the finesse over π squared. This make it possible to acheive saturated spectroscopy even at low input power.

The interaction length of a sample is enhanced by an order of the finesse. If a cell of length $\mathrm{L_{cell}}$ filled with a weakly absorbing material with absorption coefficient α, and a beam of power P_{in} pass through, the output power with detected will be:

$$P_{out} = P_{in}e^{-\alpha \mathrm{L_{cell}}} \approx P_{out}\left(1 - \alpha \mathrm{L_{cell}}\right), \tag{3.35}$$

where in the last approximation the absorption is assumed weak. α is given in units of inverse length, m^{-1}. If the same sample is placed inside a cavity, the power transmitted by the cavity can be written including the extra loss introduced by the cell:

$$\begin{aligned} \frac{P_t}{P_{in}} &= \left(\frac{T}{T+A+\alpha \mathrm{L_{cell}}}\right)^2 \\ &\approx \left(\frac{T}{T+A}\right)^2\left(1 - 2\frac{\alpha \mathrm{L_{cell}}}{T+A}\right) \\ &= \left(\frac{T}{T+A}\right)^2\left(1 - 2\frac{F}{\pi}\alpha \mathrm{L_{cell}}\right). \end{aligned} \tag{3.36}$$

Where in the second line the expression is Taylor expanded around $\alpha \mathrm{L_{cell}} \approx 0$, i.e., the absorption is weak. This implies that the absorption signal arising from the sample is enhanced by a factor of $2F/\pi$. This corresponds to enhancing the sample length. The enhanced interrogation length may allow for lower sample density, i.e., lower internal pressure in the cell, and therefore limit pressure broadening, which will be discussed in the following section, along with other broadening effects present in CEAS systems.

3.3.2 Broadening Effects

Transit time broadening is a broadening effect that is well known from both conventional absorption measurements and CEAS. It is present in systems where the lifetime of the absorber is longer than the interaction time with the interrogation field. The interrogation time is determined by the transit time of the molecules through the field, hence the name. The transit time is given by $T = 2w/v$, where w is the waist of the beam and v is the speed of the absorber. The associated broadening is given by [12]

$$\delta\omega_{TT} = 2\frac{v}{w}\sqrt{2\ln(2)} = 2\pi\delta\nu_{TT}. \tag{3.37}$$

If the transit time broadening is to be reduced, the molecular velocity must be reduced, or the beam waist must be increased. In CEAS experiments using thermal gasses, the broadened linewidth of the absorbers is typically of the order of hundreds of kHz.

The *pressure broadening*, also known as collisional broadening, linked to the density of the molecular sample, which, if it is too high, will result in molecules colliding. Collisions peturb the molecules, leading to frequency shifts and broadening. An increase in pressure will increase the molecule density, and thus the number of molecules and thereby the number of collisions. The line profile of a pressure broadend absorber is Lorenztian. At low pressures, the pressure broadening relevant for the work done in this thesis can be described using [17]:

$$\Gamma(P) = \Gamma_0 + aP, \tag{3.38}$$

where Γ_0 is the natural linewidth, P is the pressure of the sample vapor, and a is given in units of kHz/Pa and is thus a broadening coefficient. Typically a will have a value of a few hundred kHz/Pa [1], which in low-pressure samples, i.e. $P \leq 1$ Pa will result in a pressure broadening of 1-100 kHz. The magnitude of the pressure broadening present in the system investigated in this work is discussed in Sec. 6.5.

Power broadening, also known as saturation broadening, becomes relevant, when the excitation rate becomes greater than the relaxation rate, which results in a decrease in the number of absorbing molecules, which will increase the rate of stimulated emission in the sample. The absorption close to resonance will decrease, whereas far from resonance it will remain the same, i.e., the spectral line measured is decreased in size and broadenend. The power broadened linewidth is given by [10]:

$$\Gamma_s = \Gamma_0\sqrt{1 + S_0}, \tag{3.39}$$

where Γ_0 is the natural linewidth, and the saturation parameter S_0 is given by:

$$S_0 = \frac{I}{I_{sat}}, \tag{3.40}$$

where I_{sat} is the saturation intensity, i.e., the intensity at which the population in the excited state is equal to that in the absorbing state. At $I = I_{sat}$, the total broadening of the line profile is $\sqrt{2}\Gamma$. For an absorber with a natural linewidth of 100 kHz, this means that the power broadened linewidth at $I = I_{sat}$ would be broadened to $\sim$ 140 kHz. An alternative way to consider power broadening is to consider the Heisenberg uncertanty relation. When stimulated emission is present the life time of the state is reduced. From $\Delta E \Delta t \geq \hbar/2$, we see that the energy uncertainty necessarily must increase when the life time decrease.

3.4 Beam Expander Cavity

With the broadening effects introduced in the previous section in mind, the following section is dedicated to the conceptual introduction of a new cavity design that will serve to ensure reduction in both transit time broadening, and potentially also pressure broadening, when performing CEAS. Most optical cavities do not support large beam waists, which can make transit time broadening, ν_{TT}, a limiting factor. This broadening effect can be reduced by either reducing the mean velocity of the sample, i.e., cooling it, or by expanding the waist size of the interrogating field. The schemaitcs of the cavity designed is shown in Fig. 18.

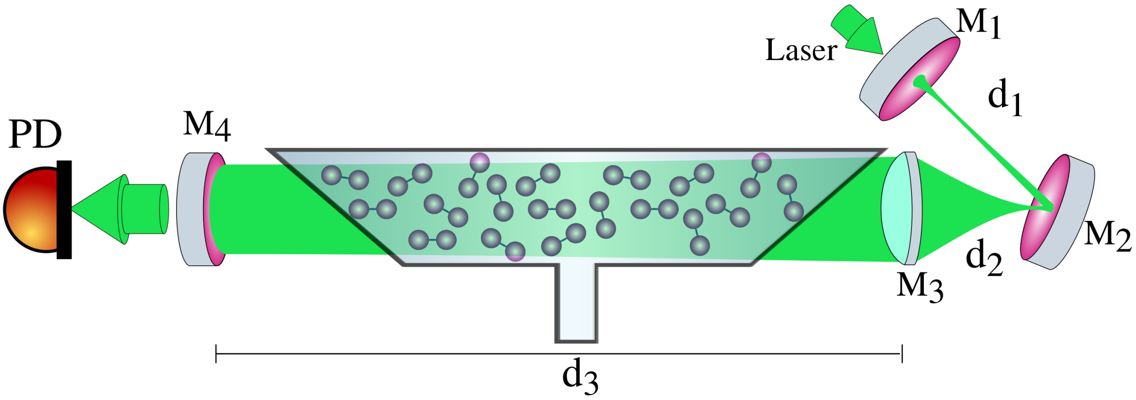

Figure 18: Schematics showing the contept of a folded beam expander cavity. The curved mirror, M_2, along with the lense at M_3, works as a telescope that expands the beam by a factor of 10 compared to conventional cavities as the one showed in Fig. 11. The cavity is sensitive to the angle at which it is folded, as well as the position of mirror M_2. The cell is introduced in this figure to emphasize the impact the large waist has on the number of molecules being interrogated compared to the setup shown in Fig. 17. The figure is adapted from [11].

In this configuration, a curved mirror (M_2) with focal length f = 12 mm, i.e., ROC = 24 mm, is combined with a plano-convex lens (M_3) with f = 200 mm, working as an intra-cavity telescope. The distances d_1 and d_2 can be varied to adjust the size of the beam in the spacing between M_3 and M_4, where the spectroscopy takes place. The setup is especially sensitive to the distance d_2. The stability and waist size as a function of intra-telescope distance and d_1 and d_2 can be seen in Fig. 19. The last distance, d_3 can be varied without having much impact on the stability, making it possible to tune the FSR of the setup. A core feature of the setup, is the fact that the beam is kept small at the M_2 interface. This helps reduce astigmatism in the beam that proved to be a limiting factor in earlier trial setups designed to support large beam waists.

The plot in Fig. 19 showing the stability as a function of intra-cavity telescope distance was calculated using $\lambda = 532$ nm though the intended wavelength to be used in the experiment performed in this thesis is 515 nm, the stability should not vary much. The advantage of setup shown in Fig. 18 is not only its ability to support a large beam waist, but also the compactness.

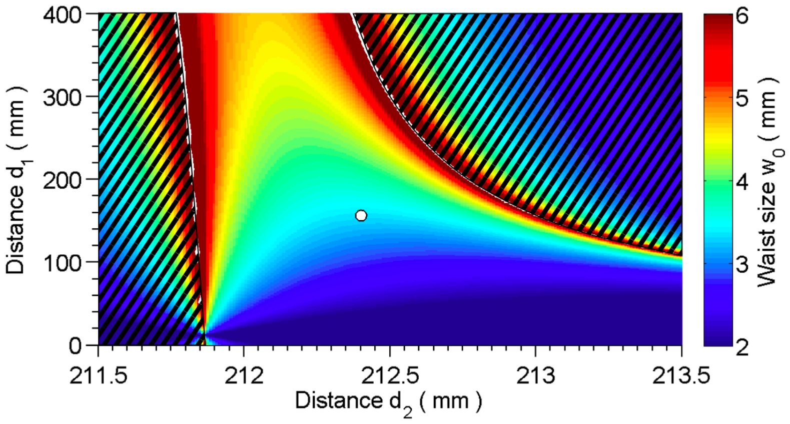

Figure 19: Waist size as function of intra-cavity telescope spacing and d_1. A plot showing the stability and waist size of the cavity as a function of the intra-cavity telescope spacing where the striped areas are within the unstable region. These calculations were performed for 532 nm. The white dot shown in this plot corresponds to the parameters used in the setup realized, and yields a waist size of 3.5 mm. This is roughly a factor of 10 higher than in conventional cavities. Figure from [11].

3.4.1 Realization of the Beam Expander Cavity

The beam expander cavity as shown in Fig. 18 was realized and testet using a 532 nm laser. The folded setup showed great performance, while still being compact. The finesse of the beam expander cavity is limited by the number of surfaces, as it is given by:

$$F \approx \frac{\pi\sqrt{\prod_{i=1}^{n} R_i}}{1-\prod_{i=1}^{n} R_i}, \tag{3.41}$$

where n is each surface encountered by a photon in the cavity. $\prod_{i=1}^{n}$ means taking the product of all the mirror reflectances. The transmission T of the lense enters on equal footing as R of the mirrors. M_1 and M_4 has a reflectivity of R = 0.998 and 0.995, respectively, while the lense has a transmission of T = 0.995 and the curved mirror at M_3 had R = 0.999. This yields a theoretical finesse of 157 for an empty cavity, i.e., with no sample cell present. The measured finesse of the empty cavity was 139, see Fig. 20.

The experimentally measured finesse in reasonable correspondence with the theoretically predicted, and the slight difference may be due to alignment or mode matching. Another suspect of the lowering of the finesse is the fact that the end mirror at M_4 fell of the piezo it was glued to more than once, which may have compromised the reflectance of the mirror.

The relatively high finesse, compared to the number of surfaces encountered, does however suggest that the setup does not suffer much from astigmatism in spite of the extra optical components added and the large beam waist.

When a sample cell is introduced into the cavity additional loss is also introduced. These stem partly from the sample itself in terms of absorption, but also from the loss associated wil the cell windows. Taking these into account, it is fair to expect pronounced degrading in the finesse of the cavity. Therefore, one is interested in acheiving a relatively high empty

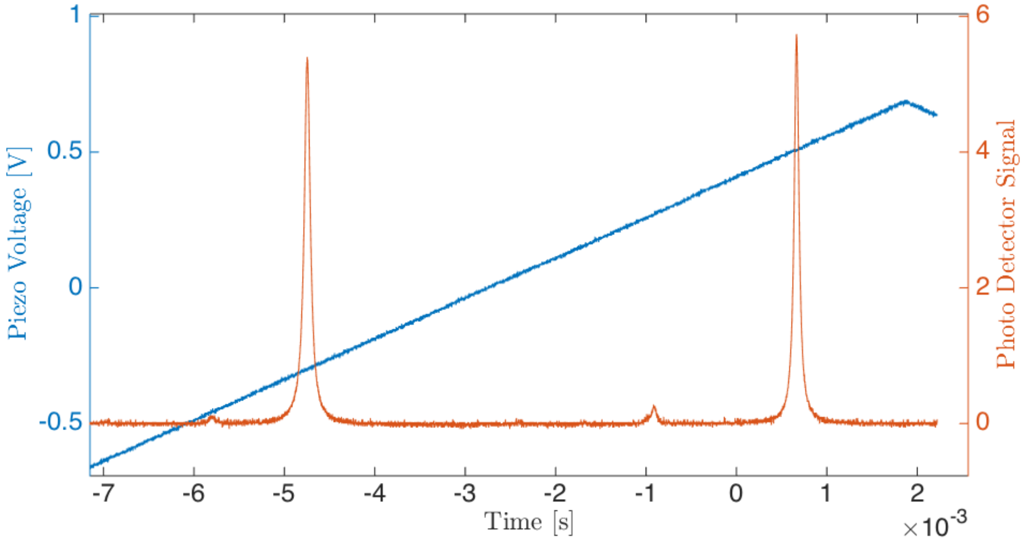

Figure 20: Cavity output. The finesse was measured by measuring the ratio of the FWHM of the transmitted peaks to the FSR of the cavity. The data was obtained by scanning the length of the cavity while monitoring the output. The length was varied by applying voltage over a piezo electric crystal mounted to the outcoupling mirror. The blue curve shows voltage applied to a piezo, i.e., the change in cavity length. The orange signal is the power measured by a PD.

cavity finesse to ensure that the finesse of the combined cavity-cell system is suffiecient for CEAS measurements. If optical components with higher mirror reflectance and higher lense transmission are used, a higher finesse is acheivable, see Table 1. The impact of introducing a cell into a cavity is discussed in Sec. 6.4.

The waist size of the folded configuration was also measured directly by image analysis perfomed in MATLAB, yielding a waist size of 3.44 ± 0.06 mm, in great correspondence with the theoretically predicted waist size of ≈ 3.5 mm, Fig. 19.

Finesse	
R = T = 0.998	R = T = 0.999
285	523

Table 1: Different examples of the theoretical finesse of the folded cavity using different quality off the shelf optical components. When a cell is introduced into the cavity additional losses arise. Therefore, to ensure a cavity-cell system that has a finesse sufficeint for CEAS, the empy cavity itself should support a relatively high finesse.

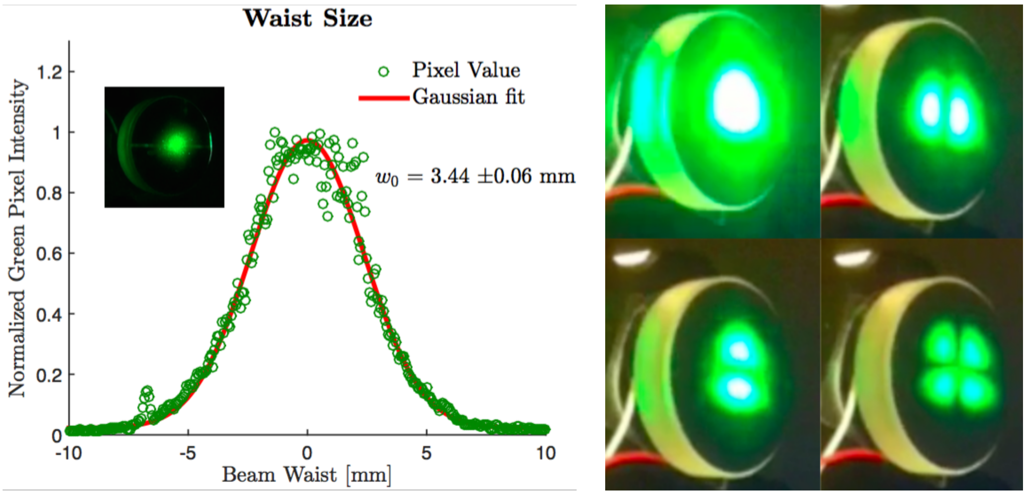

(a) **(b)**

Figure 21: (a) Measured waist size. The data was obtained by analyzing the picture shown in the inset of the graph in MATLAB. There is a great compliance between the measured waist size of 3.44 ± 0.06 mm, and the one predicted by theory yielding ≈ 3.5 mm. (b) Different cavity modes in the beam expander cavity. The pictures obtained clearly show the TEM-modes simulated in Fig. 78 in Appendix A. The large, visible modes served as a great tool for rough alignment.

4 FM Spectroscopy

So far, measurement techniques designed to measure the spectral linewidth and limit the effects of spectral line broadening have been introduced. But, in order to lock a laser to an atomic- or molecular transition, the phase shift originating from the interaction between the sample and the interrogating field must be detected. As discussed in the previous sections, an error signal used to stabilize given system must be odd and have a steep slope in order to be used in a feed back loop. The phase obtained from the radiating dipole approximation introduced in Sec. 2.1 has a form adequate for locking.

Frequency-Modulation Spectroscopy (FM Spectroscopy) is a commonly-used experimental technique when performing phase measurements. Measuring the phase of an optical fields is inherently challenging, as the oscillations are extremely fast (in the THz regime) and technically difficult to pick up with standard laboratory equipment. One solution to this problem is *Optical Heterodyne Detection*. The scheme is as follows: a beam is split into two different paths - one propagating through the sample of interest, noted as the interrogating beam, and the other through an empty pathway, denoted as the reference beam. The interrogating beam will undergo a phase shift as it interacts with the sample, whereas the reference beam remains unchanged. The two beams are then recombined on a PD, that will detect the squared sum of the two fields. A generic example of a hereodyne detection setup is shown in Fig. 22.

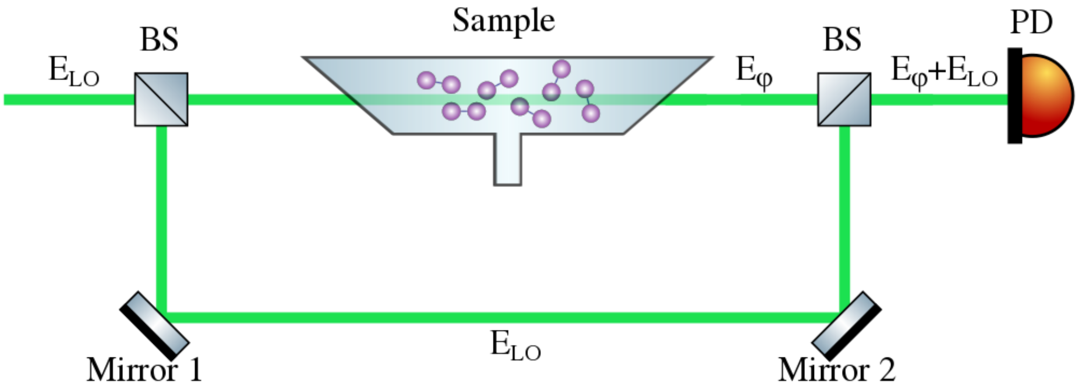

Figure 22: Schematics of a heterodyne detection scheme. The interrogating field is denoted $\mathrm{E_{LO}}$, as it works as a local oscillator. The beam is split into two paths using a beam splitter (BS). One propagating through the sample of interest with corresponding field E_ϕ, and one working as a reference propagating through an empty path. The two beams are recombined such that the toal field now consists of the sum of $\mathrm{E_{LO}}$ and E_ϕ. The corresponding signal picked up by the PD is proportional to the square of sum of the two fields, i.e., $i_{\mathrm{PD}} \propto |\mathrm{E_{LO}}+\mathrm{E}_\phi|^2 = |\mathrm{E_{LO}}|^2+|\mathrm{E}_\phi|^2+2\mathrm{E_{LO}}\mathrm{E}_\phi$. The last term containing the product of the two fields is used for phase detection.

When performing heterodyne detection the interrogating laser is referred to as the local oscillator, hence the interrogating field is denoted $\mathrm{E_{LO}}$. The field interacting with the sample is denoted E_ϕ. The phase sensitive signal is generated by overlapping the two fields incident on a PD:

$$\begin{aligned} i_{\mathrm{PD}} &\propto |(\mathrm{E_{LO}} + \mathrm{E}_\phi)|^2 \\ &= |\mathrm{E_{LO}}|^2+|\mathrm{E}_\phi|^2+2\mathrm{E_{LO}}\mathrm{E}_\phi. \end{aligned} \tag{4.1}$$

The fast oscillating terms, $E_{\rm LO}^2$ and E_{ϕ}^2, are either filtered out using a low pass filter, or simply by the detector's own bandwidth. The signal obtained will thus originate from the beat signal generated by the product of the two fields.

This method of detection can be employed in order to measure the phase shift obtained by a field interacting with an absorbing sample. The interrogating laser, referred to as the local oscillator, oscillates with an angular freuqency ω_L, and the field can be described by a sinusoidal wavefunction $\sin(\omega_L t)$. The field interacting with the sample will obtain a phase shift from the sample denoted ϕ, and be described by a sinusoidal waveform $\sin(\omega_L t + \phi)$. The signal generated by the mixing on the PD then yields:

$$\begin{aligned} i_{\rm PD} \propto \sin(\omega_L t)\sin(\omega_L t + \phi) &= \frac{1}{2i}\left(e^{i\omega_L t} - e^{-i\omega_L t}\right) \cdot \frac{1}{2i}\left(e^{i(\omega_L t+\phi)} - e^{-i(\omega_L t+\phi)}\right) \\ &= -\frac{1}{4}\left(e^{i(2\omega_L t+\phi)} - e^{-i(2\omega_L t+\phi)} + e^{-i\phi} - e^{i\phi}\right) \\ &= -\frac{1}{4}\left(\sin(2\omega_L t + \phi) + \sin(-\phi)\right). \end{aligned} \tag{4.2}$$

The term oscillating at $2\omega_L + \phi$ is filtered out using a low pass filter or simply averages to zero due to the limited bandwith of the common PD. Exploiting the fact that $\sin(-\phi) = -\sin(\phi)$, we can rewrite:

$$i_{\rm PD} \propto \frac{1}{4}\sin(\phi). \tag{4.3}$$

If the phase shift is small, the signal is directly proportional to the phase shift:

$$\lim_{\phi\to 0}\sin(\phi) \approx \phi. \tag{4.4}$$

The phase can then be used as an error signal for locking a laser to an atomic- or molecular transition. Heterodyne detection is in itself a powerfull tool since, in principle, it should only be sensitive to the phaseshift induced by sample. But in reality, the interrogating- and reference beam will pick up phase noise from the various different optcial components used when realizing the setup, which will compromise the signal. The phase noise can be eliminated by using the NICE-OHMS measurement technique, which will be introduced in the following section.

4.1 NICE-OHMS

Noise-Immune Cavity-Enhanced Optical-Heterodyne Molecular-Spectroscopy, abbreviated as NICE-OHMS, is an efficient measurement technique which can be employed alongside performing CEAS. Instead of detecting the absorption, the NICE-OHMS scheme is sensitive to the molecular induced phase. In the this section the schematics of a NICE-OHMS setup as used in the experimental work of this thesis is presented along with a conceptual and mathematical description of the technique.

One of the limitations to heterodyne detection described in the previous section is the phase noise arising from the surroundings. If a phase shift is picked up by the reference beam from any of the optical components, it will corrupt the purity of the beat note signal.

The NICE-OHMS technique circumvents this limitation by having both the reference- and interrogating beam travel through the same spatial path, thus obtaining the same accumulated phase noise originating from the cavity. This is possible due to frequency

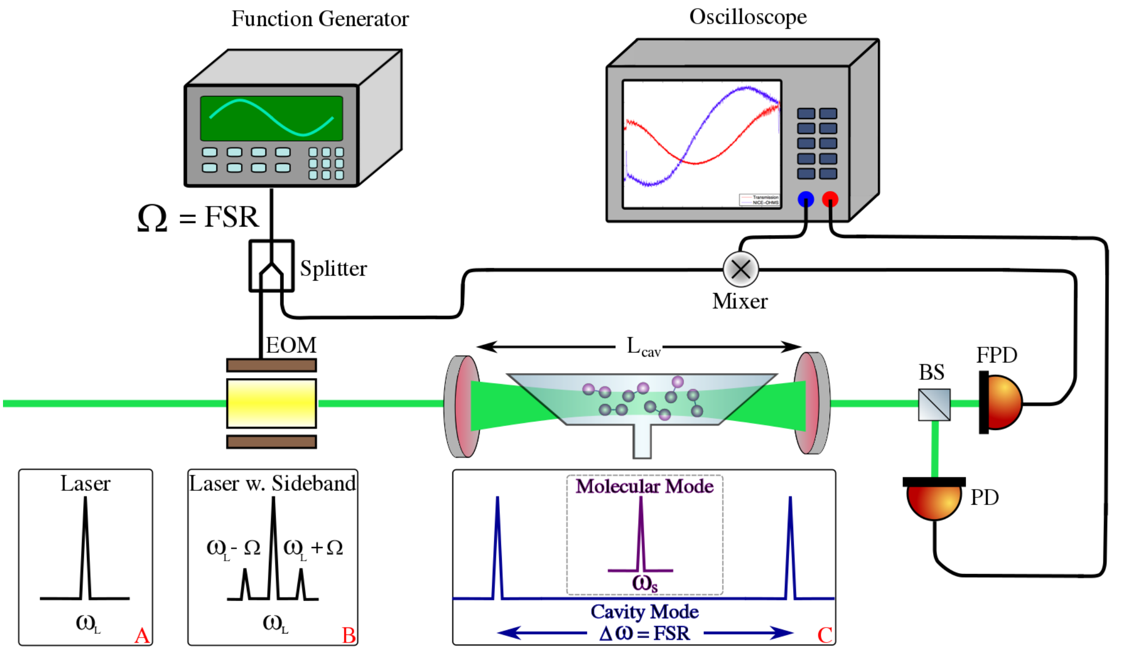

Figure 23: Schematics of the NICE-OHMS technique. The NICE-OHMS technique relies on frequency modulation of the interrogating laser that intially has a single frequency component at ω_{L}, box A. This is done by generating sidebands by letting the beam pass through an EOM before being coupled into the cavity, box B. The modulation frequency Ω is chosen such that the modulation frequency corresponds to the FSR of the interrogation cavity. This ensures equal support of the carrier beam and the sidebands by the cavity. The frequency of the interrogating field is scanned such that is is on and off resonance with the molecules, but the sidebands remain off resonance, leading to a phase shift between the carrier frequency and the sidebands. In box C the frequency of the molecular transition is shown along with the modes supported by the cavity separated by one FSR. When scanning the molecular resonance, the length of the cavity is changed such that the interrogation beam experiences constant constructive interfererence. The cavity works as a signal enhancer of both the phase signal and the saturated absorption signal. The CEAS signal can be obtained simply by monitoring the cavity transmission, whereas the NICE-OHMS signal is obtained by de-modulating the signal with the modulation frequency. This reproduces the beat signal between the carrier and the sidebands that is phase sensitive.

modulation of the interrogation beam. Before entering the cavity, sidebands are generated using an EOM as in the PDH locking scheme introduced in Sec. 3.2. The modulation frequency is chosen such that it is equal to one FSR defined by the cavity. This means that both carrier- and sidebands are resonant with the cavity. When the carrier is scanned over the molecular resonance it picks up a phaseshift. The sidebands propagate undisturbed due to their displacement in frequency. The phase sensitive signal is then picked up by mixing the cavity output signal with the modulation frequency. This is shown in Fig. 23. In Fig. 24 the modes in the cavity along with the molecular mode is shown. While the interrogation beam is scanned over the molecular resonance, the cavity is locked such that the cavity length is changed in order to support constructive intereference of both the interrogation beam and the sidebands at all times. As in CEAS measurements, the signal obtained when using NICE-OHMS benefits from the increased measurement sensitivity by a factor of F/π [2].

The separation in frequency between the carrier and the sidebands is in the radio fre-

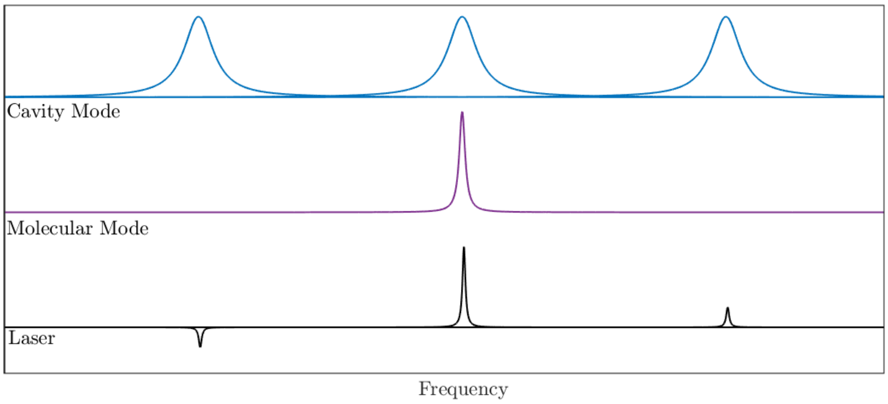

Figure 24: Concept of the measurement technique used in NICE-OHMS. The interrogation laser is scanned accros the molecular resonance. While scanning the laser frequency, the cavity is locked such that the interrogating laser frequency is supported by the cavity at all times. When the laser is on resonance with the molcules, the carrier will pick up a phase shift, while the sidebands propagate undisturbed. The phase sensitive signal is generated by beating the signal transmitted by the cavity with the modulations frequency.

quency (RF) regime, leading to another benefit of using NICE-OHMS. The intrinsic noise in electronic equipment, e.g., a photodector goes as $1/f$, where f is the frequency of the signal recorded, in this case the beat signal. This means that noise in the detected signal will be virtually eliminated as the FSR of the typical optical cavity is of the order of several hundreds of MHz.

In order to describe the system mathematically, we may consider the inital field with angular frequency ω_L prior to frequency modulation:

$$E = E_0 \exp\left(i\left(\omega_L t\right)\right) + c.c., \tag{4.5}$$

where E_0 is the field amplitude. The frequency spectrum of the unmodulated field is shown in box A in Fig.23. Before entering the cavity, the light is coupled through an EOM. The EOM generates sidebands by applying a sinusoidal voltage over a optically active crystel as described in Sec.3.2. The modulation frequency is chosen to match the FSR of the cavity. Describing the modulated field using Bessel functions, we find:

$$E_{mod} = E_0\left[J_0(\delta)e^{i\omega t} + J_1(\delta)e^{i(\omega+\Omega)t} - J_1(\delta)e^{i(\omega-\Omega)t}\right] + c.c., \tag{4.6}$$

where $\Omega = FSR$. The carrier frequency with its sidebands is pictured in box B in Fig. 23. The beam is then coupled into the cavity where it can interact with the molecuar sample.

The phase shift of the interrogating field when ω_L is tuned such that i matches ω_s is denoted ϕ. This, along with the attenuation due to absorption, leads us to write the resulting field as:

$$\begin{aligned}
E &= E_0\left[e^{-\alpha}J_0(\delta)e^{i(\omega t+\phi)} + J_1(\delta)e^{i(\omega+\Omega)t} - J_1(\delta)e^{i(\omega-\Omega)t}\right] + c.c.\\
&= E_0[J_0(\delta)e^{-\alpha}(e^{i(\omega t+\phi)} + e^{-i(\omega t+\phi)})\\
&\qquad + J_1(\delta)(e^{i(\omega+\Omega)t} + e^{-i(\omega+\Omega)t})\\
&\qquad - J_1(\delta)(e^{i(\omega-\Omega)t} + e^{-i(\omega-\Omega)t})]\\
&= 2E_0\left(J_0(\delta)e^{-\alpha}\cos(\omega t+\phi) + J_1(\delta)\cos((\omega+\Omega)t) - J_1(\delta)\cos((\omega-\Omega)t)\right),
\end{aligned} \tag{4.7}$$

where α is a dimensionless attenuation due to absorption in the sample. The signal picked up by the photo diode is proportional to the power of the transmitted field. The field transmitted by the cavity is described in Sec. 3.1 by:

$$E_T = E\frac{t_1 t_2 e^{-i\phi_{cav}}}{1 - r_1 r_2 e^{-i2\phi_{cav}}}, \tag{4.8}$$

where $\phi_{cav} = \omega\frac{L}{c}$ is the cavity induced phase, which is derived in Appendix A. The cavity induced phase ends up cancelling when monitroing the power, i.e., $|\mathrm{E}_T|^2$, as derived in Sec. 3.1. Therefore, the cavity induced phase will be omitted in the following derivations. The power detected by the photodetector is proportional to the field squared, leading to:

$$\begin{aligned}
i_{PD} &\propto P \propto |E|^2\\
&= 4E_0^2\left[J_0(\delta)e^{-\alpha}\cos(\omega t+\phi) + J_1(\delta)\cos((\omega+\Omega)t) - J_1(\delta)\cos((\omega-\Omega)t)\right]^2\\
&= 4E_0^2[J_0^2(\delta)e^{-2\alpha}\cos(\omega t+\phi) + J_1^2(\delta)\cos^2((\omega+\Omega)t + J_1^2(\delta)\cos((\omega-\Omega))\\
&\qquad + 2J_0(\delta)J_1(\delta)e^{-\alpha}\cos(\omega t+\phi)\cos((\omega+\Omega)t)\\
&\qquad - 2J_0(\delta)J_1(\delta)e^{-\alpha}\cos(\omega t+\phi)\cos((\omega-\Omega)t)\\
&\qquad - 2J_1^2(\delta)\cos((\omega+\Omega)t)\cos((\omega-\Omega)t)].
\end{aligned} \tag{4.9}$$

The expression in eq. (4.9) rewritten using:

$$\cos(A)\cos(B) = \frac{1}{2}(\cos(A-B) + \cos(A+B)). \tag{4.10}$$

From this, we express the photo current as:

$$\begin{aligned}
i_{PD} \propto & 4E_0^2[J_0^2(\delta)e^{-2\alpha}\cos(\omega t+\phi) + J_1^2(\delta)\cos^2((\omega+\Omega)t + J_1^2(\delta)\cos((\omega-\Omega))\\
&+ J_0(\delta)J_1(\delta)e^{-\alpha}\left(\cos(\Omega t+\phi) + \cos((2\omega+\Omega)t+\phi)\right)\\
&- J_0(\delta)J_1(\delta)e^{-\alpha}\left(\cos(-\Omega t+\phi) + \cos((2\omega-\Omega)t+\phi)\right)\\
&- J_1^2(\delta)\left(\cos(2\Omega t) + \cos(2\omega t)\right)].
\end{aligned} \tag{4.11}$$

The signal transmitted by the cavity is picked up by a Fast Photo Diode, FPD, and demodulated by Ω using a mixer, as shown in Fig. 23. The signal is thus only sensitive to terms oscillating in the vicinity of the de-modulations frequency, meaning that the fast oscillating terms will not contribute to the signal. This gives:

$$\begin{aligned}
i_{PDmod} &= i_{PD} \times \cos(\Omega t + \theta_M)\\
&= \cos(\Omega t+\theta_M) \times 4E_0^2[J_0(\delta)J_1(\delta)e^{-\alpha}\cos(\Omega t+\phi)\\
&\qquad - J_0(\delta)J_1(\delta)e^{-\alpha}\cos(-\Omega t+\phi)\\
&\qquad - J_1^2(\delta)\cos(2\Omega t)]\\
&= 2E_0^2[J_0(\delta)J_1(\delta)e^{-\alpha}\left(\cos(\theta_M-\phi) + \cos(2\Omega t+\theta_M+\phi)\right)\\
&\qquad - J_0(\delta)J_1(\delta)e^{-\alpha}\left(\cos(2\Omega t+\theta_M+\phi) + \cos(\theta_M+\phi)\right)\\
&\qquad - J_1^2(\delta)\left(\cos(3\Omega t+\theta_M) + \cos(-\Omega+\theta_M)\right)].
\end{aligned} \tag{4.12}$$

Here, $\cos(\Omega t + \theta_M)$ is the demodulation signal and θ_M is the relative demodulation phase. Assuming $\theta_M = \pi/2$, and exploiting that:

$$\cos(A + B) = \cos(A)\cos(B) - \sin(A)\sin(B), \tag{4.13}$$

and employing a low pass filter we find the de-modulated photodetector signal:

$$\begin{aligned} i_{PDmod} &\overset{\text{lowpass}}{=} 2E_0^2 \left[J_0(\delta) J_1(\delta) e^{-\alpha} \cos(\theta_M - \phi) - J_0(\delta) J_1(\delta) e^{-\alpha} \cos(\theta_M + \phi) \right] \\ &\overset{\theta_M = \pi/2}{=} 4E_0^2 J_0(\delta) J_1(\delta) e^{-\alpha} \sin(\phi). \end{aligned} \tag{4.14}$$

Usually the attenuation of the field can be assumed to be weak, such that $e^{-\alpha} \approx 1$ and the phaseshift small giving $\sin(\phi) \approx \phi$, making eq. (4.14) expressed as:

$$i_{PDmod} \approx 4|E_0|^2 J_0(\delta) J_1(\delta) \phi. \tag{4.15}$$

The NICE-OHMS signal is thus phase sensitive and can be used as an error signal for laser stabilization. The NICE-OHMS technique thus makes it possible to exploit the benefits of cavity enhancement of the light-matter interaction, without the cavity phase corrupting the molecular induced phase shift. As already mentioned, the saturated absorbtion signal can be extracted along with the NICE-OHMS signal. In Fig. 23, the NICE-OHMS signal is shown as the red curve, and the saturated absorption signal is shown as the blue curve.

In Fig. 25, the NICE-OHMS signal and the saturated absorption signal is simulated for an artifical sample. Both the saturated absorption signal and the NICE-OHMS signal sit ontop of a Doppler broadened background.

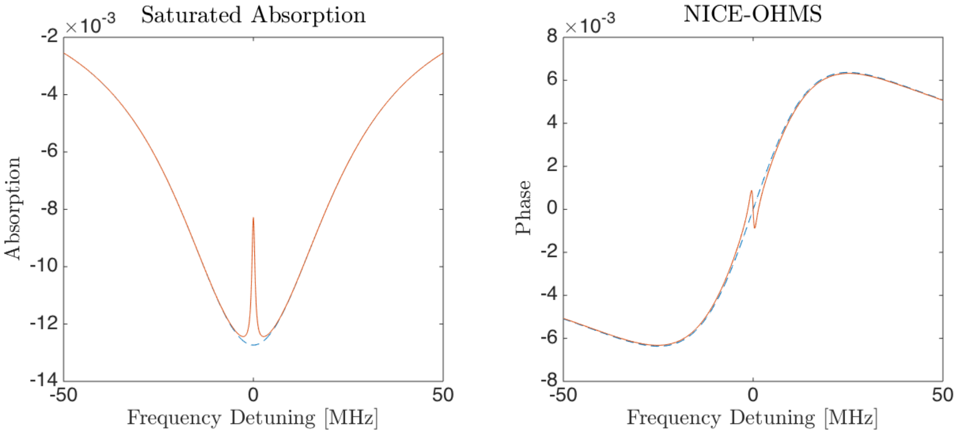

Figure 25: A simulated example of a saturated absorption signal (left) and a NICE-OHMS signal (right). The blue dashed curve show the Doppler broadened absorption and phase, respectively, where as the orange curve show the saturated absorption and the phase shift of the sarurated profile. Both the saturated absorption and the NICE-OHMS signal sit on top of the broadened absorption and phase. Here the Doppler broadened profile is fifty times wider than the natural linewidth but in reality it is often several orders of magnitude wider.

The molecular induced phase shift can be expressed as the imaginary part of the Fourier transform of the damped oscillator introduced in Sec. 2.1. The Fourier transfrom is given by:

$$\begin{aligned} A(\omega) &= \frac{U_0}{2} \frac{-i(\omega - \omega_0) + \frac{\Gamma}{2}}{(\omega - \omega_0)^2 + (\frac{\Gamma}{2})^2} \\ \phi \propto \arg(A(\omega)) &= \frac{U_0}{2} \frac{\omega - \omega_0}{(\omega - \omega_0)^2 + (\Gamma/2)^2}. \end{aligned} \tag{4.16}$$

U_0 is the oscillating amplitude corresponding to the field strength, ω is the angular frequency of the interrogating field, ω_0 is the frequency of the transition, and finally Γ is the width of the transition. As discussed earlier the limited amount of absorbers contributing to the saturated signal descrease the signal size compared to the broadened feature. This holds true also in the NICE-OHMS case.

The general feature of the absorption is dominated by the Doppler broadened induced phase shift, but due to the setup exploiting saturated absorption, the molecules with a zero-velocity component in the beam direction contribute to a narrow feature near resonance, which can be measured by the NICE-OHMS signal. This ensures the steepness of the slope compared to the Doppler broadened background. The slope of the induced phase near resonance detected by the NICE-OHMS signal arising from the saturated absorber's transition can be used as an error signal for laser stabilization.

FM spectroscopy may also be used to monitor the saturated absorption signal by monitoring the sidebands located at $\pm 2\Omega$. This is beyond the scope of this project, and only a few of the benefits of this approach is listed. The signal obtained will be proportional to measured absorption, but will suffer less from electronic noise compared to measuring just the transmitted signal, due to the displacement in frequency, reducing the $1/f$ noise. This method of measuring can be performed simultaneously with NICE-OHMS detection. Impressive results with this detection scheme have been obtained and reported in [30].

5 Iodine

With the measurement and experimental techniques in place, it is time to introduce a candidate for a thermal frequency reference: Iodine.

To most people, iodine is a liquid substance mainly encountered as a disinfectant for cuts and wounds, or as an additive to ordniary kitchen salt. But iodine has played an important role within optical physics for decades due to its strong and plentiful absorption lines.

In solid form, iodine is a black, almost metallic looking granulate that bleeds purple when dissolved in water, see Fig. 26. The colour purple is what originally gave name to the element, as iodine is derived from the greek word *ιοειδής* [*ioeidēs*], meaning purple.

(a) **(b)**

Figure 26: Solid iodine, and iodine dissolving in water.

The iodine used in this thesis was in gassious form, i.e., a vapor. The iodine vapor is, as the liquid solvent, slightly purple. The isotope used is $^{127}I_2$, which is 100% naturally abundant, as all other isotopes are synthesized [20].

The sample is held inside a glass cell (Sec. 6.3). Iodine constitue an interesting candidature as a thermal molecular clock due its optical properties introduced in the following sections. In general, the optical transitions in iodine narrows faster than the transition strength decreases in the 500-520 nm regime [6]. The hyperfine transitions in iodine have a reported linewidth of just 48 kHz [6], even in a thermal vapor, making iodine a very promising candidate in realizing a thermal optical frequency reference.

5.1 Iodine: A Thermal Frequency Reference

As emphasized in sec. 2.1 the use of atomic- and molecular optical frequency references constitute the pinnacle in terms of precision and stability. This, however, comes at a price of complex and expensive experimental setups, making the use in, e.g., space applications difficult. The need for compact and simple atomic- and molecular clocks serves as the primary motivation for the work done in this thesis. As the work in this thesis has been carried out in iodine, this section is devoted to present the advantages of using iodine as the frequency reference.

Iodine is no stranger in the clock making business. The molecule has roughly 60 000 fine structue lines in the region between $\sim$ 500 nm to 900 nm, [10]. The International Bureau of Weights and Measures, BIPM, has adapted the results obtained by [7] and [6] as the primary standard at $\lambda = 514.673$ nm in the P(13)43-0 manifold. Iodine has long been a favourite when perfoming spectroscopy due to the transition strength making signals easily obtainable. The energy level structure, which ultimately set the foundation for a future frequency reference, is introduced and explained in the following section.

5.1.1 Energy Level Structure

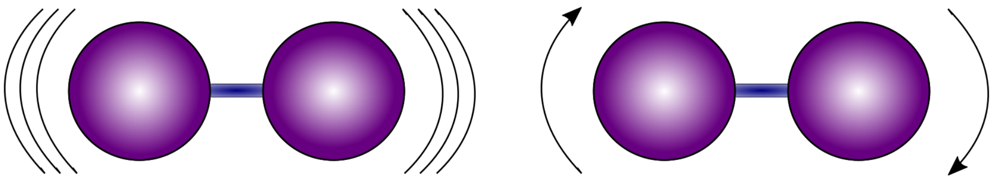
(a) Vibrational **(b)** Rotational

Figure 27: Diatomic molecule modelled as a dumbbell. Molecules are inherently more complex in structure than atoms simply due to the fact that they are build up by two or more atoms. Therefore, additional motional degrees of freedom turn up, such as vibrations (a) and rotations (b), with associated energy levels. The vibrational energy level stem from the spacing between the two iodine atoms varying slightly making the whole molecule vibrate. The rotational energy level stem from the molecule rotating around itself. Both can be combined, such that the molecule is both rotating and vibrating at the same time.

The energy level structure in molecules is in general more complex than those in atoms. This is due to the extra degrees of freedom that arise when the structure of the molecules become more complicated than that of the atoms. The energy level structure is attributed to three main mechanism: The electronic state of the molecule, vibrations and rotations. The two latter often combine to form rovibrational states.

The quantum numbers describing the state are as the following:

The spin of the molecule can be assumed to consist of the two individual atom spin vecors $\bar{S_1}$ and $\bar{S_2}$, such that the total spin value of the molecule is described by $S = S_1 + S_2, S_1 + S_2 - 1, ..., |S_1 - S_2|$.

The orbital angular momentum of the molecule is quantised with respect to the symmetry line of the molecule, i.e., the line of sight between the two atoms. The resulting electronic orbtial angular momentum is defined as Λ, and takes on values of $\Lambda = 0, 1, 2, 3, ...$, and the molecular states are labeled accordong to Λ, as $\Sigma, \Pi, \Delta, \Phi$ etc, analagous to the labeling the atomic states.

As with atoms, where the total angular momentum J i sdescribed through $\bar{L}$ and $\bar{S}$, the total angular momentum of the electrons is described using $\bar{\Omega}$, which is described through $\bar{\Lambda}$ and $\bar{S}$, i.e., the spin and orbital angular momentum of the molecule. The symmetry of the electronic wavefunction is either odd or even. For even symmetry the total electronic angular momentum is denoted as $\Omega = 0^+, 1^+, ...$, etc., and for odd total electronic angular momentum $\Omega = 0^{-}, 1^{-}, ..$, and so forth.

For a molecule consisting of two identical atoms, the center of symmetry is located half way between the atoms. In this system, the inversion of electronic coordinates will not change the sign of the electronic wavefunction, which is either even or odd. In this special case, the symmetry of the electronic wavefunction is denoted by a "g" if it is even, and a "u" if it is odd. The diffierent electronic states are referred to as X for the ground state, and A, B, C,..., etc., for higher lying electronic states. There is no consesus of what order the letters labelling the different states follow, making the labelling appear somewhat random at times [10].

The whole molecular system is described quantum mechanically using the wave equation:

$$H\psi_n = E_n\psi_n = \left\{ \frac{-\hbar^2}{2\mu}\nabla_R^2 - \sum_{i=1}^{N} \frac{-\hbar^2}{2m} + V(R; r_1; ..r_N) \right\} \psi_n = E_n\psi_n, \tag{5.1}$$

where n denote the n'th state and R is the radial distante from the source to the observation point. The first term arise from the kinetic energy of the nuclei with reduced mass μ, and the second arise from the kinetic energy of the electrons. $V(R; r_1 ... r_N)$ is the potential in which the molecule sits. The kinetic energy of the of the nuclei is made up of contributions arising from the molecule vibrating and rotating. Before deriving these expressions, the Born-Oppenheimer approximation is introduced. In this approximation, it is assumed that the energy attributed to the electronic state can be used to describe the potential of the nuclei wavefunction. This is based on the fact that the motion of the nuclei can be assumed stationairy compared to that of the electrons, since the atomic mass is much higher than the electron mass.

To describe the potential arising from the electron, a few assumptions can be introduced. In a diatomic molecule, the two atoms are held together through the sharing of valence electrons. This can be intepreted as the atoms being held together by a spring force, with spring constant k_e. This is pictured for a simplified artifical molecule in Fig. 28.

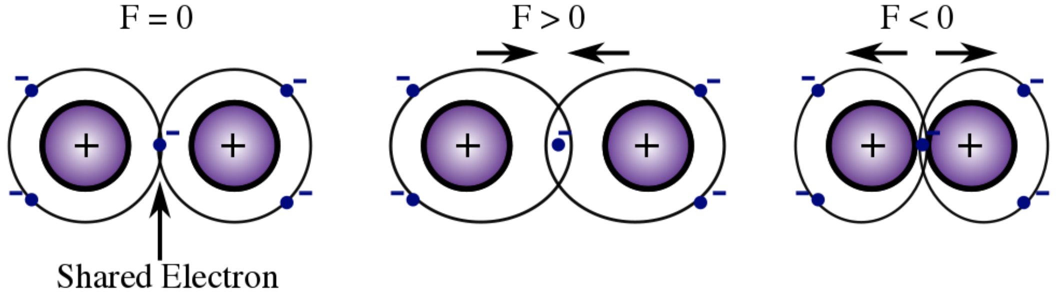

Figure 28: A simple schematics showing the force holding an artificial molecule together. The two nuclei share a valence electron lying in the outermost band (the others are not shown). The nuclei will naturally find a steady state separation, where the repelling and attracting forces cancel out, i.e., F = 0. If the nuclei are bein pulled appart, the binding force from the electron will work to pull the nuclei back, and when being pushed togehter, the force will work to repell them. The force can be thought of as a spring force.

If the spring is being compressed, it will work to seperate the two atoms, but when pulling the atoms away from each other, the spring will work to pull them back together. In between both extremums lies an equilibrium denoted x_0. The potential describing the binding force between the two atoms is approximated by the anharmonic Morse potential [21]:

$$V(x) = D_e \left(1 - e^{-\alpha(x-x_0)}\right)^2, \tag{5.2}$$

D_e is the dissoiation energy, i.e., the energy it takes to separate the two atoms at $x \to \infty$, and defines the depth of the well. $\alpha = \sqrt{\frac{k_e}{2D_e}}$, where k_e is the spring, or force, constant between the atoms. The Morse potential is plotted in Fig. 29.

Using eq. (5.2) as the potential in the wave equation of the nuclei, and write out the kinetic part of the Hamiltonian in spherical coordinates, we find:

$$\frac{-\hbar^2}{2M}\nabla_R^2 = \frac{-\hbar^2}{2M}\frac{1}{R^2}\frac{\partial}{\partial R}(R^2\frac{\partial}{\partial R}) + \frac{L^2}{2MR}, \tag{5.3}$$

where we have assumed that the molecule is composed of two identical atoms, i.e., $\mu \to M$. The last term holds the rotational energy of the atom.

The rotational part of the Hamiltonian arise when the molecule rotate around itself. This can be modelled as a dumbbell, as in Fig. 27b, rotating around the center-of-mass. From the theory of quantum mechanics [21], the eigenvalues of the L^2 operator makes it possible to write:

$$E_J = \frac{\hbar^2}{2I}J(J+1). \tag{5.4}$$

Including the effect of vibration in eq. (5.4), and rewriting in terms of wave numbers, the final expression is found [9]:

$$E_J = \hbar\left[B_e - \alpha_e(v + \frac{1}{2})\right]J(J+1) - \hbar D J^2(J+1)^2. \tag{5.5}$$

The values for B_e, α_e and D can be found in [20], and determine to what degree the different terms contribute. Most commonly, D is small enough to be neglected completely. v is the vibrationel quantum number an is described in the following.

The vibrational contribution is found using the first term in eq. (5.3). Due to the molecule vibrating, it is shifted from the equilibrium at x_0. By Taylor expanding the potential around $x = x_0$, the potential seen by a vibrating molecule can be expressed as:

$$\begin{aligned} V(x) &= V(x_0) + (x-x_0)\left(\frac{dV}{dx}\right)_{x=x_0} + \frac{1}{2}(x-x_0)^2\left(\frac{d^2V}{dx^2}\right)_{x-x_0} + ... \\ &= V(x_0) + \frac{1}{2}k_e(x-x_0)^2 + A(x-x_0)^3 + B(x-x_0)^4.., \end{aligned} \tag{5.6}$$

where $V(x)$ is the Morse potential described in eq. (5.2). By incuding higher order terms, the potential becomes more and more anharmonic. The constants A and B holds the weight of the anharmonic contributions. For simplicity, $V(x_0)$ is set to 0. This results in energy levels written on the form [9]:

$$E_v = \hbar\omega_e\left[(v+\frac{1}{2}) - x_e(v+\frac{1}{2})^2 + y_e(v+\frac{1}{2})^3 + ...\right], \tag{5.7}$$

with $v = 0, 1, 2, 3, ..., n$, describe the vibrational quantum number. ω_e is expressed in wavenumbers, i.e., cm^{-1}. In [20] the constants for ω_e and $\omega_e x_e$ are listed for the electronic ground state.

The combined energy of the whole system is thus given by:

$$E = E_e(R) + E_v + E_J. \tag{5.8}$$

$E_e(R)$ is the electronic energy arising from the morse potential.

The electronic energy magnitude is usually a few eV, and can be estimated as [21]:

$$E_e \approx \frac{\hbar^2}{2ma}, \tag{5.9}$$

where a is the the average distance between the nuclei in the molecule, i.e., of the order of Åand m is the electron mass. The energy is equvalent to transitions in the optical range. The vibrational energy E_v can be estimated by:

$$E_v = \sqrt{\frac{m}{M}} E_e. \tag{5.10}$$

As the nuclei mass is much larger than the electron mass, i.e., $M \gg m$, meaning that the energy associated with the vibrational state of the molecule is much lower than the electronic, and thus vibrational transitions resides in the infrared regime. Finally, the rotational energy of the molecule can be estimated by:

$$E_J \approx \frac{m}{M} E_e, \tag{5.11}$$

again, taking into account that the nuclei mass is much larger than the electronic, this means that rotational energy is in the microwave regime.

An example of the energy structure in a di-atomic molecule in the electronic ground state is given in Fig. 29. The spacing between rotational energy levels will become smaller and smaller as J increases. One will find various rotational levels in the spacing between vibrational levels. States that both rotate and vibrate are also present, but not depicted in the figure.

As with atomic systems, not all transitions are allowed. This was already mentioned in the beginning of this section, and will be ellaborated further in the following: The transition between two different energy states are denoted E'' for the inital state energy, and E' for the final state energy. The selection rules of the J^2 operator dictates that $\Delta J = J' - J'' = 0, \pm 1$. Depending of the value of ΔJ, the transitions are divided into three branches: A Q-branch, a P-branch, and an R-branch. If $\Delta J = -1$ the transitions resides in the P-branch, and if $\Delta J = +1$ the transition is part of the R-branch. The P- and R-branches appear around the transition corresponding to $\Delta J = 0$, known as the Q-branch. A transition from one rovibronic state to another is labeled as P$(J'')v' - v''$ and R$(J'')v' - v''$, where P and R denote which branch the transition resides in.

Some of the selection rules that apply to iodine are listed in Table 2.

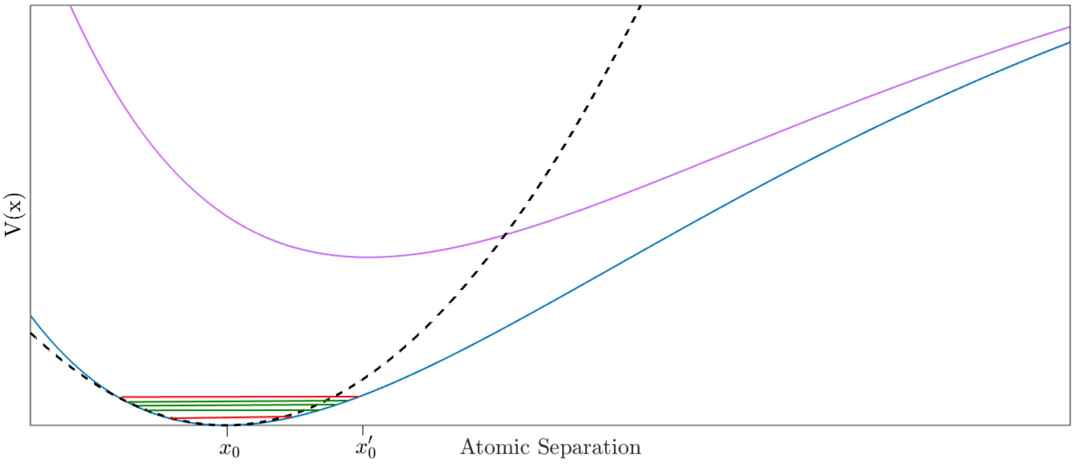

Figure 29: A graphic example of energy level spacing for a di-atomic molecule with an anharmonic Morse potential. The ground- and first excited electronic state are shown with the blue and purple curve, respectively. The full lines shows the anharmonic Morse potential, and the dashed line shows the harmonic approximation. In each potential lies several rotational (green) and vibrational (red) statse, though only the ones in the ground state are explicitly shown here. The spacing between the different state is reduced as the potential gets higher. The spacing between the vibrational states is larger than that of the rotational. Transitions between different electronic states are in the optical regime, where as vibrational resides in the infrared regime, and the rotational in the microwave regime. x_0 and x'_0 denote the separation at which equilibrium occurs for the ground- and excited state, respectively.

ΔΛ	=	0,±1	
±	↮	±	
g	↮	u	
ΔJ≡J'-J"	=	-1	(P-branch)
	=	0	(Q-branch; but not J'=0 ↮ J"0)
	=	+1	(R-branch)

Table 2: Table based on [10] showcasing the different selections rules for transitions in iodine.

5.2 P(13)43-0 Transition

The transistion of interest for the work done in this thesis is the rovibrational transition denoted P(13)43-0. As mentioned in Sec. 5.1.1, the ground electronic state is denoted X, and all higher lying electronic states is denoted A, B, C... etc. Following the formalism in [1], the transition of interest that happens between the electronic groundstate X to the first excited state B, is written as $B \leftarrow X$. The electronic states are labelled as following the $^{2S+1}\Lambda^{(+/-)_{g,u}}$ notation. The ground state is labelled $^1\Sigma_g^+$ and the first escited state is labelled $^3\Pi_u$ [1].

As the name indicates, the transitions resides in the P-branch. This means that $\Delta J = -1$, indicating that $J' - J'' = -1 = 12 - 13$, and $v' - v'' = 43 - 0$. The transition happens when the molecular vibrational state changes from the vibrational ground level to the 43rd vibrationally excited level, and the rotational level changes from the 12th to the 13th, between the electronic groundstate and the first excited state.

The transition has a transition energy equivalent to a frequency of 582 490 603 442 kHz, corresponding to light at $\lambda \approx 514.67$ nm, as denoted in Table 3. In the same table the spacing in frequency between the hyperfine components in the P(13)43-0 manifold are listed.

$\lambda \approx 515$ nm $^{127}I_2$ P(13)43-0					
a_n	$[f(a_n - f(a_3)]$/kHz	u_c/kHz	a_n	$[f(a_n) - f(a_3)]$/kHz	u_c/kHz
a_1	-131 770	1	a_{12}	435 599	3
a_2	-59 905	1	a_{13}	499 712	5
a_3	0	–	a_{14}	518 00	1000
a_4	76 049	1	a_{15}	587 369	2
a_5	203 229	5	a_{16}	616 756	5
a_6	240 774	5	a_{17}	660 932	5
a_7	255 005	1	a_{18}	740 000	1000
a_8	338 699	5	a_{19}	742 000	1000
a_9	349 717	5	a_{20}	757 631	10
a_{10}	369 000	1000	a_{21}	817 337	5
a_{11}	393 962	2			
Frequency Referenced to a_3, P(13)43-0, $^{127}I_2$: f = 582 490 603 442 kHz					

Table 3: Table based on [3]: All hyper fine components of the P(13)43-0 transition listed with respect to the a_3 component. The uncertainty with which each transition has been measured is denoted as u_c. The spacing in frequency between the different hyperfine transitions is given in kHz.

BIPM is currently basing the frequency reference at 582 490 603 442 kHz on the a_3 component of the P(13)43-0 manifold. This is based on measuremenst performed by [6] and [7]. The linewidth of the a_3 component is however of the order of $\sim$ 240 kHz FWHM [1], whereas the linewidth of the a_2 component has been reported having a linewidth of $\sim$ 48 kHz [6]. Therefore, the a_2 component is of great interest to use as a future reference at 514.67 nm.

The relative uncertainty of laser systems stabilized to the a_3 component in the P(13)43-0 manifold have obtained values of 8.6 $\times 10^{-12}$ [3]. The setup presented in Sec. 6 is designed to further improve, and at least match, this uncertainty by enhancment of the signal sensitivity and the elimination of broadening effects while stille keeping the setup compact. Other iodine based frequency refrences using 532 nm transitions has achieved a fractional uncertainty of 3 $\times 10^{-15}$ [8]. The hyperfine transitions in the vincinity of 532 nm have natural linewidths varying beteen 400-600 kHz (FWHM) [1]. With a system based on the even narower transitions in the P(13)43-0 manifold around 515 nm, it should be possible to surpass the system performance of the systems working at 532 nm.

5.3 Number of Molecules in the P(13)43-0 State

The number of molecules N_i in a sample of N molecules, occupying the P(13)43-0 state can be approximated using a Maxwell-Boltzmann distritution:

$$N_i/N = \frac{\exp(-E_i/k_BT)}{\sum_{j=0}^{\infty}\exp(-E_j/k_BT)}. \tag{5.12}$$

By assuming that the majority of the molecules will already be in the electronic ground state, we only concern ourselves with the different vibrational and rotational states. Further more, it is assumed that the rotational and vibrational states do not couple, as $\alpha \ll B_e$ [20]. The vibrational and rotational energy, as introduced in the previuous section, is given by:

$$\begin{aligned} E_v &= \hbar\omega_e\alpha(v+\frac{1}{2}) + \hbar\omega_e x_e\alpha(v+\frac{1}{2})^2 \\ &= \hbar\cdot 214.5(\mathrm{cm}^{-1})\alpha(v+\frac{1}{2}) + \hbar\cdot 0.61(\mathrm{cm}^{-1})\alpha(v+\frac{1}{2})^2, \\ E_J &= \hbar B_e\alpha(J\cdot(J+1)) \\ &= \hbar\cdot 0.03737(\mathrm{cm}^{-1})\alpha\cdot(J\cdot(J+1)), \end{aligned} \tag{5.13}$$

where $\alpha = 2.99792458 \cdot 10^{10}$ cm · Hz is introduced as a conversion factor from cm^{-1} to frequency. The different values used for ω_e, $\omega_e x_e$ and B_e have all been found in [20], and are written in terms of wavenumbers. Using these, and assuming $T = 300$ K, the number molecules occupying each possible vibrational- and rotational state is evaluated, see Fig. 30. From the figure, we see that it is fair to sum over $J = 0, 1, ..., 400$ and $v = 0, 1, ..., 20$, as the number of molecules fall of drastically. Rewritting the sum in eq. (5.12), and taking into account that the degeneracy of the J quantum number is $2(J + 1)$ we get:

$$\begin{aligned} N_i/N &= \frac{2(J+1)\exp(-(E_{v'=0}+E_{J'=12})/k_BT)}{2(J+1)\sum_{J=0}^{400}\sum_{v=0}^{30}\exp(-(E_v+E_J)/k_BT)} \\ &= 0.0025. \end{aligned} \tag{5.14}$$

This means that only about 0.25 % of the molecules will contribute to the spectroscopic signal.

5.4 Absorption Measurements

A series of absorption measurements at different coldfinger temperatures were carried out in order to determine the pressure dependent absorption of the iodine sample. These measurements were performed in two rounds, yielding two different results. The first set of measurements were performed on a sample that later was determined to be contaminated, denoted Sample 1. The same characterization was carried out in a new sample, denoted Sample 2. The relation between coldfinger temperature and internal vapor pressure is elaborated in Sec. 6.4.2.

The setup used to determine the absorption through the sample as function of internal vapor pressure, is shown in Fig. 31a alongside a photo of the setup in Fig. 31b. A tunable laser with a wavelength of $\lambda \approx 515$ nm pass through the 15 cm long iodine vapor cell. The signal is then picked up by a PD. The laser wavelength is scanned on and off resonance with the molecules in order to determine the absorption.

The coldfinger temperature, and thus the vapor pressure, is varied from -2.0 °C to -18.2 °C, corresponding to a variation in pressure from 3.35 Pa to 0.54 Pa in the measurements perfomed on Sample 2, and from -20 °C and 21 °C corresponding to a vapor pressure varying from 0.436 Pa to 32.42 Pa for Sample 1. The absorption was calculated by comparing the signal obtained while the laser is on resnonace with the molecules, with the

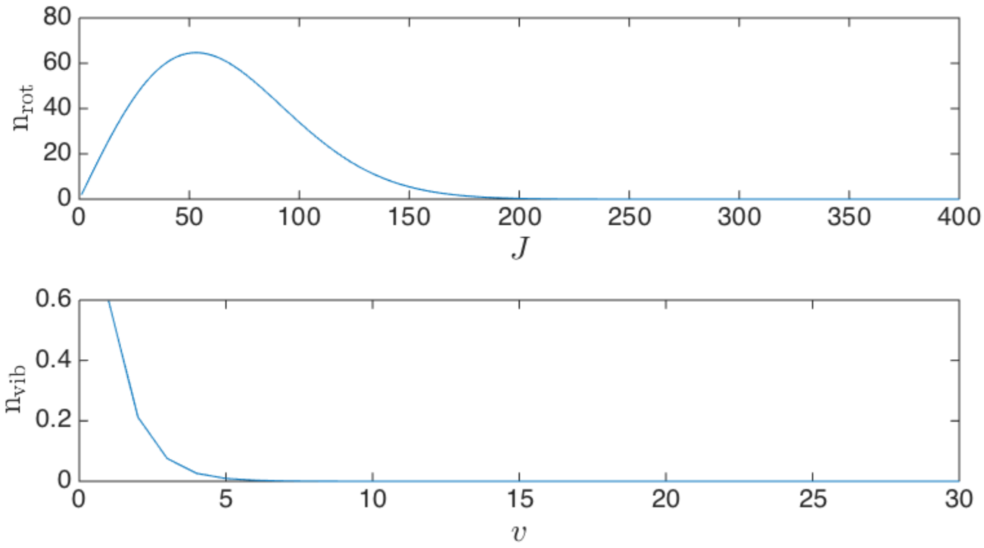

Figure 30: Number of molecules occupying each rotational and vibrational state. The probability of a molecule occupying a rotational state with $J \leq 200$ is approximately 0. The same goes for molecules occupying a vibrational state with $v \leq 10$. This justifies the approximation used in eq. (5.14), where $J = 0, 1, ..., 400$ and $v = 0, 1, ..., 30$. For the vibrational state, most molecules tend to be in the $v = 0$ state, and in the $J \approx 50$ state for the rotational states.

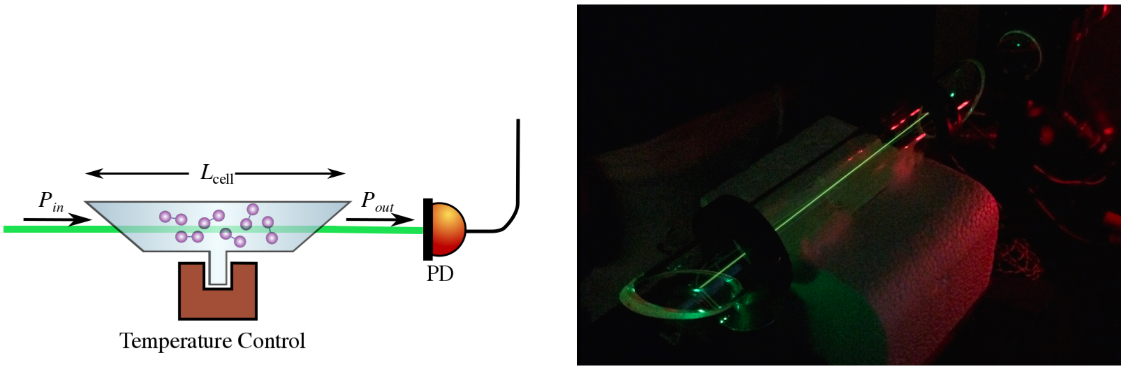

(a) **(b)**

Figure 31: Schematics of the absorption measurement being carried out (a), and a photograph of an absorption setup. The light is scanned on and off resonance with the molecules, in order to measure the maximum absorption.

signal measured with no absorption present. The signal measured when the light is being absorbed is given by:

$$P_{on} = (P_{in} - P_r) \exp\left(-\alpha_{\mathrm{P}} L_{\text{cell}}\right) - P_r, \tag{5.15}$$

where α_{p} is the absorption coefficient in units of $(\mathrm{Pa\ m})^{-1}$, and P_r is the power reflected from the cell windows (not explicitly shown in Fig. 31a). The measured signal off resonance is given by:

$$P_{off} = P_{in} - 2P_r. \tag{5.16}$$

By isolating P_r in eq. (5.16), and inserting into eq. (5.15), we get:

$$P_{on} = (P_{in} - P_{off}) \exp\left(-\alpha_{\mathrm{P}} L_{\mathrm{cell}}\right) - \frac{P_{in} - P_{off}}{2}. \tag{5.17}$$

The expression now holds only measurable quatities. From this, se absorption coefficient α is isolated:

$$\alpha_{\mathrm{P}} = \frac{-\ln\left(\frac{P_{in} - P_{off} + 2P_{on}}{P_{in} + P_{off}}\right)}{L_{\mathrm{cell}}}. \tag{5.18}$$

In Fig. 32 an example of the absorption profile measured in Sample 2 is given for two different temperatures. Before plotting the data, all background was measured and subtracted from the data.

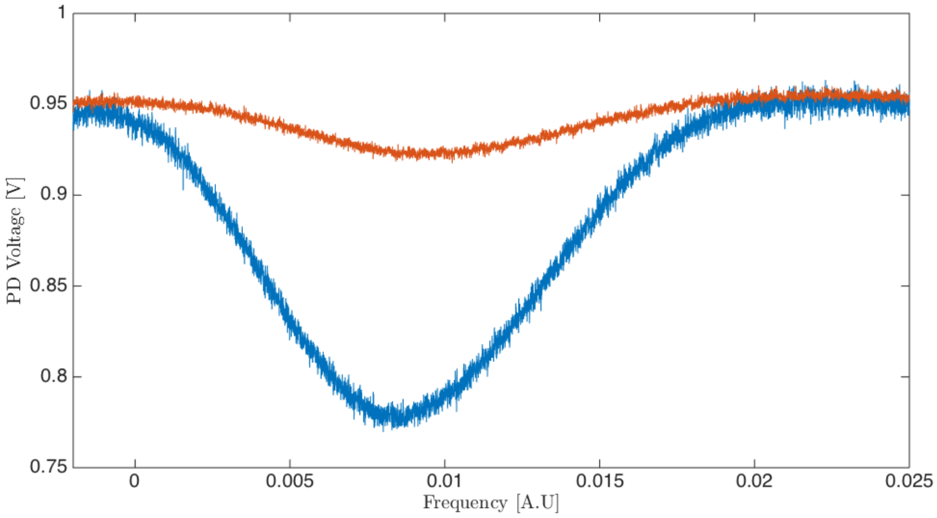

Figure 32: Data obtained from absorption measurements. The orange curve show the data collected for at a coldfinger temperature of -2.0 ^{o}C, and the blue the data obtained at -18.2 ^{o}C

P_{on} corresponds to a minimum in the transmitted signal, i.e., the light is absorbed by the molecules, whereas P_{off} corresponds to the maximum in the plot shown. The data shown in Fig. 32 is normalized to P_{in}. From this α_{P} as function of vapor pressure calculated from the data and fitted for Sample 1 and Sample 2.

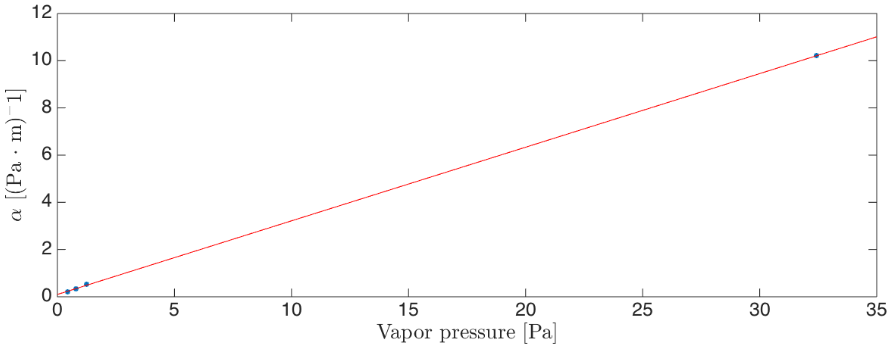

Figure 33: Data and fit from the absorption measurements performed on Sample 1. Due to limited temperature control of the coldfinger, the measurements were only carried out at four different vapor pressures. The fit yielded an absorption coefficient of $\alpha = 0.3119$ (m Pa)$^{-1}$.

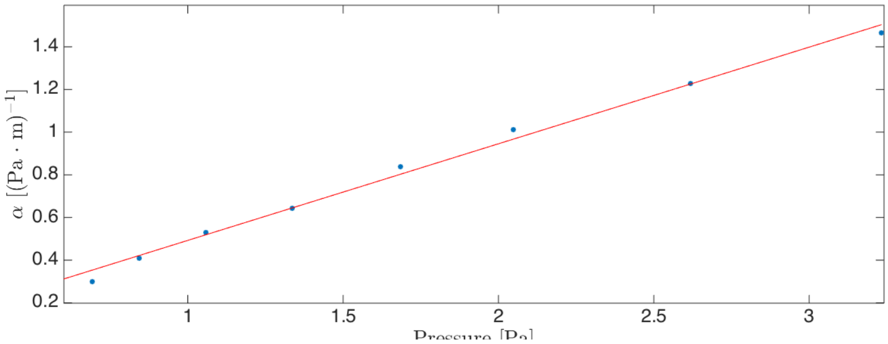

Figure 34: Data and fit from the absorption measurements performed on Sample 2. The data was collected at various coldfinger temperatures. The fit gave a an absorption coefficient of $\alpha = 0.4529$ (m Pa^{-1})

In Sample 1, the absorption was measured at four different temperatures due to limited temperature control. The fit obtained gave:

$$\begin{aligned}\alpha_{P,\text{Sample 1}} &= \alpha_{0,1} P_T + c_1 \\ &= 0.3119 \pm 0.002(\text{m Pa})^{-1} P_T + 0.09823,\end{aligned} \tag{5.19}$$

and for Sample 2 the fit yielded:

$$\begin{aligned}\alpha_{P,\text{Sample 2}} &= \alpha_{0,2} P_T + c_2 \\ &= (0.4529 \pm 0.016)\ (\text{m Pa})^{-1} \cdot P_T + 0.0397.\end{aligned} \tag{5.20}$$

P_T is the coldfinger temperature-dependent pressure. The absorption measured in Sample 1 is weaker than in Sample 2. This may be due to the fact that Sample 1 was contaminated. Though the number of measurements performed in Sample 1 is quite low, the obtained value for the absorption coefficient did fit nicely with measurements performed later on once the sample was placed inside an interrogation cavity, see Sec. 6.4.

6 The Experimental Setup

The experimental setup built during this thesis takes advantage of the techniques described in the previous sections, such as CEAS and NICE-OHMS. An overview of the setup is shown in Fig. 35.

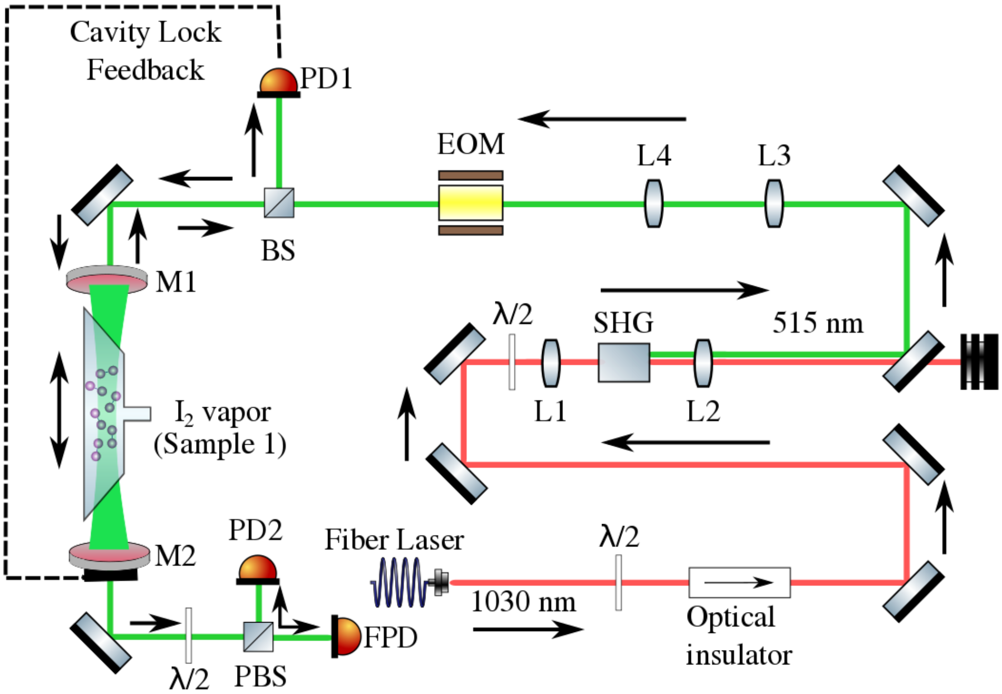

Figure 35: The experimental setup used for NICE-OHMS and CEAS detection. A fiber laser delivers light at 1030 nm that passes through an optical insulator to prevent backreflections into the fiber. The light is then beam shaped before entering the frequency doubling crystal, that generates the second harmonic at 515 nm. The green and infrared light are then separeted using a dichroic mirror. The green light light is beam shaped using the lenses at L3 and L4 in order to mode match the interrogation cavity. Before entering the cavity, the beam pass through an EOM, that generates sidebands for cavity locking and for NICE-OHMS detection. The error signal was generated using the PDH locking scheme, and picked up by the photodiode PD1. The beam splitter, BS, shown after the EOM separates the incomming field from the field reflected by the cavity. The error signal is then fed to the piezo-electric element (PZT) on the backside of the out-coupling mirror. The PZT change the cavity length to support constructive interference in the cavity for the light coupled in. When the light enters the cavity, it servers to enhance the interrogation signal as described in Sec. 3.3 and 4.1. The field transmitted by the cavity is separated into two paths using a polarized beam splitter, PBS. The NICE-OHMS signal is picked up by a fast photo diode, FPD. The demodulation of both the error- and NICE-OHMS signal is not explicitly shown in this figure. The saturated absorption signal is picked up by PD2 and is not demodulated. The black arrows indicate the direction of the light.

The Bureau International des Poids et Mesures (International Bureau of Weights and Measures), BIPM, has adopted the P(13)43-0a$_3$ transition in $^{127}I_2$ as the primary standard at 514.67nm [3] based on measurements perfomed by [6] and [7]. Both experiments have been performed as saturated absorption spectroscopy (SAS), see Sec. 5.4 and FM spectroscopy, on iodine vapor cells, making the signal limited by interaction length, i.e., cell length, and sample density, i.e., cell pressure.

In [7] they circumvent this issue by having a short cell of 8 cm kept at a relatively high temperetue of -5 °C, corresponding to a vapor pressure of 2.4, Pa making it compact but suffering from pressure broadening effects. In [6] the experiment is performed at very low pressure, 0.01-0.1Pa at the expense of compactness as the cell is 4 m long in order to compensate for the low molecule density. The trade off is thus either a large setup operating at low pressure, or a more compact setup working at a relatively high pressure. The work performed in this thesis aims to overcome the limitations set by vapor pressure and sample size, by placing the sample inside a cavity. As the cavity works as a signal enhancer, the whole setup can be kept rather compact without compromising the performance. The experiment is designed to make use of the NICE-OHMS technique and CEAS. The NICE-OHMS signal will work as a phase detection scheme which will be used as a lock for a frequency reference.

In order to perform PDH-locking and NICE-OHMS detection simultaneously, the EOM shown in Fig. 35 is modulated with two frequencies at the same time. One modulation frequency used for locking the cavity, and the other used to detect the molecular induces phase shift. Essentials in the setup include the NKT Koheras AdjustiK fiber laser, the frequency doubling crystal (SHG), the sample cell, and the sample cavity-cell system performance. These will be discussed in the following sections.

6.1 Laser Source: NKT Koheras AdjustiK

The laser used in this project is a NKT Koheras AdjustiK tunable fiberlaser working at ∼1030 nm. The laser has a linewidth $>$ 3 KHz specified by the manufacturer. The laser has a maximum power of ∼ 100 mW, and the power output is easily controlled through the display and setup menu in the front panel, see Fig. 36.

Figure 36: Front panel of the NKT Koheras AdjustiK fiber laser. All standard settings such as temperature- and power adjustments are controlled using the the dispay and designated buttons. The fiber itself is the blue fiber in the lower left corner of the panel. The fiber length is approximately 1.5 m.

The laser wavelength is tunable either through temperature control or through a built-in piezo electric crystal. The temperature tuning covers a larger spectral area than that of the piezo, as summarized in Fig. 37 and 39. The temperature is capable of tuning the wavelength from roughly 1028.85 nm to 1029.7 nm, and a change in temperature of 5 °C roughly corresponds to a change in wavelength of 0.1nm. The wavelength corresponding to the desired transition in iodine at 514.67 nm yields a wavelength of 1029.34 nm, which corresponds to a temperature of 39.66 °C.

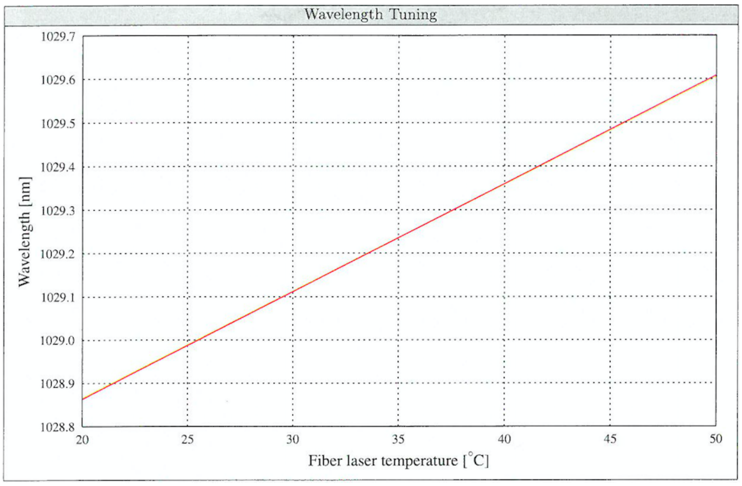

Figure 37: The fiber laser wavelength as function of internal fiber temperature. The temperature exhibits a wide tuning range of 0.85 nm, sufficient for the experiment performed in this thesis. A change in temperature of 5°C roughly corresponds to a change in wavelength 0.1 nm. This implies that the initial temperature setting of the laser is cruicial for performing any spectroscopic measurements. The figure is supplied by the manufacturer.

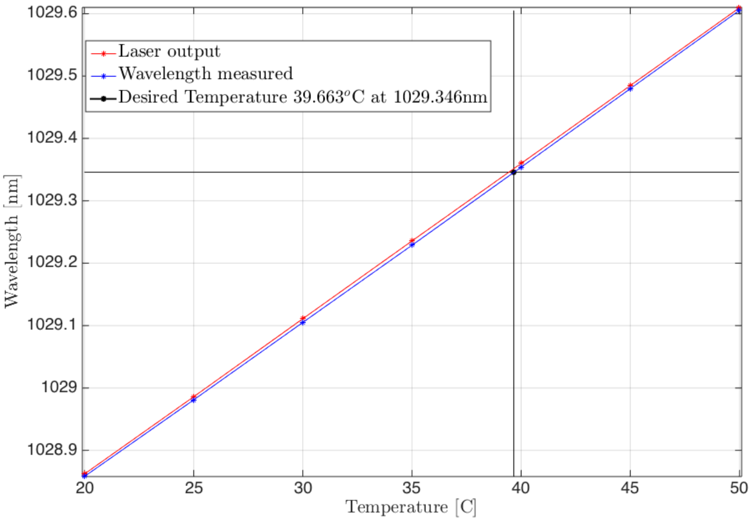

Figure 38: Control measurement of the laser wavelength as function of fiber temperature. The measured output show fine correspondence with that supplied by the manufacturer. The red curve show the output stated by the laser, and the blue curve show the wavelength measured. The point at which the black lines intersect is yields the temperatue needed to deliver ligth at 1029.34 nm.

A control measurement of the relation between wavelength and fiber laser temperature was performed. The measured output was compared to that specified by the manufacturer, and is shown in Fig. 38. The measured relation showed fine compliance with the information provided by NKT. The initialization of temperature is a rather slow process, since fluctations decrease slowly. Thus, the laser should be kept af the same temperature setting for roughly 5-10 minutes before performing any measurements to ensure a stable temperature and thus a stable laser output.

The piezo tuning, on the other hand, has a more narrow spectral range. The maximum voltage that can be applied to the piezo is 200 V. The whole tuning range is over 200 V is 15 pm, corresponding to a change in wavelength of 0.015 nm. A change of 1 V corresponds to a change in wavelength of 0.000075 nm. When scanning the laser over the molecular resonance, the piezo tuning is used.

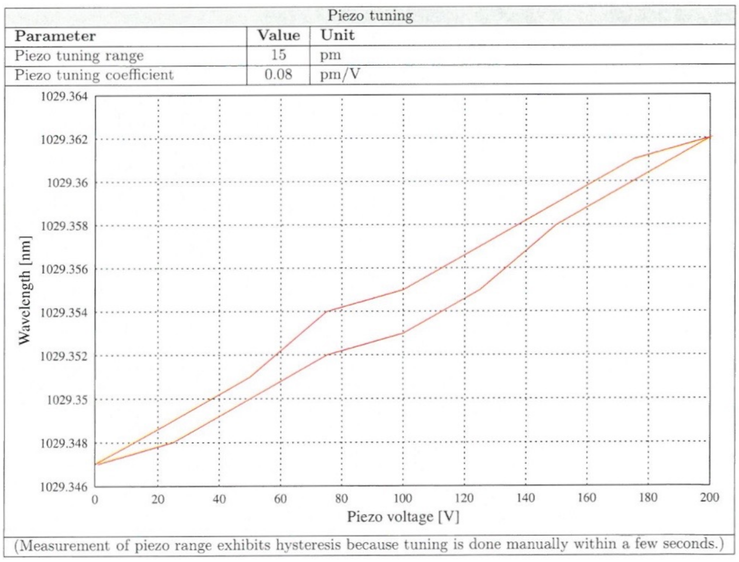

Piezo tuning

Parameter	Value	Unit
Piezo tuning range	15	pm
Piezo tuning coefficient	0.08	pm/V

(Measurement of piezo range exhibits hysteresis because tuning is done manually within a few seconds.)

Figure 39: A plot showing the wavlength as function of voltage applied to the piezo. The maximum voltage that can be applied is 200 V, which corresponds to at tuning range of 0.015 nm. According to the manufacturer, the hysteresis in the output stem from the manual tuning of the piezo voltage. The hysteresis has not been explicitly measured afterwards.

Despite having a very narrow linewidth, the laser exhibited a rapid frequency drift of roughly 20 MHz over the course of 1 s, compromising the experimental performance. It has not been possible to determine the cause of the frequency drift, but an external stabilizing setup was built in order to supress the drift of laser. This is disussed further in sec. 6.7.

6.2 Second Harmonic Generation

The P(13)43-0 transition has a transition energy equivalent to transition a wavelength of 514.67 nm. In this the P(13)43-0 manifold and a wide selection of hyperfine transitions are present, with linewidths as narrow as 48 kHz for the a_2 component [6]. In order to generate light that matches both the wavelength and is narrower than the transition linewidth, see Sec. 4.1, second harmoninc generation (SHG) was used. The linewidth of infrared fiber lasers can be made extremely narrow, in the few-kHz regime, [19], making it preferable to use SHG to generate light at the desired wave length as the generated second harmonic inherits the narrow linewidth.

Second harmonic generation is a second order nonlinear effect where light passes through a nonlinear medium, and two identical photons are combined to generate a new photon at twice the energy, i.e., twice the frequency thus at half the wavelength. Overall, nonlinar effects can be described as special cases where the presence of a field modulate the field itself, i.e., the induced polarization works as a source term. The theory behind SHG is thoroughly described in [16] and [9], and some of the derivation relevant for the calculations shown in this section can be found in Appendix B.

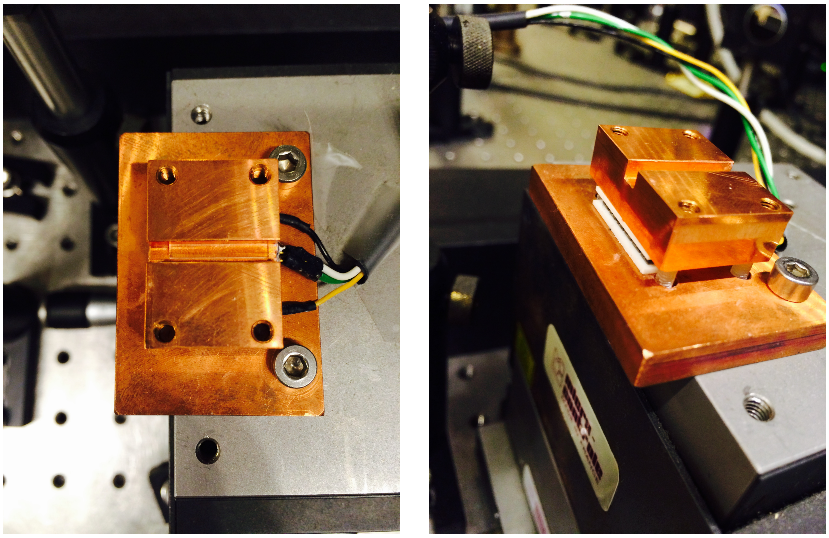

(a) **(b)**

Figure 40: The copper heatsink used to stabilize the temperature of the PPKTP crystal in order to ensure phase matching. The crystal itself is placed in the groove placed in the middle of the copper block. In order to eliminate excessive airflow around the crystal, a lid was placed on top. The lid is not included in this picutre. The copper block sits ontop of a peltier element, such that temperature control of the crystal was possible. A small thermistor is placed on the back side of the copper clock, close to the crystal. The temperature was controlled using a Thorlabs TEC 2000.

Green light at 515 nm was succesfully generated using a periodically poled potassium titanyl phosphate (PPKTP) purchased at Raicol. The crystal was placed in a copper block working as a heatsink for temperature stabilzation see Fig. 40. The temperature of the crystal is varied in order to secure phase matching between the k vector of the second harmonic, the real field and the quasi phase matching k-vector which is given by the crystal structure. This is derived in Appendix B. The power conversion efficiency was determined as function of both crystal temperature, i.e., phase matching, beam size and power.

The phase matching condition is controlled via. the temperature adjustments of the crystal, see Fig. 41. The maximum power of the generated second harmonic was found at T = 32.6 °C. This is the exact same value reported in [15] for the same crystal type.

The amount of power that is being converted is also dependent on the ratio between the

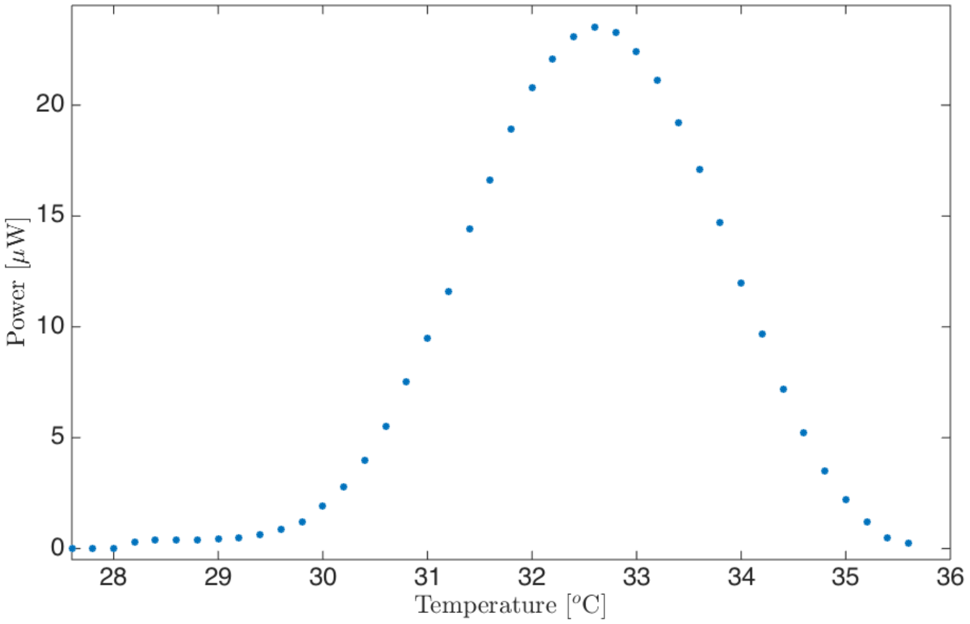

Figure 41: Phase matching in SHG crystal. The blue dots show the data measured. The temperature of the copper heatsink was varied slowly while monitoring the second harmonic output. A maximum output was found at T = 32.6°C.

crystal length, L, and the twice Rayleigh length of the beam. A parameter ξ is introduced [16]:

$$\xi = \frac{L}{b} = \frac{L}{2z_0}. \tag{6.1}$$

If the beam is propagating straight through the crystal the optimal ξ value is 2.84. The optimum value for ξ varies with the angle at which the light propagates through the crystal. In practice it is easiest to assume straight propagation, perform beam shaping, and align to ensure maximum output. The ξ value used in this setup is 2.96 due to lack of lenses available.

The power conversion from the fundamental frequency to the second harmonic is given by (for a derivation, see. Appendix B):

$$P_{2\omega} = \gamma P_\omega^2. \tag{6.2}$$

In Fig. 42 the power conversion is measured and fitted. The data show beautiful compliance with the expected behaviour, with $\gamma = (2.344 \pm 0.002) \cdot 10^{-5}$ (mW)$^{-1}$.

After careful alignment, beam shaping and characterization of the phase matching condition, a maximum of 120 μW was created from roughly 80 mW infrared light reaching the crystal.

Given the power conversion parameter γ, and the crystal length of 15 mm, the relative conversion efficiency pr. power pr. length was found to be:

$$\epsilon_{SHG} = \frac{2.34410^{-2}\ (\mathrm{W})^{-1}}{1.5\ \mathrm{cm}} = 1.56\ \%(\mathrm{W\ cm})^{-1}. \tag{6.3}$$

This may not seem like much, but it is almost twice as high as the value of 0.8 % (W cm)$^{-1}$ reported in [17], indicating that the setup is working reasonably well. Though 120 μW was created, only about 60 μW reached the cavity, due to loss through the EOM.

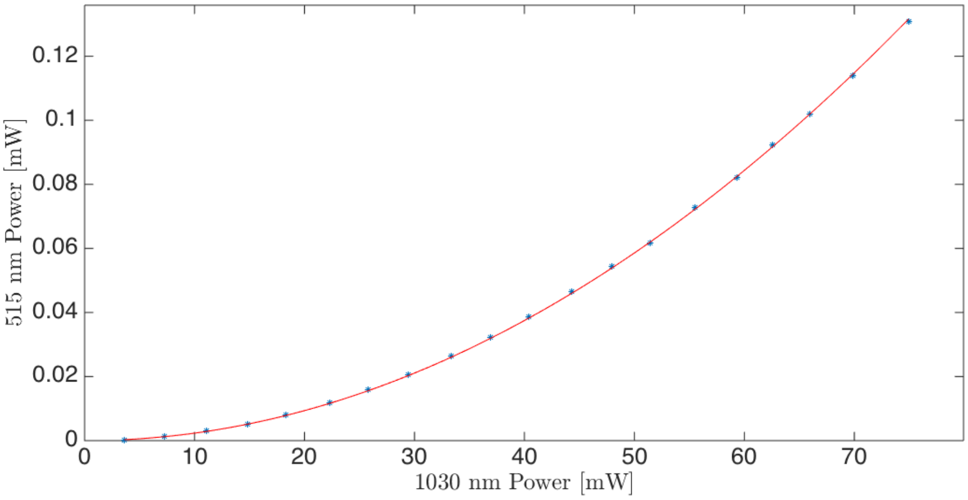

Figure 42: Second harmonic generated power as function of input power. The blue dots show the data measured, and the red curve show the fit. The data recorded shows almost perfect correspondence with the expected behaviour in eq. (6.2), with $\gamma = (2.344 \pm 0.002) \cdot 10^{-5}$ (mW)$^{-1}$. A maximum of 120 μW was created at roughly 80 mW 1030 nm input.

6.3 Sample Cell

The sample cell was purchased at Sacher Lasertechnick. Due to the intended experimental use, a series of requirements were made. The cell is made of fused silica to ensure a high optical quality, and the windows are Brewster cut in order to minimize losses. In order to control the internal pressure, a coldfinger was placed on the short side of the cell. The cell is 15 cm long, and has a diameter of 25 mm, as shown in Fig. 43.

The iodine vapor inside the cell was slighty purple at room temperature, and the solid iodine was at times also visible on the cell walls.

Initial measurements performed with the cell in the cavity showed adequate optical quality. The reflection at the Brewster windows was found to 0.83 %. But due to the molecular sample being contaminated, the cell had to be returned and refilled at the manufacturer, which resulted in a degradation in the optical quality, such that the final transmission of the Brewster windows more than doubled to 1.93 %. A slightly white, matte desposit is visible at various placed on the cell, which most likely stems from the cleaning process of the cell before the new sample was introduced see Fig. 45. For clarity, the contaminated sample is denoted Sample 1, and the refilled sample is denoted Sample 2.

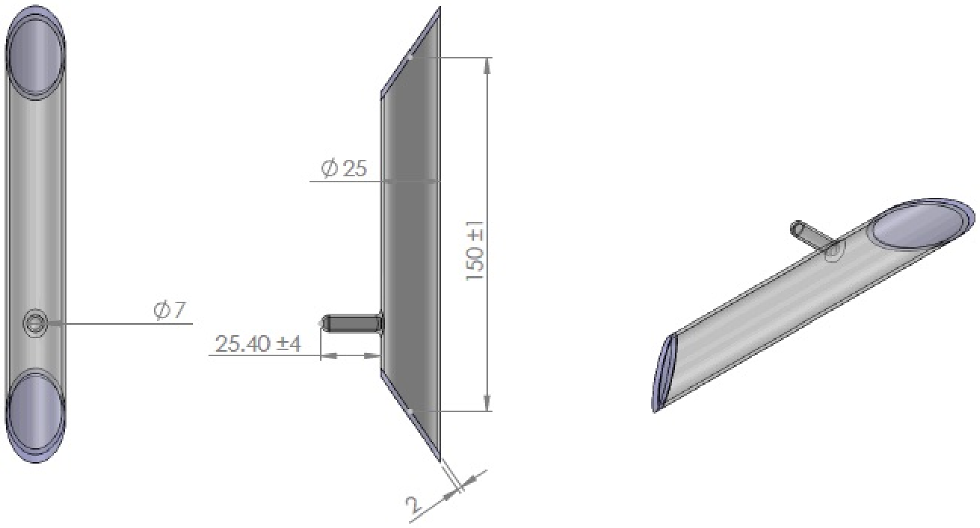

Figure 43: A schematic drawing of the sample cell supplied by the manufacturer. The coldfinger ended up being placed in the middle of the short side. The dimensions of the cell was designed to match the length of the interrogation cavity.

(a)

(b)

Figure 44: The iodine vapor cell. At room temperatur the slight purple vapor is visible to the naked eye. (a) show the cell from the side and (b) show the end facet of the cell. The small dark looking granulate visible in (b) is solid state iodine.

After the cell had been returned, a quick test was made by comparing the spectral properties of the new sample with an older 30 cm control cell available. The control cell did not have Brewster cut windows making it unfit for CEAS and NICE-OHMS. The control measurement was performed as a SAS setup, but due to the sample being held at room temperature, i.e., at very high pressure, all hyperfine lines are broadened. The measurement was performed using a 532 nm laser. The data recorded, with the background removed, is shown in Fig. 46. Both Sample 2 and the control cell showed the same broadened line profile. It was however not possible to determine at what wavelength the spectral line was at nor its linewidth, as the the laser did not have built-in wavelength tuning, and the only way to tune the laser was to vary the output power.

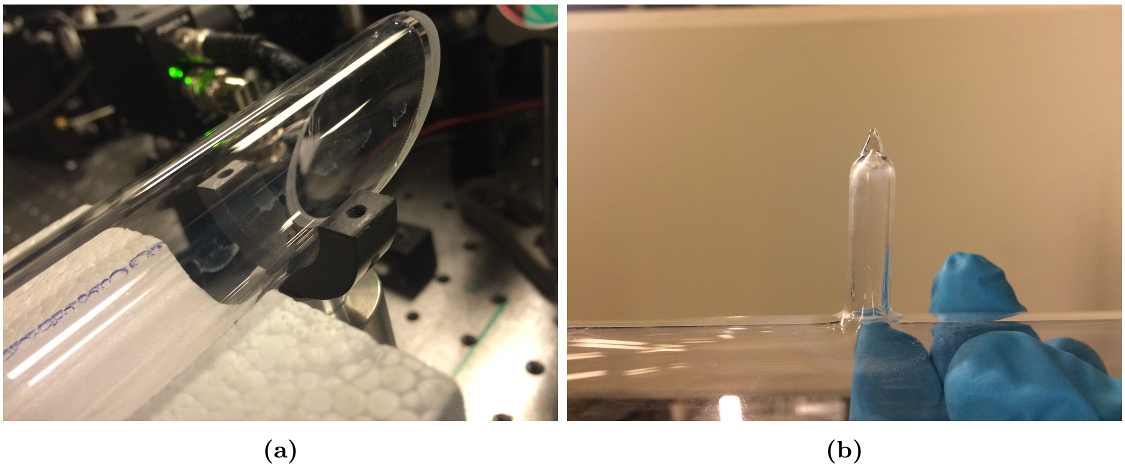

Figure 45: The iodine vapor cell after being returned for a refill. Matte, white deposits are visible of, e.g., the coldfinger and where the coldfinger is attatched, as well as on the cell walls. These were not present before the cell was re-filled. This indicates that the chemicals used to clean the cell after the contaminated sample was removed have left deposits, degrading the optical quality. The degradation in optical quality was evident in the measurements performed after the re-filling of the cell.

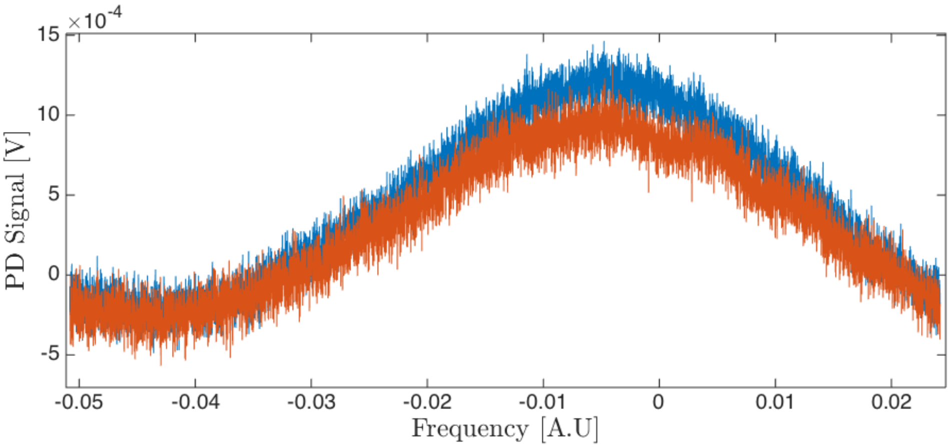

Figure 46: Measured SAS signal performed on Sample 2. The returned cell was compared spectrally against an older, 30 cm long, iodine vapor cell. The blue signal show the data obtained from the control cell, and the orange data the refilled sample cell. The two show the same spectral property, i.e., a broadened line profile is visible in both data sets. The background has been subtracted and only the peak arising from the sample is plotted.

6.4 Characterization of the Cavity-Cell system

As this experiment, to the author's knowledge, has been the first of its kind performed on iodine, the characterization of the cavity-cell system is crucial in order to set the foundation for successful results as well as future improvements. As mentioned in Sec. 6.3, the molecular sample had to be replaced during the course of the work done in this thesis. Therefore, two separate characterizations were made - one for the initial sample, denoted Sample 1, and one for the sample placed inside the cell after the refill, denoted Sample 2. All NICE-OHMS measurements were carried out on Sample 1.

Absorption measurements for both Sample 1 and Sample 2 were performed prior to introducing the cell into the cavity in order to determine the pressure dependent molecular absorption, see Sec. 5.4.

The empty itself was made up of two mirrors with a ROC of -9 m, separated by roughly 30 cm. This yields a waist of 0.43 mm.

6.4.1 Finesse

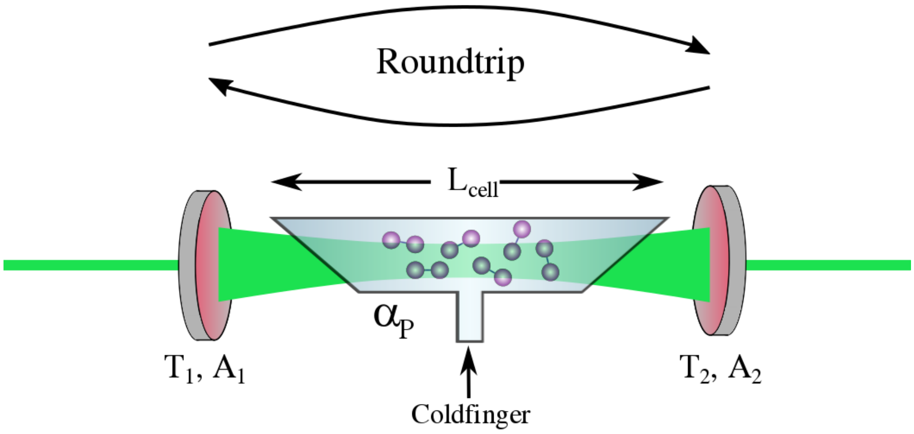

Figure 47: The roundtrip loss arising from the sample cell being introduced into the cavity. The mirrors both have a loss associated with the transmission, denoted T_1 and T_2. The loss at the Brewster windows and the additional loss from the mirrors, such as absorption and scattering, have been collected in a common notation, A_1 and A_2. The sample itself has a pressure dependent absorption, i.e., a pressure dependent loss, denoted α_P. The vapor pressure P varies with the coldfinger temperature.

As introduced in Sec. 3.1.1, the finesse of the cavity-cell system plays an important role as the finesse serves to enhance the interrogation length. When a cell with a weakly absorbing sample is introduced in the cavity, the finesse of the whole system varies greatly with internal cell pressure, i.e., the molecule density, due to the absorption changing with pressure. The finesse of the cavity depends on the roundtrip loss, and using eq. (3.18), we recall:

$$F = \frac{2\pi}{Loss} = \frac{\pi}{T + A}, \tag{6.4}$$

which for the empty cavity case gives a finesse of 630, where A is assumed to be neglible compared to the mirror transmission T of 0.5%. The finesse of the empty cavity was measured, and showed great correspondence with the expected value. The coupling efficiency was measured to be $\approx$ 55%. The relatively poor incoupling was due to lack of lenses avaliable when the set-up was build which compromised the mode matching.

Additional losses in the cavity is introduced by the cell. The extra loss arises from the absorption from the molecules as well as loss at the brewster windows, the finesse is expressed as:

$$F(\mathrm{T}) = \frac{2\pi}{T1 + T2 + A1 + A2 + (1 - e^{-\alpha_{\mathrm{P}}\mathrm{P(T)}2\mathrm{L}_{\mathrm{cell}}})}, \tag{6.5}$$

where we can assume that $T1 = T2$, i.e., the transmission at each mirror is the same, and that $A1 = A2$ holds the loss at both Brewster windows as well as the mirrors. P(T) is the coldfinger temperature-dependent vapor pressure, and $\mathrm{L_{cell}}$ is the cell length. α_P is the pressure dependent absorption measured in Sec. 5.4 and is given in units of (m Pa)$^{-1}$. This model was tested experimentally by measuring the finesse at different coldfinger temperatures. The finesse was experimentally measured by adding 25 MHz sidebands to the interrogating light in order to determine the FWHM of the cavity mode. The FSR of the cavity was determined to be 500 MHz. By using eq. (3.17) the finesse was determined:

$$F = \frac{FSR}{FWHM}. \tag{6.6}$$

The measurements were carried out at temperatures varying from -45.1°C to -15.6°C corresponding to a vapor pressure of 0.02 Pa to 0.73 Pa in Sample 1, and -40.1 °C to -19.8 °C corresponding to a vapor pressure of 0.03 Pa to 0.45 Pa in Sample 2. The interrogating light was kept on resonance with the molecules during all measurements to ensure maximum absorption. The finesse is plotted along with the expected behaviour in Fig. 48 and 49.

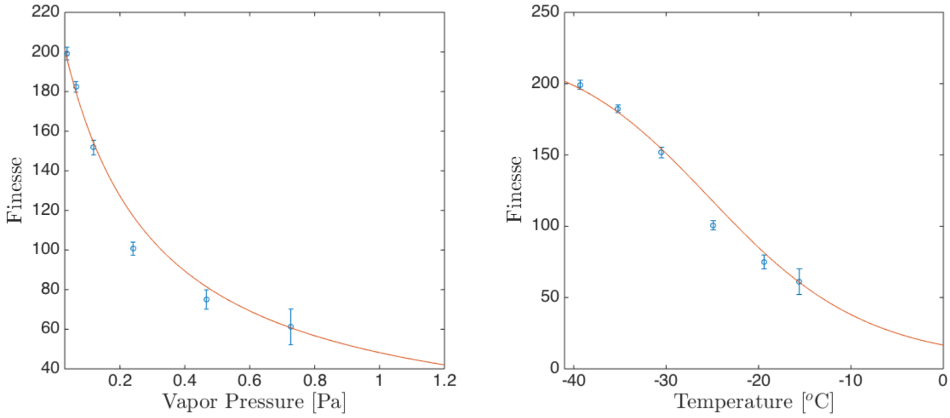

Figure 48: Sample 1. A direct measurement of the cavity-cell system finesse plotted as function of the vapor pressure (left) and temperature of the coldfinger (right). The blue points show the data recorded, while the orange curve show the expected behaviour based on eq. (6.5). The data recorded does follow the expected behaviour nicely. In order to obtain the best fit possible, the only variable varied was the loss at the Brewster windows, A, which is the only truly unknown parameter, as the mirror transmission was determined by measureing the empty cavity finesse, and the molecular absorption was measured prior to introducing the cell into the cavity. Parameters used to describe the finesse are $\mathrm{T_1 = T_2 = 0.5}$ %, $\alpha_\mathrm{P} = 0.35$ [1/(m Pa)], and $\mathrm{A_1 = A_2 = 0.83\%}$. Discreprancy between the absoprtion coefficient used in this model and the one measured may be due to the fact that the absorption coefficient measured is based on too few samples, as the temperature control was limited when initial measurements were performed

Overall, the data obtained follows the general slope of the expected behaviour. The measurement performed on Sample 1 shows a better compliance with eq. (6.5) than the data obtained from Sample 2. The loss at the Brewster windows was determined to be 1.93% for Sample 2, compared to 0.83% for Sample 1. The loss at the cell windows for Sample 2 is unusually high, since at the right polarization, losses as low as 0.01-0.03% are achievable [18]. As discussed in Sec. 6.3, the degrading in optical quality is expected to

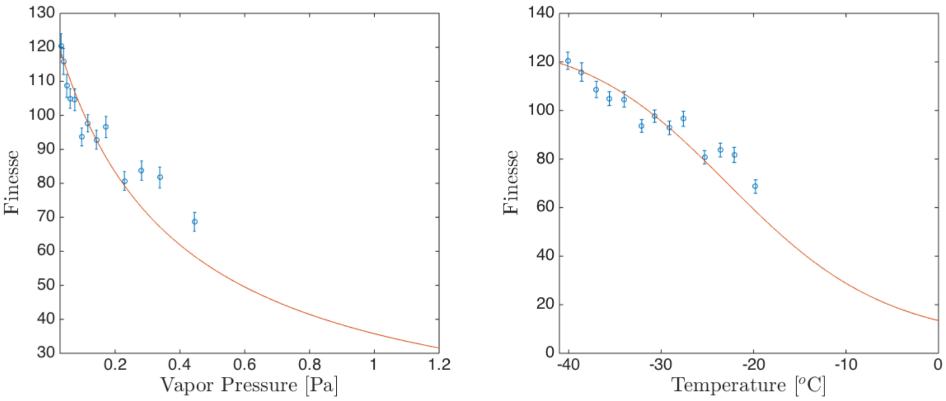

Figure 49: Sample 2. A direct measurement of the cavity-cell system finesse as function of the vapor pressire (left) and temperature of the coldfinger (right). The blue points show the data recorded, while the orange curve show the expected behaviour based on eq. (6.5). The finesse has been worsened compared to the data shown for the same measurements performed on Sample 1. This is partly due to the change in absorption, but also the degrading in the optical quality of the cell, as discussed in Sec. 6.3. The parameters used to describe the finesse are $T_1 = T_2 = 0.5$ %, $\alpha_P = 0.45$ [1/(m Pa)], and $A_1 = A_2 = 1.93\%$.

stem from the replacing of the molecular sample.

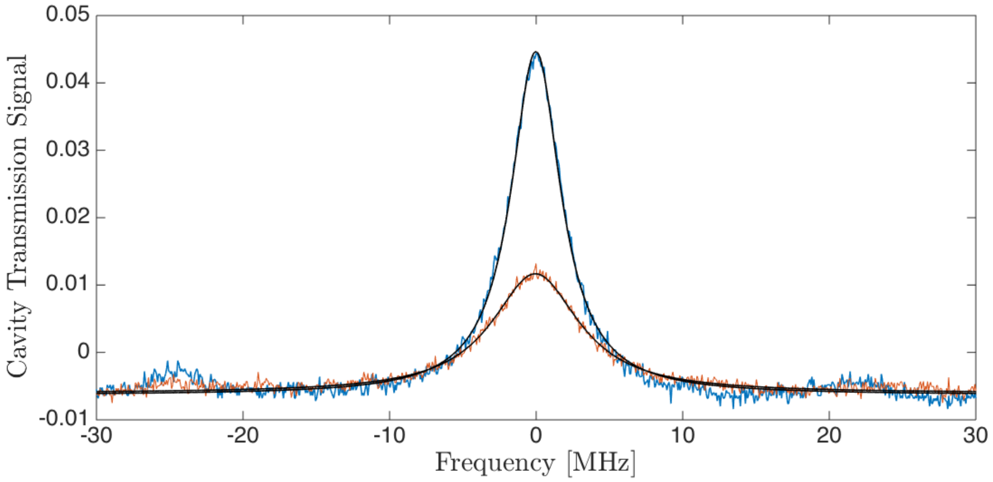

Figure 50: The signal transmitted by the cavity at T = -40.1 °C (blue curve) and T= -19.8 °C (orange curve). The data obtained stem from Sample 2, but the behaviour is similar to that observed in Sample 1. As the temperature increase, the signal is increasingly dominated by external noise, as less power reach the PD, making measurements performed at temperatures higher than $T = -15^o$C unreliable. The black curves on top of each dataset show the fit made in order to determine the FWHM of the transmitted signal. The FWHM of each signal at varying pressure and tempeature is listed in table 5.

The absorption varies with pressure, setting an upper limit as to how high the coldfinger temperature can be while measureing the finesse. At high temperatures the signal transmitted by the cavity gets dimmer, making the PD signal inceasingly noise dominated. The difference in signal between the signal picked up at -40.1 °C and -19.8 °C is shown in Fig.

50. Beyond -15 °C the transmitted peak and the sidebands were barely distinguishable from the background noise.

The data collected on the FWHM of the transmitted signal with varying pressure for both Sample 1 and Sample 2 is listed in Table 4 and 5.

T [°C]	-45.3	-39.3	-35.2	-30.5	-24.9	-19.4	-15.6
P [Pa]	0.016	0.037	0.070	0.119	0.2402	0.466	0.726
FWHM [MHz]	2.32	2.45	2.74	3.30	4.97	6.67	8.17
σ_{FWHM}[MHz]	± 0.01	±0.02	±0.02	±0.04	± 0.08	± 0.21	± 0.56

Table 4: Sample 1: The linewidth of the cavity-cell system with varying temperature. As more and more absorbers are introduced into the cavity as the pressure increase, the wider the cavity mode becomes.

T [°C]	-40.1	-38.6	-37.0	-35.6	-34.0	-32.1	-30.7	-29.1	-27.6	-25.3	-23.6	-22.1	-19.8
P [Pa]	0.033	0.041	0.051	0.061	0.076	0.097	0.116	0.142	0.172	0.229	0.282	0.338	0.445
FWHM [MHz]	4.15	4.32	4.60	4.77	4.78	5.34	5.12	5.39	5.18	6.20	5.97	6.12	7.28
σ_{FWHM} [MHz]	± 0.03	±0.04	±0.04	±0.03	±0.05	±0.04	±0.04	±0.04	±0.04	±0.05	± 0.05	± 0.06	±0.07

Table 5: Sample 2: The linewidth of the cavity-cell system collected at different coldfinger temperature, i.e., at different vapor pressures. The linewidth is in general much wider than that obtained in Sample 1. This is partly due to the change in absorption, but also due to the decrease in optical quality of the sample cell.

Given the beam dimensions and the cavity-cell system finesse, the intra-cavity power and intensity is calculated using eq. (6.5) and (3.34). The mean intensity in the cavity is given by:

$$I_{cav} = \frac{P_c}{\pi w^2}\eta. \tag{6.7}$$

η is taking the coupling efficiency into the cavity into account. The waist of the beam is $w = 0.43$ mm. A plot showing the intra-cavity intensity- and power is shown in Fig. 52.

The Sample 1 system showed great promisse, as the finesse of the system is sufficient to ensure saturated absorption, as the recommended $\text{I}_{\text{sat}} < 40$ mW/cm^2 [3]. The finesse of the Sample 2 system struggles to reach a power build-up high enough, as the maximum intensity is ≈ 16 mW/cm^2 at T = -45 °C. The low intra-cavity intensity can be improved by either optimizing the coupling into the cavity, which is currently limited by poor impedance matching (see Sec. 7.2), or by simply generating more power. This is also discussed in Sec. 7.

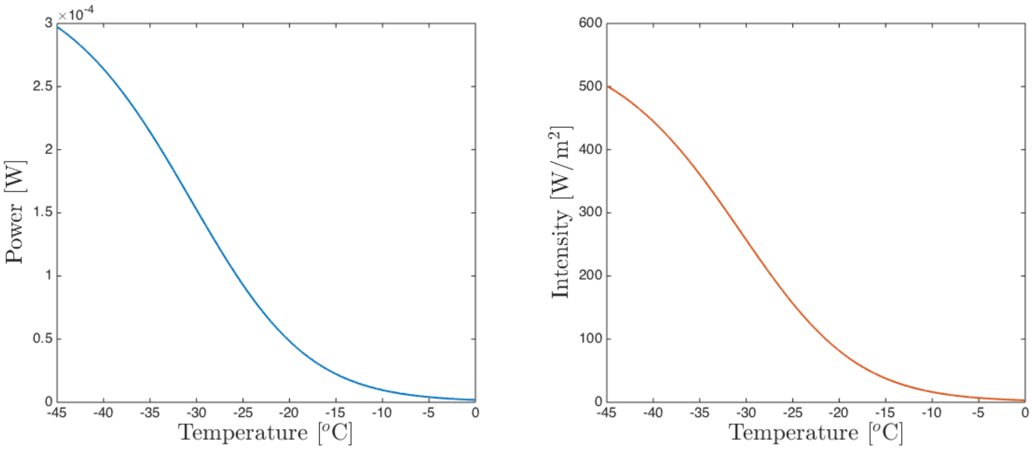

Figure 51: Sample 1: The intra-cavity power (left) and mean intensity (right) as function of the finesse, and thereby temperature. The intra-cavity intensity has been modeled using a $P_{\text{in}} = 60\ \mu\text{W}$. With a finesse of a maximum of 240, the intensity reaches a maximum of approximately $50\ \text{mW/cm}^2$, which should be more than sufficient for performing saturated spectroscopy, as the intensity recommended by BIPM yields $I_{\text{sat}} < 40\ \text{mW/cm}^2$.

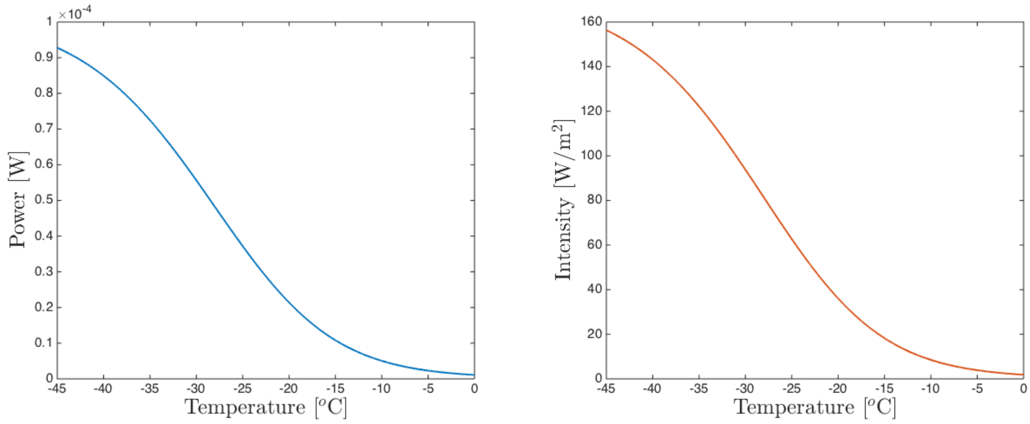

Figure 52: Sample 2: The intra-cavity power (left) and mean intensity (right) as function of the finesse, and thereby temperature. Again, the intensity has been modelled assuming the maximum $P_{\text{in}} = 60\ \mu\text{W}$ available. Despite the the cavity ensuring a field biuld up, the intensity of the beam struggles to reach a value high enough to generate a saturated absorption signal. This is due to a poor in-coupling and the degradation in the finesse of the system.

6.4.2 Vapor Pressure

In order to evaulate the internal vapor pressure in the cell, all data given on the subject in [1], [6] and [15] was collected and fitted according to the Antoine equation that relates the vapor pressure of pure components to the temperature:

$$\begin{aligned} \log(\mathrm{P(T)}) &= \mathrm{A} - \frac{\mathrm{B}}{\mathrm{C+T}} \\ \mathrm{P(T)} &= 10^{A-\frac{\mathrm{B}}{\mathrm{C+T}}}. \end{aligned} \tag{6.8}$$

T is the temperature in Kelvin and P is the pressure in Pa. A, B and C are constants. The data gathered from [1], [6] and [15] is shown in Table 6.

T [°C]	-22	-15	-15	-14.5	-13	-11	-5	-2.28	15
P [Pa]	0.37	0.79	0.83	0.87	1.0	1.29	2.38	3.3	18

Table 6: Temperature vs. Pressure [Pa] collected from [1], [6] and [15]. The data obtained was used in order to determine the connection between coldfinger temperature and vapor pressure.

The data was plotted and fitted using eq. (6.8), and yields the following relation:

$$\mathrm{P_{I_2}(T)} = 10^{14.01-\frac{4005}{\mathrm{T}-25.55}}. \tag{6.9}$$

The data and the fit are shown in Fig. 53. It has not been possible to measure the vapor pressure of the sample used in this work directly. This means that here may be some some discrepancy between what the acutal vapor pressure is, and what the model predicts.

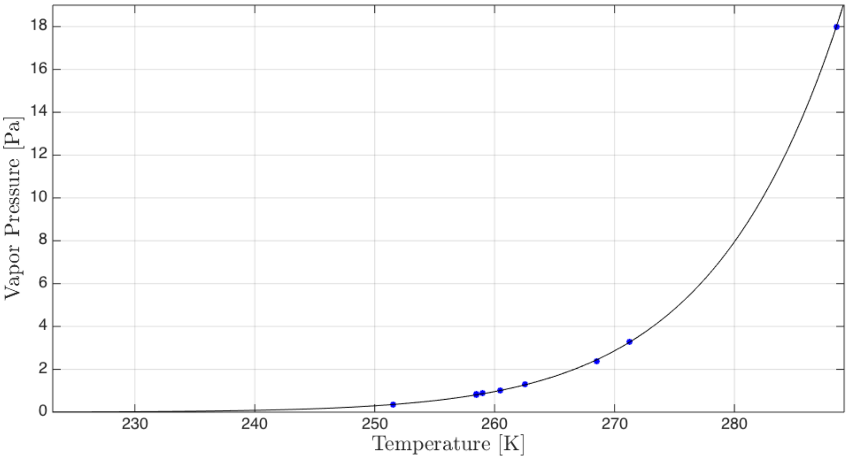

Figure 53: The vapor pressure of the sample inside the cell as function of coldfinger temperature. The blue dots are data points collected and the black curve is a fit corresponding to eq. (6.8).

6.4.3 Cavity Locking

The cavity was locked using the PDH locking scheme when CEAS and NICE-OHMS was performed. The PDH-scheme is described in Sec. 3.2. The cavity locking was inherently challenging as the size of the error signal would vary with frequency as the light was on and off resonance with the molecules. The generated error signal is shown in Fig. 54. Despite the error signal size changing while the experiment was carried out, the cavity lock was rather robust to disturbances such as loud noises or vibrations. The circuit used in the feedback loop is discussed in Sec. 6.9.

At high temperatures, i.e, at large vapor pressure, the error signal decreases in size. Therefore it was not possible to conduct experiments a temperatures much higher than T $\simeq$ -25 °C, as the error signal would have shrunken about 50% in amplitude compared to the signal size at T $\simeq$ -35 °C.

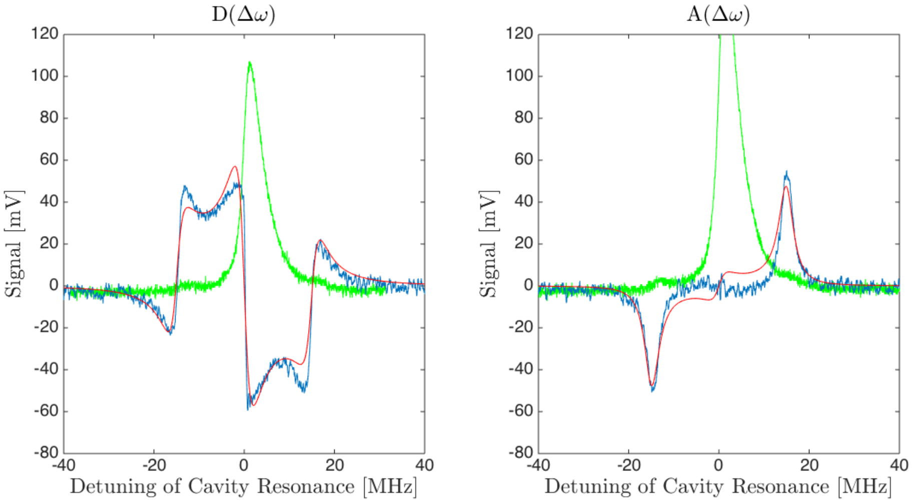

Figure 54: The error signal generated for locking the interrogation cavity while scanning the wavelength over the resonance. The green curve shows the transmitted signal from the cavity, and the blue curve shows the generated error signal. The D-component is shown in the left figure, and the A-component in the right figure. The red curve shown is the error signal as predicted by theory. It was particularly challenging to generate an error signal that could keep the cavity locked, when the amplitude of the error signal varied with the absorption in the sample. This meant that it would not be possible to perfom CEAS at temperatures much higher than -25°C, as the difference in signal size would vary too much over the course of one scan.

6.4.4 Number of Molecules

The number of molecules present in the interrogation beam is calculated using the Ideal Gas Law. Though iodine is not an ideal gas, the behaviour can be assumed to mimic that of an ideal gas at low vapor pressure, where inter-molecular interactions can be assumed neglible. The number of molecules is thus given by:

$$N = \frac{PV}{kT}, \tag{6.10}$$

where P is the pressure, V is the cell volume, k is Boltzmanns constant and T is the temperature of the gas in Kelvin. From this the density of the gas is calculated using: $n = N/V$:

$$n = \frac{P}{kT}. \tag{6.11}$$

The cell volume is approximated by a cylinder, giving a volume of 0.29 L. With a gas tempereature of 300 K, and the pressure varying from 0.01 Pa to 0.1 Pa, the density is:

$$n \approx 10^{19} \quad \text{molecules/m}^3. \tag{6.12}$$

For a beam with waist size of 0.43 mm propagating through a cell of length 15 cm, and taking the enhancend interrogation length into account, the interaction volume is $\pi/4\text{L}_{\text{cell}}Fw_0^2$ = 2.83 $\times 10^{-6}$ m^3 where F is assumed to be 200. Using these numbers, the number of molecules in the interrogation beam is of the order of 10^{13}.

As the setup uses Doppler-free spectroscopy, the molecules contributing to the signal are only those whose velocity is zero in the direction of the interrogation beam, i.e., the z-

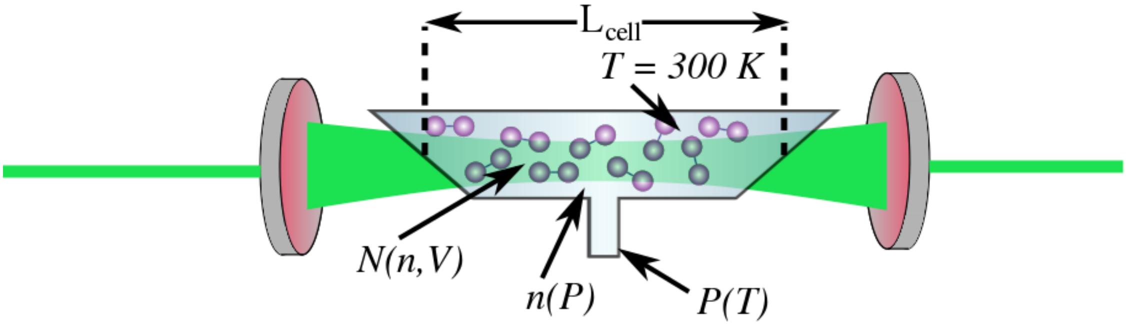

Figure 55: A schematic showing the physics governing the number of molecules in the sample. The internal vapor pressure $P(T)$ is controlled by the coldfinger temperature T. The vapor pressure dictates the molecular density in the cell $n(P)$, which determines the number of molecules $N(n, V)$ in the interrogation volume V, which is determined by the beam profile and the cell length, $\mathrm{L}_{\mathrm{cell}}$. The temperature of the gas itself is 300 K.

direction. From eq. (2.14) we get:

$$\begin{aligned}\int_{-\infty}^{\infty}\int_{-\infty}^{\infty}\int_{-\Gamma/k}^{\Gamma/k} f(v)dv_x d_y dv_z = \pi^2\sqrt{\frac{M}{\pi 2k_BT}}\int_{-\Gamma/k}^{\Gamma/k}\exp\left(\frac{-Mv_z^2}{2k_BT}\right)dv_z \\ \approx 0.7\times 10^{-3},\end{aligned} \tag{6.13}$$

where Γ is the linewidth of the transition of the a_3 component, and k is the k-vector magnitude of the light. This leaves on the order of 10^{10} molecules. Out of these, only a fraction of the molecules will be in the desired state. This was derived in Sec. 5.2, eq. (5.14). Only about 0.25% of the molecules would be in the desired state. Using this, we arrive at the final number of molecules contributing to the signal,

$$\begin{aligned}&\frac{N_{int}}{N_0} = 0.0025 \\ &N_{int} = 0.0025\times 10^{10} = 2.5\times 10^{7}\text{ molecules.}\end{aligned} \tag{6.14}$$

This is roughly a factor of 10^2 higher than what would be obtained in a similar sample without a cavity.

6.5 Broadening Effects

The work done during this thesis relies on CEAS and NICE-OHMS. The three main limiting broadening effects are evaluated in the following.

6.5.1 Pressure Broadening

As previously introduced, the pressure broadening of a sample arise from molecules colliding, and is also known as collisional broadening. The line profile of a pressure broadened transition is Lorentzian [23]. In [1], the pressure dependent linewidth of the a_3 is measured. The data is summarized in Table 7.

Pressure Broadening of the P(13)13-0a_3 Transition

P [Pa]	0.518	0.742	1.234	1.661	2.674	3.122
Γ (HWHM) [kHz]	192.7	214.0	258.2	301.2	350.7	379.0

Table 7: Data on the pressure dependent broadening of the a_3 component of the P(13)43-0 transition. Data from [1].

The relation between pressure and linewidth of the a_3 component is fitted with a second order polynomium [1]:

$$\Gamma(\mathrm{P}) = \Gamma_0 + a\mathrm{P} + b\mathrm{P}^2, \tag{6.15}$$

where P is the pressure and a and b are constants determined by the fit. Γ_0 is the natural linewidth of the transition. The resulting fit and data is shown in Fig. 56.

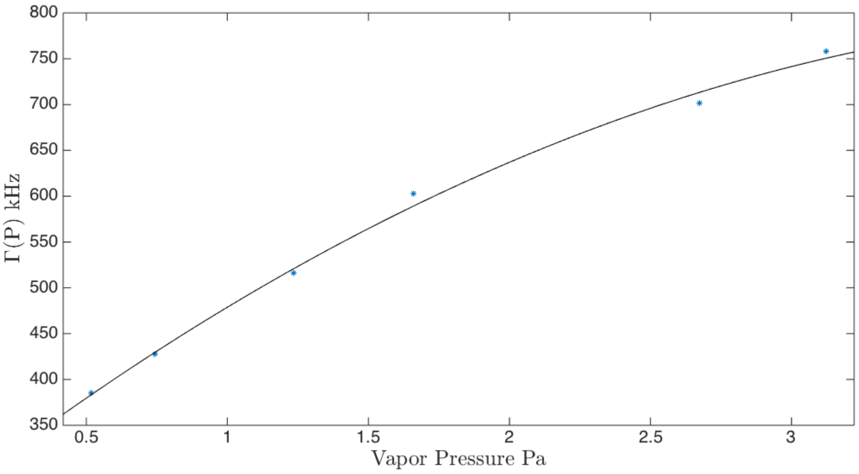

Figure 56: The pressure broadening af the a_3 component of the P(13)43-0 transition. The blue points show the data from [1], and the black curve show the fit obtained using a second order polynomial as in [1]. a and b was found to be 238.7 ± 25.8 kHz/Pa and -26.9 ± 7.0 kHz/Pa^2, respectively

The vapor pressure used in the work done in thesis is much lower than 1 Pa and thus the P^2 term is assumed neglible. The effective pressure broadening can then be expressed as:

$$\Gamma(\mathrm{P}) = \Gamma_0 + a\mathrm{P}. \tag{6.16}$$

From the fit in Fig. 56, a is determined to be 238.7 ± 25.8 kHz/Pa. The pressure used in the experiments perfomed in this thesis varies from 0.015 Pa to 0.12 Pa, the pressure broadening of the a_3 component vary from 2.8 kHz to 28.4 kHz. This is much lower than the pressure broadening in [1], where the pressure used in the experiments was 3.30 Pa.

As mentioned in Sec. 5.2, a very interesting candidate for a future frequency refrence is the a_2 component, whose linewidth is just 48 kHz (FHWM), in comparison the the 240 kHz (FWHM) linewidth of the a_3 component. There is no concrete data given on the pressure broadening of the a_2 component in [1], but data on the matter has been collected for various other transitions, with a pressure broadening similar to the results obtained from the a_3 component. It is fair to assume that the pressure broadening of the narrower

a_2 component will be similar to that of the a_3 component. At least within the same order of magnitude.

6.5.2 Transit Time Broadening

The transit time broadening is a limiting factor in the current setup. The transit time broadening is introduced in Sec. 3.3.2:

$$\delta\nu_{TT} = \frac{\sqrt{2\ln(2)}}{\pi}\frac{v}{w}, \tag{6.17}$$

where v is the velocity, and w is the beam waist. In the experiment performed in this thesis, the sample consists of thermal molecules, and the velocity can not be adjusted. Therefore, the transit time broadening is the limiting factor due to the narrow waist.

The most probable speed of the molecules is given by [23] :

$$v = \sqrt{\frac{2}{3}}\sqrt{\frac{3RT}{M_m}}, \tag{6.18}$$

where R is the molar gas constant, T is the temperature in Kelvin, and M_m is the molar mass of the molecule. For iodine at $T = 300$ K, this gives a velocity of 198 m/s. For a beam waist of 0.43 mm, this gives a transit time broadening of:

$$\delta\nu_{TT} = 170.8 \text{ kHz}. \tag{6.19}$$

If the beam expander cavity is employed, the transit time broadening will be reduced to 21.2 kHz, i.e., the transit time broadening will be reduced by a factor of 8.

6.5.3 Power Broadening

The power broadening in the system is given by:

$$\Gamma_s = \Gamma_0\sqrt{1+S_0}, \tag{6.20}$$

where Γ_0 is the natural linewidth, and the saturation parameter S_0 is given by:

$$S_0 = \frac{I}{I_{sat}}. \tag{6.21}$$

BIPM has recommended a saturation intensity of $I_{sat} < 40$ mW/cm^2. The intensities used in the experiment performed varied from 28 mW/cm^2 to 10 mW/cm^2 resulting the power broadened linewidth of the a_3 component to vary between 313 kHz to 268 kHz, respectively.

In Table 8 the broadening effects discussed in this section are summarized.

Broadening Effects of the a_3 component	
Pressure Broadening	2.8 - 28.4 kHz
Transit Time Broadening	170.8 kHz
Power Broadened Linewidth	268 - 313 kHz

Table 8: Overview of the Broadening Effects present in the system. The dominating broadening effect is the transit time broadening.

6.6 NICE-OHMS Results

A series of NICE-OHMS and CEAS measurements were carried out in a set-up as the one shown in Fig. 35. The measurements are amongst the first of its kind carried out in this kind of set-up, and at such low vapor pressure while still being compact.

The experiment was carried out before the cell was found to be contaminated, and thus the cavity finesse and intra-cavtity power- and intensity is equal to those of Sample 1. The measurements were carried out at T ∼-30 °C, corresponding to a pressure of 0.1 Pa. The interrogation length is enhanced by a $(2/\pi)F$ due to the cavity. With a finesse of $\simeq$ 200 at T = -30 °C, this results in an effective interaction length of 20 m.

As BIPM recommends an interrogation beam intensity that is lower than 40 mW/cm^2 to avoid saturation broadening, the interrogation beam intensity was kept at a maximum 28 mW/cm^2. This should be sufficient for saturated spectroscopy, as lower interrogation beam intensities have been reported in [6].

Once the cavity was locked, scanning of the NICE-OHMS- and CEAS signal was possible. The results are shown in Fig. 57. The three figures show the NICE-OHMS signal obtained at different intra-cavity powers, and all three figures show the average of 64 consecutive measurements.

The top figure show the a NICE-OHMS scan and CEAS signal performed with an intra-cavity power of 28 mW/cm^2. The middle figure shows the NICE-OHMS scan at 17 mW/cm^2, and finally the bottom figure show the NICE-OHMS scan at 10 mW/cm^2.

Very dissappointingly it was not possible to observe any hyperfine transitions in the data using Sample 1. In order to determine the cause of the corruption of the signal both the interrogating laser and the sample was examined.

The sample cell was taken to the Danish Fundamental Metrology Institute, where spectroscopy was performed simultaneously on Sample 1 and a control cell. The measurement unambiguously determined that the sample was contaminated.

The NKT Koheras AdjustiK laser was taken back to the manufacturer for inspection. The frequency output was measured, and found to have rapid fluctuations. The fluctuations were also measured in our own lab, and showed drift of approximately 20 MHz over the course of one second. The cause of the frequency drift is expected to stem from some kind of flaw in the laser current supply. The manufacturer has not been able to identify the cause of this issue.

In order to circumvent these issues, the cell was returned to the manufacturer for a refilling (Sample 2), while a stabilizing setup was built for the interrogation laser. This is discussed in the following section.

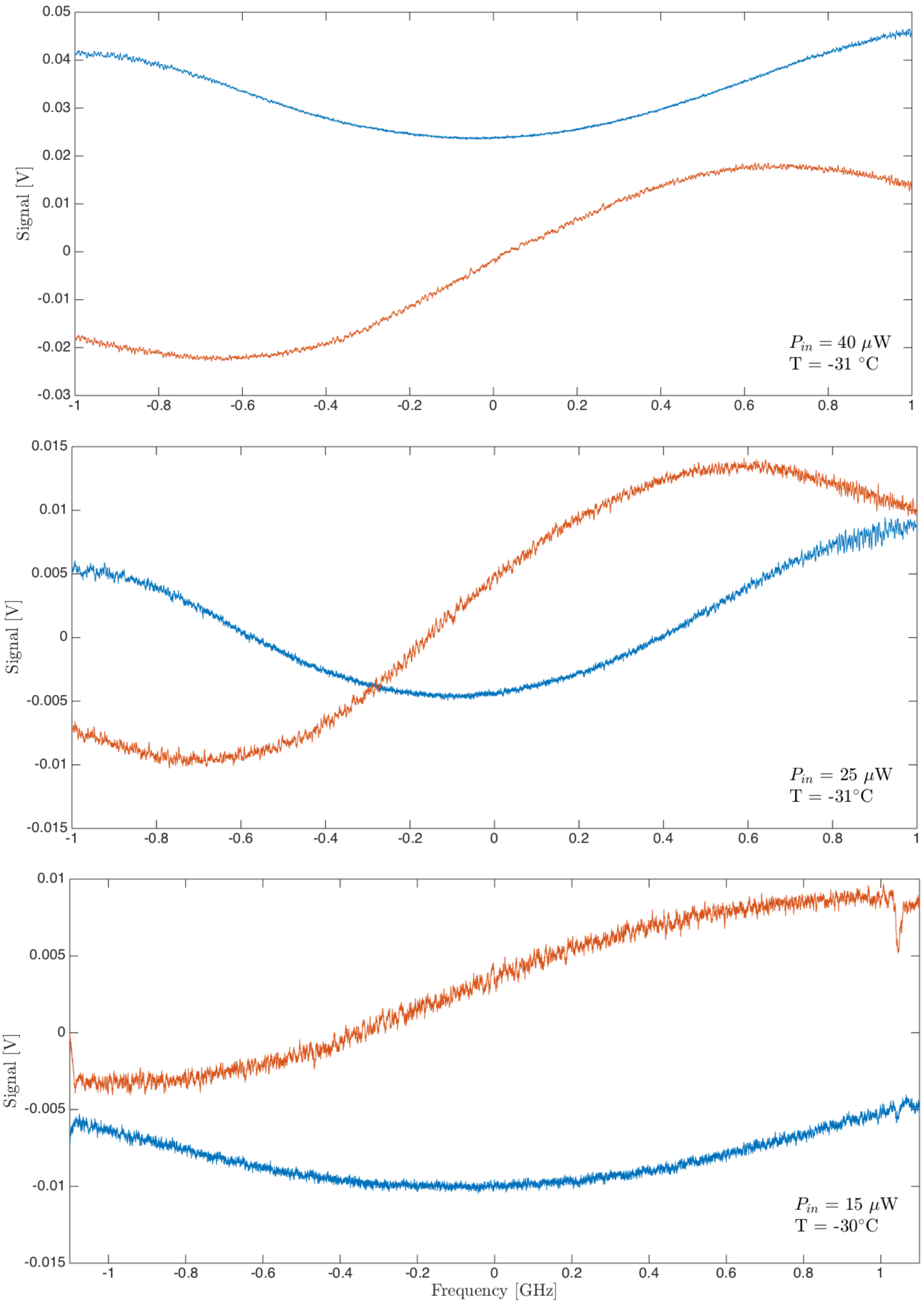

Figure 57: Data obtained from NICE-OHMS and CEAS scans performed on iodine (Sample 1), using various interrogation laser power. The blue curves shows the saturated absorption signal, and the orange curve shows the NICE-OHMS signal. The data plotted is the average of 64 consecutive measurements. The data obtained are in stark contrast to those expected, Fig. 25. The lack of any hyperfine transitions was later determined to be due the impureness of the molecular sample, and the instability of the laser.

Despite the lack of any hyperfine transitions we do observe that the NICE-OHMS signal amplitude decrease with the field power as expected. The signal amplitude detected at $P_{in} = 40\ \mu$W is roughly thee times larger than that detected at $P_{in} = 15\ \mu$W, which is reasonable since the ratio between the two input powers is roughly 1:3. The offset in the measured saturated absorption signal is due to dimming of light reaching the PD. The zero-crossing of the NICE-OHMS signal is also different for each measurement contrary to theory. This most likely stem from the demodulation, i.e., the mixing, between the signal detected by the PD and the modulation frequency from the function generator. The power depence suggest that there may be some phase delay induced by the PD when the power incidint on the detector is varied.

Besides being held back by an impure sample and a very unstable laser, the NICE-OHMS signal can be improved further. As introduced in eq. (4.15), the amplitude of the signal is partially determined by the modulation index δ:

$$i_{PDmod} \approx 4E_0^2 J_0(\delta) J_1(\delta) \phi. \tag{6.22}$$

The modulation index can be determined using [25]:

$$\delta = \pi \frac{V_m}{V_\pi}, \tag{6.23}$$

where V_π is the half-wave-voltage and is $\approx$ 110V for the EOM used. V_m is defined through the applied voltage:

$$V = V_m \sin(\omega t). \tag{6.24}$$

The modulation signal was amplified using a Mini Circuits ZHL-2-8 amplifier with a maximum output of 29 dBm, which is equivalent to 6.40V. This gives a maximum $\delta = 0.18$. In Fig. 58, the product of the zero- and first order Bessel function along with the value given by the current modulation index. The current δ gives $J_0(\delta)J_1(\delta) = 0.09$, as compared to the maximum at $\delta = 1.1$, where $J_0(\delta)J_1(\delta) = 0.34$, i.e., a factor of 4 in NICE-OHMS signal amplitude can be won by amplifying V_m further. One way to ensure amplification of V_m is to employ a resonance circuit that effictively amplifies the modulation signal. A proposal for such a circuit is presented in Sec. 7.4.

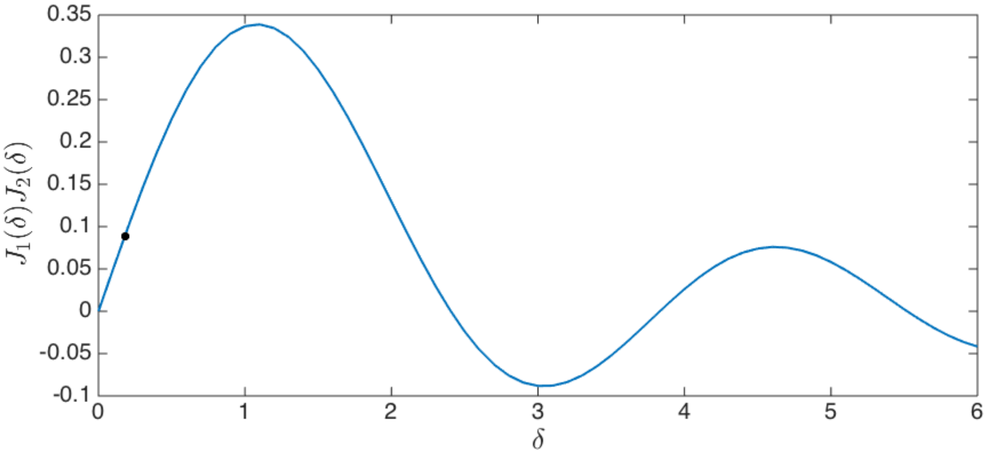

Figure 58: Schematics of the NICE-OHMS technique.

6.7 Frequency Stabilization of NKT Koheras AdjustiK

In order to decrease the frequency drift of the NKT Koheras AdustiK laser, a high finesse stabilizing cavity was build in order to stabilize the laser.

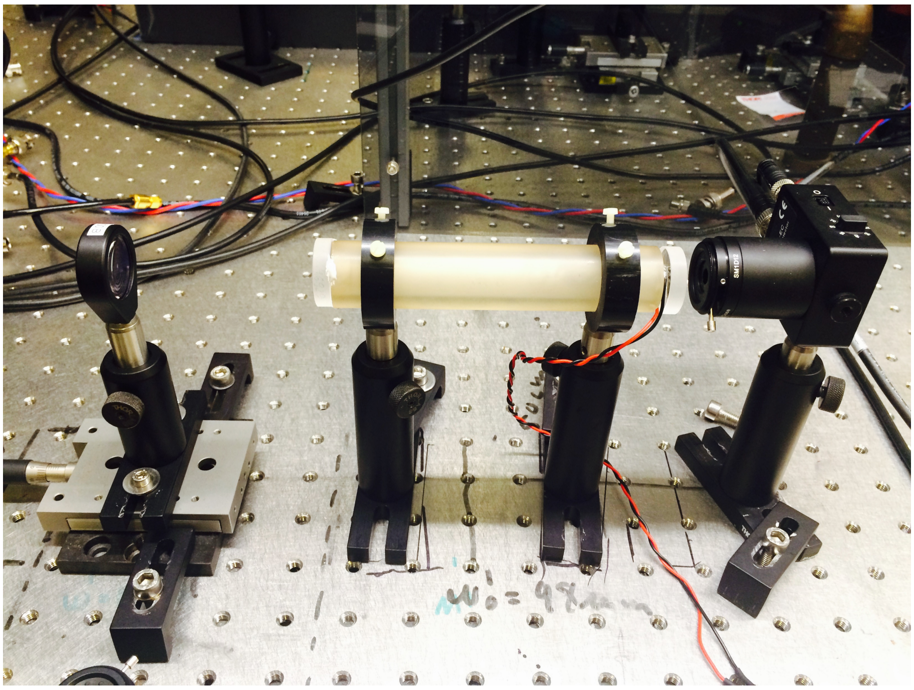

Figure 59: The stabilization cavity consisting of two mirrors glued to a 12.2 cm long hollow zerodur glass rod. As the cavity length determines what frequency is being supported, the end mirror is glued to a piezo in order subsequently scan the IR laser once is has been locked to the cavity. The glass rod works to eliminate any other variations in cavity length, i.e., any instability arising from thermal expansions of the cavity.

The stabilizing cavity consits of two ROC = -75 mm mirrors separated by a 12.2 cm long hollow zerodur glass rod to suppress unwanted fluctuations in cavity length, Fig. 59. Before glueing the mirrors onto the glass rod, a great deal of work went into aligning the cavity properly. The mirrors were designed to have a reflectance of 99.5% yielding a finesse of 1250, but the measured finesse of the un-glued cavity was almost four times as high, 4300, giving a linewidth of ∼280 kHz, see Fig. 60. The light coupled into the cavity was not visible to the naked eye. Therefore, to perform initial rough alignment, a CCD camera was placed at the cavity output monitoring the intesity profile of the field inside the cavity. The intensity profile yields an almost perfect Gaussian intensity, as shown in Fig. 60a.

After rough alignment had been performed, a PD was set to monitor the cavity output. The cavity was scanned by varying the the wavelength coupled into the cavity. The final signal showed almost all power coupled into the fundamental TEM_{00} mode, see Fig. 61.

After the cavity had been aligned the zerodur glass rod was placed inbetween the mirrors and carefully attached to the out-coupling mirror. The cavity output was monitored while the glue was hardening. When the first mirror was attached to the glass rod, the second mirror was glued in the same manor. The glued cavity showed little sensitivity to

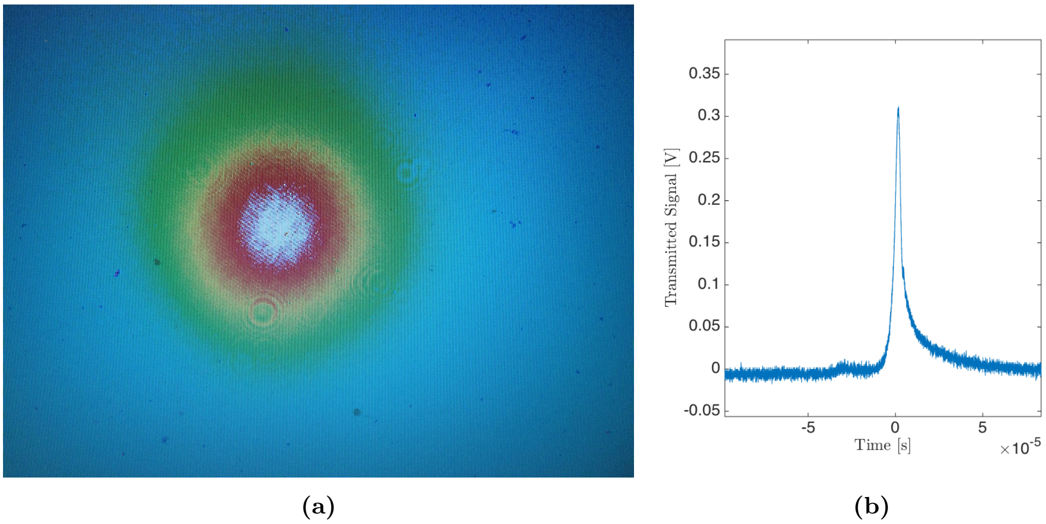

(a) **(b)**

Figure 60: (a) The measured intensity profile of the stabilization cavity. (b) Zoom-in on one of the transmitted peaks. The asymmetry of the peak is due to the performance capability of the photodiode used. The cavity linewidth was measured to be ∼ 280 kHz using 2 MHz sidebands before glueing. The narrow linewidth of the transmitted peak yielded a finesse impressive 4300.

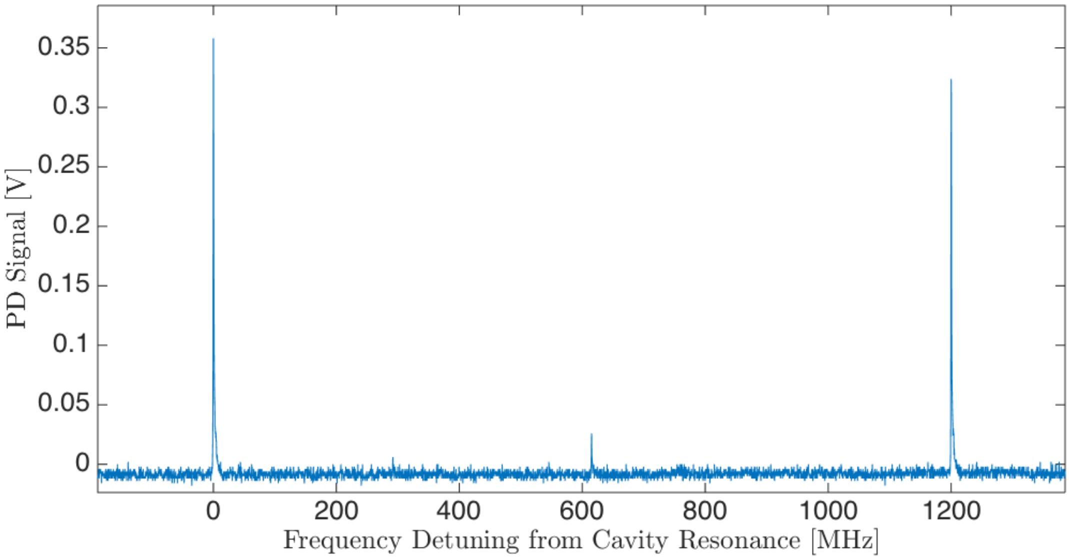

Figure 61: Transmitted power of the stabilizing cavity while scanning the laser frequency. The blue curve shows the transmitted power. The FSR was determined by measuring the length of the cavity.

mechanical disturbances such as vibrations, but in order to make the system as stable as possible, the cavity was placed on a breadboard that was isolated using sorborthane, and the whole cavity was then placed inside black box to further ensure thermal and noise isolation.

After the cavity was glued, the finesse was measured while scanning the length of the cavity, and determined to be of the order of 2200 with a linewidth of the order of 500 kHz. The degradation in finesse is expected to be due to a small angle in the mounting of the piezo electric element on the gass rod, making it not perfectly straight. Fumes from the glue may also have degraded the mirror reflectance slightly. The finesse is however still sufficient for laser stabilization. The cavity transmission as well as the generated PDH signal is shown in Fig. 62.

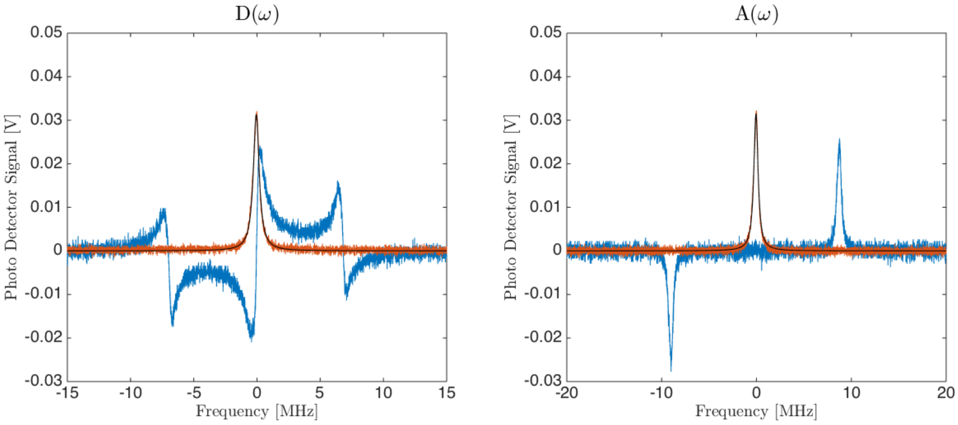

Figure 62: The A- and D-component of the PDH signal obtained from the stabilization cavity. The D-component was present at $\omega_m = 7$ MHz, and the A-component at $\omega_m = 9.23$ MHz. The blue curve shows the PDH signal, and the orange the transmitted field. A fit was made to the transmitted signal in order to determine the width of the cavity mode, which yielded ≈ 500 kHz. The cavity transmission signal has been scaled down by a factor of 10 in this plot.

The error signal was generated in order to both lock and and determine the stability of the laser-cavity system. This was done by fitting the slope of the D-component of the PDH signal in order to define a Voltage-to-MHz conversion factor.

The data shown in Fig. 63 was obtained using a different modulation frequency and a better photodetector than that shown in Fig. 62. Notice the great compliance between the data obtained and theory, along with the Signal-to-Noise Ratio (SNR) of 116. The Voltage-per-MHz conversion factor was determined to be:

$$\mathrm{Voltage-per-MHz : 0.1525V/MHz.} \tag{6.25}$$

The stability was measured by keeping the laser locked to the cavity over varying periods of time and monitoring the cavity transmission output. The voltage picked up by the PD was converted into MHz in order to determine the width of the locked system. The Allan variation in terms of fractional instability given by [12]:

$$\sigma = \frac{1}{\nu}\left(\sum_{i=1}^{N}\frac{\langle(\Delta\nu_i - \Delta\nu_{i-1})^2\rangle}{2(N-1)}\right)^{1/2}, \tag{6.26}$$

where ν is the frequency of the light, N is the number of samples. The fractional instabilty as function of the sampling time τ is plotted in Fig. 64.

The fractional instability of the laser locked to the cavity is of the order of $10^{-11} - 10^{-12}$, making it sufficient for stabilizing the laser frequency drift. In practice the width of the system is reduced from 20 MHz to ~ 300 Hz.

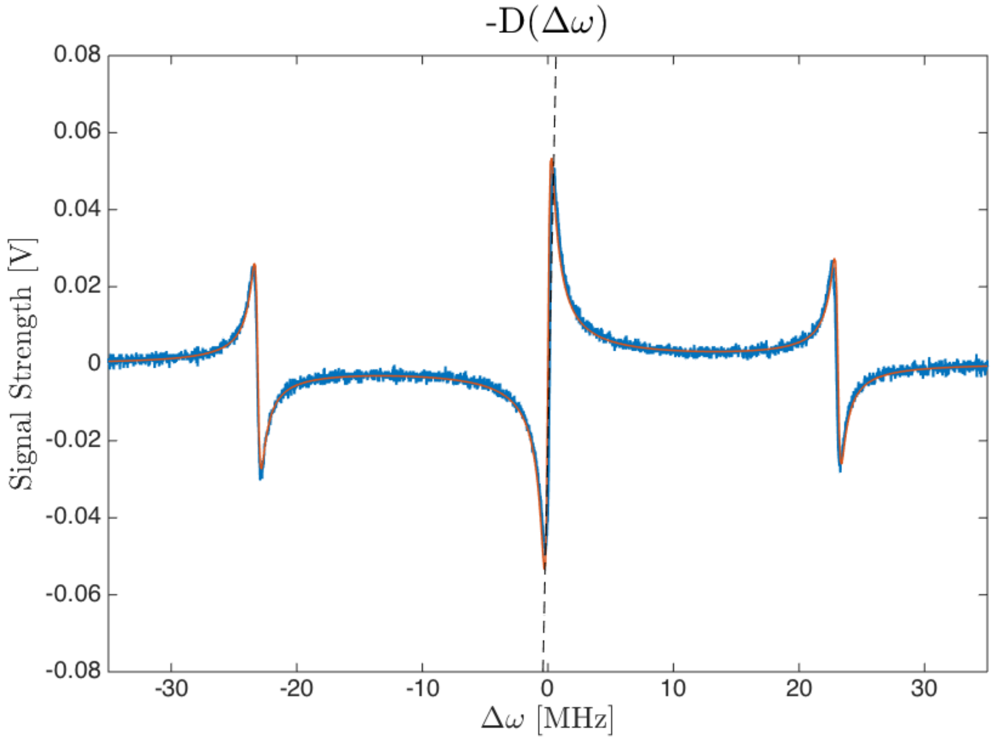

Figure 63: The D-component of the generated PDH signal. The blue curve is the measured signal, and the orange is the theoretical model. The modulation frequency used is $\omega_m = 23.1$ MHz. Notice the beautiful compliance with the theoretical curve. The signal-to-noise ratio of the error signal is an impressive 116.

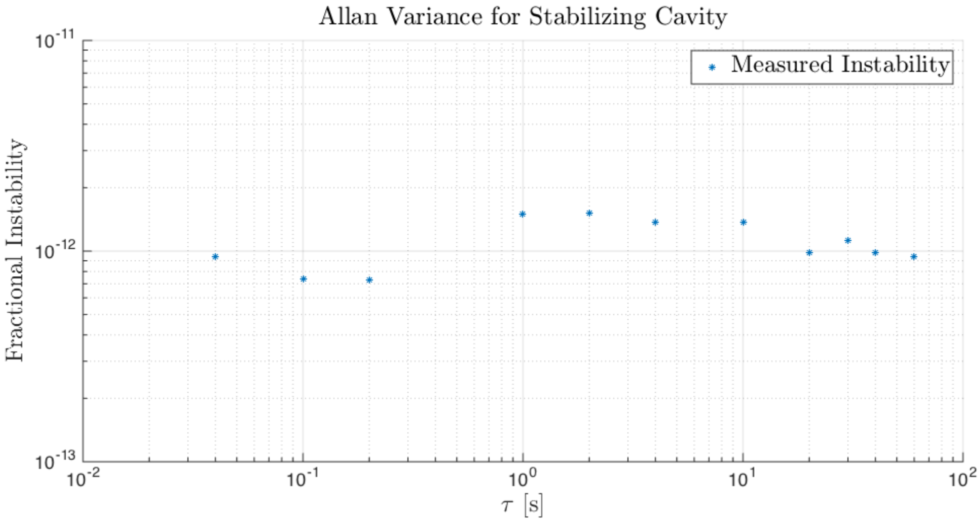

Figure 64: Allan variation of the IR stabilizin cavity. The Allan deviation was measured over time periods varying from 0.04 s to 60 s. The stability of the whole system start to decrease at $\tau > 1$ s, though it is still of the order of 10^{-11} for longer sample times.

6.8 Current Setup Status

Due to time limitations, it was not possible to redo the NICE-OHMS measurements during the course of this thesis. The current setup status is shown in Fig. 65.

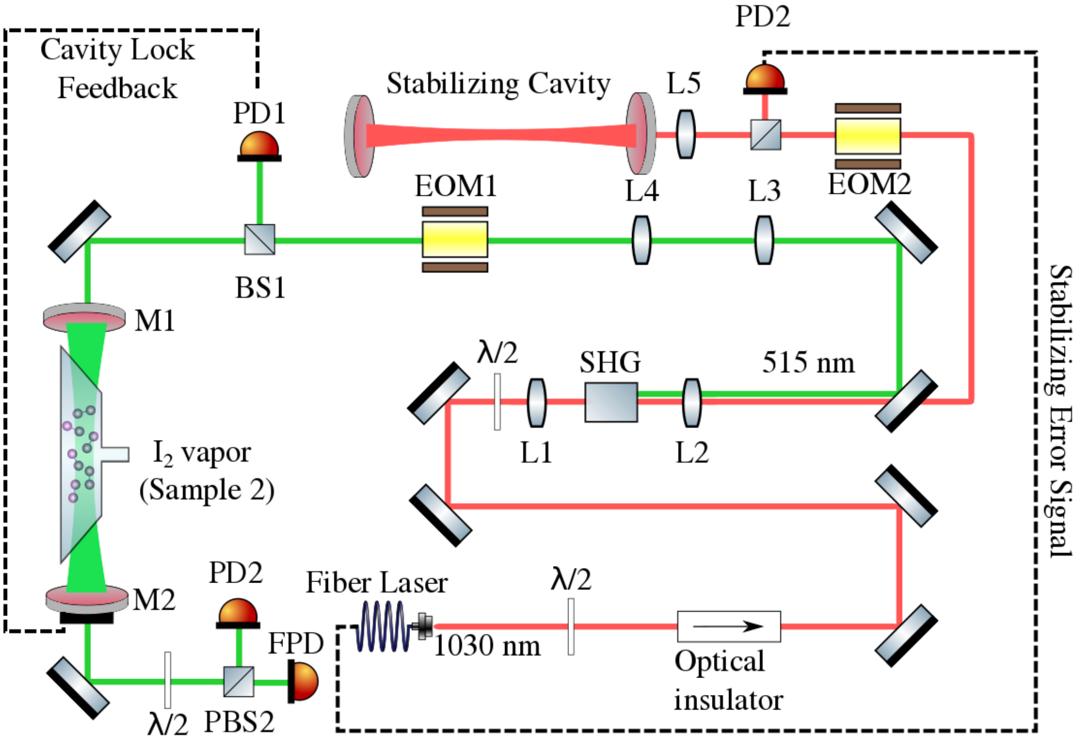

Figure 65: Stabilized NICE-OHMS setup. The interrogation laser has been stabilized using the cavity described in Sec. 6.7. The laser is locked to the cavity using the PDH scheme, and the laser wavelength can be tuned by varying the length of the stabilizing cavity through the piezo. The interrogation scheme is the same as presented in Fig. 35.

The current set-up has been improved compared to the setup shown in Fig. 35. The stabilization of the NKT laser combined with the new, presumably pure, iodine cell constitute the foundation for a succesfull experiment. There are however still issues to be solved. Due to the degrading in finesse, the intra-cavity power struggles to reach a high enough saturation power, which may compromise the signal. Therefore, another future improvement would be to supply more power. This is discussed in Sec. 7.3.

Furthermore, the future employment of the beam expander cavity introduced in Sec. 3.4 will enable even further reduction in vapor pressure, as well as reducing the current system limitation - the transit time broadening. This is also discussed in Sec. 7.1.

6.9 Cavity Lock Circuits

Both the interrogation and stabilization cavity was locked using similar locking circuits. The circuits can, when combined with the piezo, be related to Fig. 13 in Sec. 3.2, where the locking circuits and piezo electric element can be interpreted as the actuator. The error signal is fed into the locking circuit, where it undergoes, e.g., frequency dependent amplification in amplitude before it is fed back to the piezo, which in turns act on the system.

The two circuits in play, i.e., the one used to lock the interrogation cavity, and the one used to lock the stabilizing cavity, are identical in design, but due to the different nature of the two cavities, i.e., the stabilizing cavity delivering a much higher and narrower error signal than the one obtained from the interrogation cavity, the circuits have different component values.

Furthermore, it is worth noticing the slight difference in the way the locking circuits are employed. The interrogation cavity is locked in order to follow the change in wavelength when the molecular resonance is scanned. Therefore the cavity length is changed while scanning the sample.

In the case of the stabilizing cavity, it is the infrared light that is locked to the stabilizing cavity. The frequency of the light is controlled using the built-in piezo in the NKT Koheras laser. Thus, in order to be able to scan the frequency of the infrared light, the length of the stabilizing cavity is changed. This meant that the lock had to be able to follow the change in cavity length, in order to keep the laser locked to the cavity.

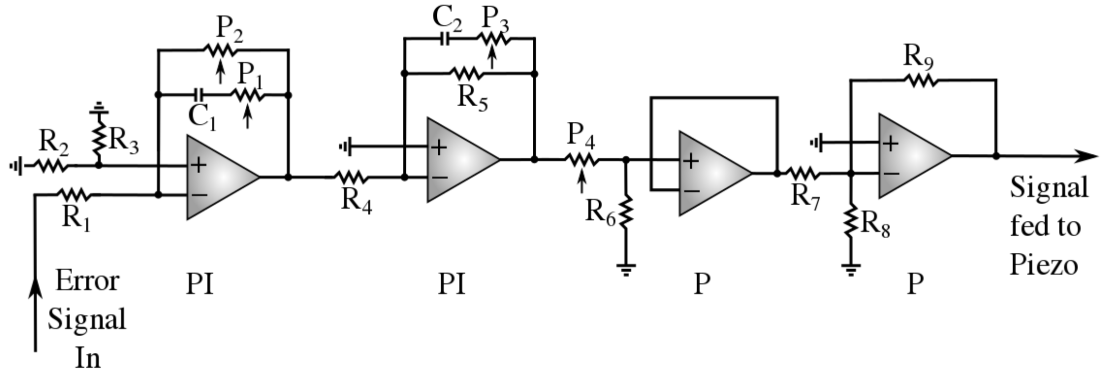

Figure 66: Schematics of the circuit design used to lock both the interrogation cavity and the stabilizing cavity. As the locking circuits share the same layout, but differ in component values, the values used in each circuit is listed in Table 9. The R denote resistors, P potentionemeters and C capacitors. The resistance of the potentiometers were optimzed each time the locking circuits were employed, meaning that the values used for $P_{1,2,3,4}$ would vary.

	R_1	R_2	R_3	R_4	R_5	R_6	R_7	R_8	P_1	P_2	P_3	P_4	C_1	C_2
I. C.	1.5 kΩ	1.5 kΩ	33 kΩ	100 kΩ	150 Ω	150 Ω	150 Ω	150 Ω	0-150 kΩ	0-50 kΩ	0-20 kΩ	0-20 kΩ	10 nF	10 nF
S. C.	1.5 kΩ	1.5 kΩ	33 kΩ	10 kΩ	1.5 kΩ	150 Ω	1.5 kΩ	1.5 kΩ	0-1 MΩ	0-50 kΩ	0-20 kΩ	0-20 kΩ	10 nF	10 nF

Table 9: Component values of the various components used in the two cavity locking circuits. I.C. is the interrogation cavity, and S. C. is the stabilizing cavity. The potentiometer resistance was optimized each time locking was necessary, thus making the resistor values vary each time. A simulation of the Bode plot for the interrogation cavity is show in Fig. 67.

Both circuits are designed as PI-PI-P-P (PI = Proportional Integrater, P = Proportional), which is also denoted in Fig. 66. The circuit is fed the error signal, which is then being amplified and integrated at the first operational amplifier (Op-Amp). An Op-Amp is a DC-coupled high-gain electronic voltage amplifier with a differential input and a single-ended output. The corner frequency and the amplification can be controlled using the two first potentiometers, P_1 and P_2. The second PI allows for further adjustment of the corner frequency, and is used to remove signal noise but the gain is fixed. The first P has an adjustable gain through the third potentiometer P_3. The last P is a simple voltage follower.

In practice, all potentiometer values in the circuit would be adjusted when locking the cavity. The signal from the error signal and the cavity output would be monitored simultaneously. If the corner frequencies were not chosen correctly, large, rapid oscillations were visible in the cavity output due to the piezo ringing. Therefore, the corner frequencies were adjusted when locking. The amplitude of the signal was also adjusted using P_2 and P_4. If the signal amplitude got amplified too high, the system would saturate and the lock would no longer be efficient.

Due to the optimization of the locking circuit every time the lock was employed, no concrete Bode plot was measured. But, based on some of the values noted from the potentiometer settings, a Bode plot for the lock used for the interrogation cavity has been simulated using the online simulation tool provided by www.systemvision.com. The results are summarized in Fig. 67.

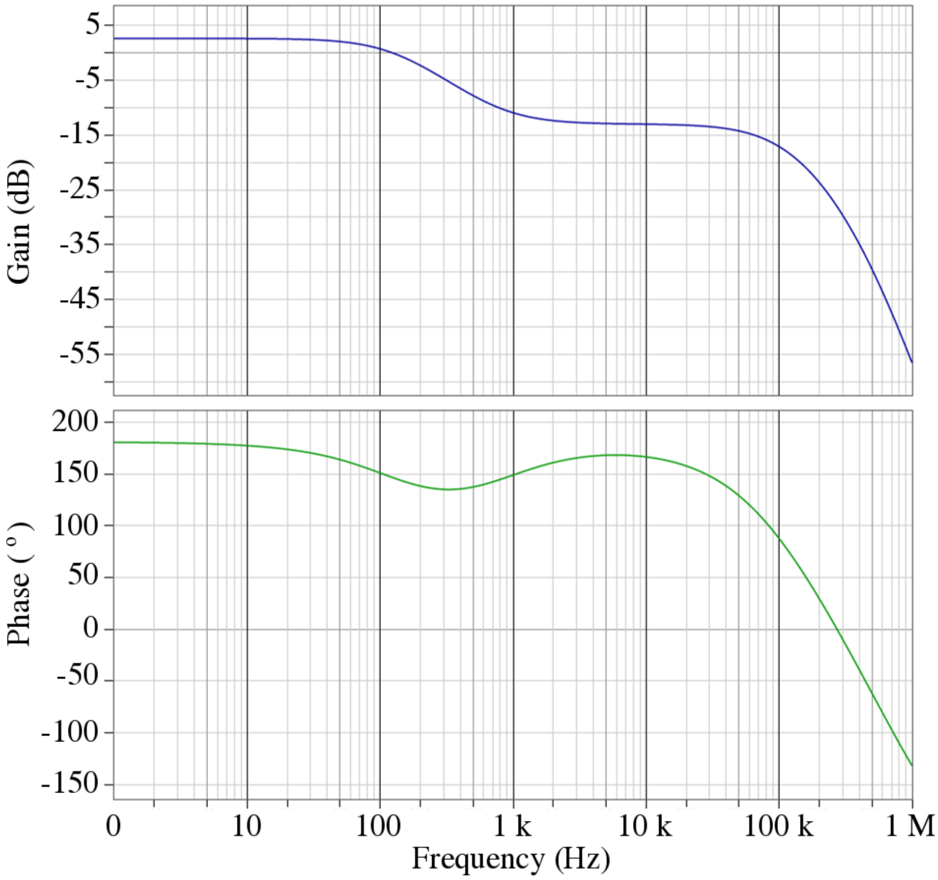

Figure 67: A simulated Bode plot using potentiometer values measured after the cavity had been locked. The potentiometer at P_1 was determined to be 120 kΩ, P_2 = 15 kΩ, P_3 = 20 kΩ and P_4 = 0.5 kΩ. The plot shown is that simulated at the output, i.e., the signal fed to the piezo in Fig. 66. The magnitude of the signal starts to fall off at approximately 80 Hz. This is the 3 dB point.

7 Future Prospects

As the work done in this thesis has been dedicated to building a working thermal molecular clock, a great deal of work has gone into characterizing and troubleshooting. The future of the experiments thus has room for improvements, some of which will be evaluated in this section.

7.1 Implementing the Beam Expander Cavity

One of the most evident future improvements to be introduced is the implementation of the beam expander cavity. The current limitation in the system stems from the transit time broadening, which is due to the narrow waist as explained in Sec. 6.5.

If the beam expander cavity is introduced, the number of interrogated molecules will be increased. It is fair to assume that the molecule density will be approximately the same, i.e., $n \approx 10^{19}$ molecules/m^3. If the waist size is increased to 3.5 mm, the interaction volume, i.e., the volume of the beam overlapping with the molecules, will be $\pi/4(2F/\pi)\mathrm{L}_{\mathrm{cell}}w_0^2 = 1.84 \times 10^{-4}$ m^3 compared to 2.84×10^{-6} m^3 in the current setup. Thus, the total number of moleculs contributing to the signal is enhanced by and a factor of 10^2.

The increase in waist size also serves to decrease the transit time broadening. The thermal velocity of the molecules is 198 m/s at room temperature. This gives a transit time broadening of:

$$\delta\nu = \frac{\sqrt{2\ln 2}}{\pi}\frac{v}{w} = 21.2 \text{ kHz}, \tag{7.1}$$

compared to the current 170 kHz.

The implementation of the beam expander cavity is currently held back by the low power available. When the beam waist increased, the intensity is lowered. Therefore more power is needed. Besides increasing the power of the light coupled in, the intra-cavity power build up can be optimized through impedance mathcing of the cavity. Both will be discussed in the following section. Impedance matching is also a limiting factor in the current setup.

7.2 Cavity Impedance Matching

In order to get the most efficient power build up in the cavity, one may assume that a higher finesse will result in the most efficient power build up, and while this is true for an identical two-mirror configuration as the one shown in Fig. 11, the assumption breaks down when more complex systems are introduced. In order to couple more light into the cavity the loss at the incoupling mirror must be impedance matched. Thus, the poor input coupling into to cavity-cell system described in section 6.4.1 may be improved by impedance matching of the incoupling mirror. In [22] a impedance mismatch parameter, σ, is introduced:

$$\sigma \simeq \frac{t_1^2}{L}, \tag{7.2}$$

where t_1^2 is the mirror transmission at the incoupling mirror and L is the total roundtrip loss excuding the loss at the input mirror. Note that t_1 is the transmission for the E-field, and not the power, which is given by $t_1^2 = T_1$. Looking back at eq. (6.5) we see that the loss in the cavity must be:

$$L = T + 2A + (1 - e^{-\alpha P 2 L_{cell}}), \tag{7.3}$$

where A is the loss at the Brewster cut cell windows, T is the mirror transmission at the end mirror, α is the pressure dependent absorption, and L_{cell} is the length of the sample cell. The relationship between the power build-up in the cavity as function of the mismatch parameter σ is given by:

$$\frac{I_c}{I_{c,matched}} = \frac{4\sigma}{(\sigma+1)^2}. \tag{7.4}$$

From this relation it is evident that the maximum intra-cavity intensity is acheived when $\sigma = 1$. Applying this to eq. (7.2) we find for maximum intra-cavity intensity:

$$T_1 = \text{Loss}. \tag{7.5}$$

Assuming a temperature of -30 °C the total loss excluding the incoupling mirror is 0.748. In Fig. 68 the relationship given in eq. (7.4) is plotted. As expected we see that the maximum intensity build-up is at $T_{1,matched} = 0.074$ compared to the current $T_1 = 0.0052$. With the current setup, the black dot in Fig. 68, the intra-cavity intensity is only about 25% of what is acheivable. If the input mirror reflectance is lowered such that the loss is impedance matched, the finesse of the system would be:

$$\begin{aligned} F(\mathrm{T}_c) &= \frac{2\pi}{T_{1,matched} + T_2 + 2A - (1 - e^{-\alpha_{\mathrm{P}} \mathrm{P(T)} 2 \mathrm{L}_{\mathrm{cell}}})} \\ &= 42, \end{aligned} \tag{7.6}$$

compared to the current $F \approx 100$. The finesse will be worsened by a factor of ~ 2, but the intra-cavity power would increase by a roughly factor of 4. The interaction length is still enhanced, such that the pressure can still be lowered.The main limitation stem from the loss at the Brewster windows that was increased by a factor of two after the cell was refilled, as discussed in Fig. 6.3. If the finesse as well as the intra-cavity intensity is to be maximized, it might be reasonable to invest in a new sample cell, as the cell showed great optical quality before being refilled.

Impedance matching is no less important when the beam expander cavity is employed. The increased beam waist demands a higher power, if the intensity of the beam is to be high enough to saturate the sample. The same analysis is applied to the beam expander cavity, where the temperature of the coldfinger is assumed to be T = -30 °C. If the optical components all have a reflectivity of $1 - T = R = 99.99\%$, exept for the incoupling mirror, and the sample cell has the same optical properties as the one used now, we find:

$$\begin{aligned} T_1 &= 7T + 2A + e^{\alpha_{\mathrm{P}} \mathrm{P(T)} 2 \mathrm{L}_{\mathrm{cell}}} \\ &= 0.076. \end{aligned} \tag{7.7}$$

This gives a finesse of 41. The plot of the impedance matching for the beam expander cavity is shown in Fig. 69. Again, the same conclusion that the optical quality of the sample cell limits the system, is reached.

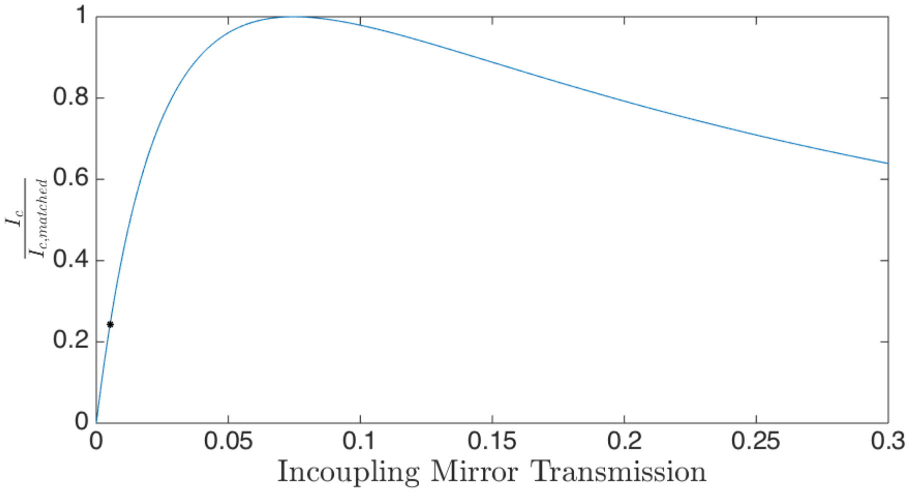

Figure 68: The impedance matching of the current cavity-cell system. Due to the high loss associated with the cell windows, the coupling of power into the cell is extremely inefficient. The black dot show the current impedance matching. If the system is impedance matched, the finesse of the system will decrease by roughly a factor of 2, while the incoupling is increased by a factor of 4

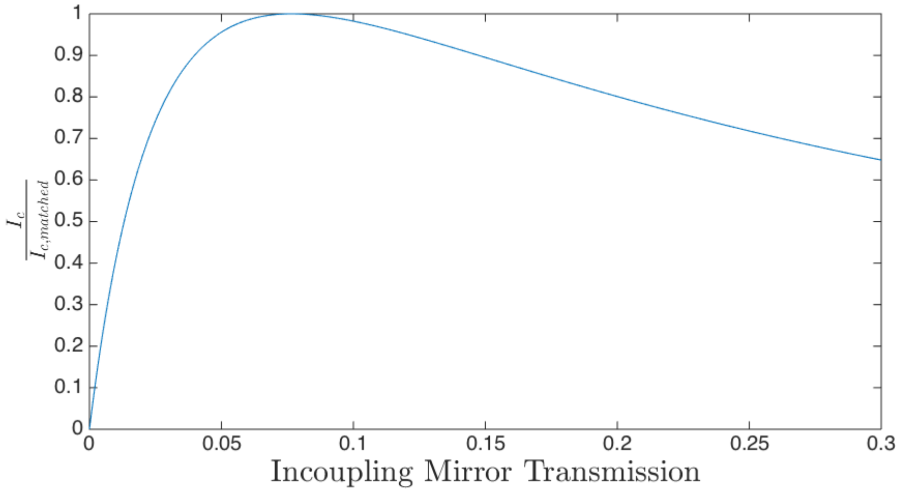

Figure 69: Impedance matching of the beam expander cavity. The analysis has been based on the assumption that the cell will have the same optical quality of the one currently used. The incoupling is most efficient at $T_1 = 0.076$, resulting in a finesse of just 41 at a coldfinger temperature of -30 °C.

7.3 Master Oscillator Power Amplifier - MOPA

What is evident from the analysis made in the previous section, is the fact that the current system is limited by the optical quality of the cell, which will result in a degradation in the finesse of the system, which in turn sets an upper limit for the power build up in the cavity. The current setup is limited by the power available from the NKT Koheras laser and the SHG crystal. Only about 60 μW reach the cavity, and roughly 10 % is coupled into the cavity due to poor impedance matching and limited mode matching of the cavity-cell system (see. Sec. 7.2).

For the purpose of keeping the setup simple, compact and single pass, a Master Oscillator Power Amplifier (MOPA) was chosen. A MOPA is a laser diode that amplifies an injected seed laser. Due to stimulated emission, the output from a seeded MOPA will have the narrow linewidth and the same wavelength. The gain medium itself is a tiny tapered amplying chip, abbrevated TA-Chip. The MOPA was purchased at Toptica, and according to the specifications, the MOPA should be able to deliver $\sim$ 1.5W when seeded with 40mW 1030nm light. An input of 1.5 W to the SHG crystal should generage roughly 13 mW light at 515 nm. The MOPA was placed in a large copper block to dissipate heat. The frontview of the MOPA is shown in Fig. 70.

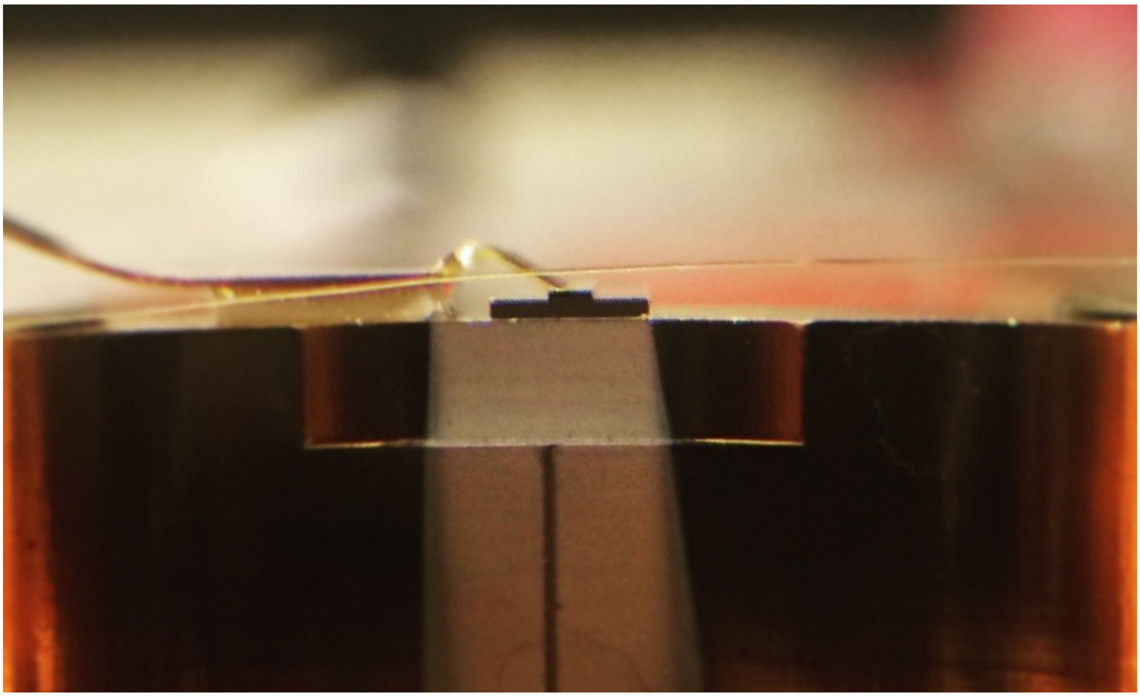

Figure 70: The MOPA shown with a hair of roughly 100μm for scaling. The tapered amplifier chip (TAC) sits inside the small black rectangle of approximately 100-150 μm attached to the gold wires. The TAC itself has an even smaller input aperture. The input aperture is roughly 1.4 μm $\times$ 3 μm and is therefor not visible to the naked eye. The output aperture is approximately 1.4 μ m $\times$ 250 μ m. The extremely small input aperture made the coupling of light into the amplifier extremely challenging.

The input aperture of the TA-Chip is of the order of $\sim$ 1.4 μm $\times$ 3 μm while the output aperture is of the order 1.4 μm $\times$ 250 μm. In order to effectively couple light into the TA-Chip, Toptica recommended using a 1:3 elliptical beam. The beam was shaped using a telescope consisting of two cylindrical lenses, giving a 0.57:1.61 beam, which should be adequate, see Fig. 71. In order to focus the beam to the right dimensions, a f = 6.24 mm lense was used in front of the input aperture MOPA.

Coupling light into the MOPA is inherently difficult due to the small input aperture of the TA-Chip. The human eye is capable of resolving around a 100 μm, making it impossible to rely on visual check when judging whether or not coupling has been achieved. The MOPA itself emits Amplified Spontaneous Emission (ASE) once a current is applied, making it

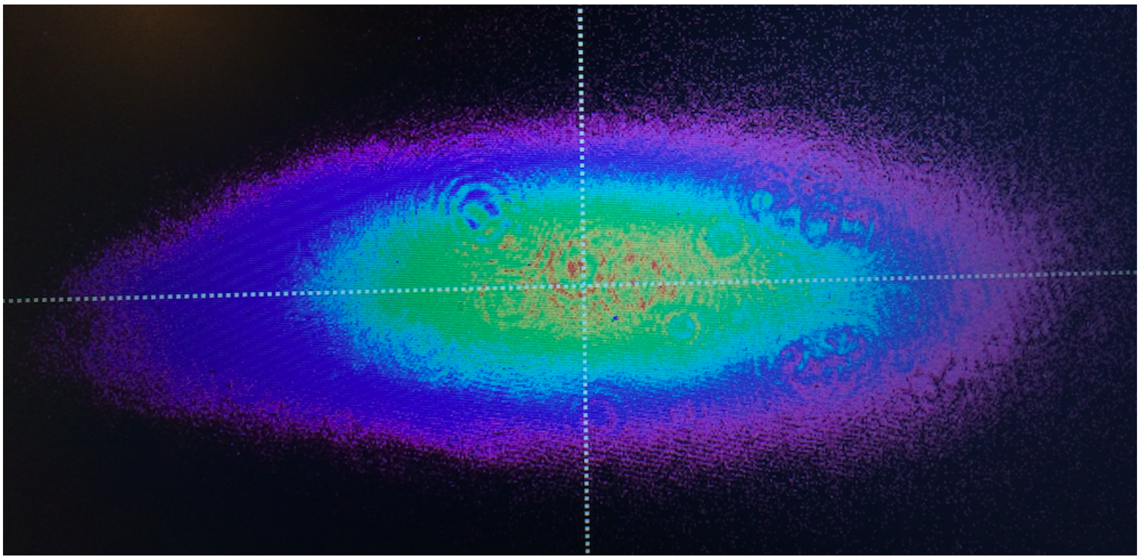

Figure 71: A picture of the beam profile of the beam coupled into the laser. Using a telescope made up of cylindrical lenses, the desired 1:3 elliptical beam profile was acheived. The beam was later focused into the MOPA using a f = 6.24 mm lens.

possible to do rough alignment by overlapping the light from the MOPA with the seed laser. This is explicitly shown in Fig. 72b using a IR-viewer.

The required input beam size results in a Rayleigh length of roughly 6 μm, making the input extremely sensitive to the distance from the focusing lens to the input aperture. The setup is shown in Fig. 72a and 72b. The two metal cylinders each hold a lens for incoupling and outcoupling of the light. The system was aligned by observing the diffraction from the small black rectangle that holds the TA-Chip, see Fig. 70. An IR-viewer was used to observe the ASE from the chip. The seed was then overlapped with the ASE. When a visible overlap was achieved, a power meter was used to measure the output power and maximizing this though aligment. Fine-alignment was made using micrometers screws adjusting the in-coupling lense. Damage can be caused to the amplifier if it runs at high currents without a seed for long periods of time. Therefore breaks had to be included where the MOPA power was lowered and the ASE was turned off in order to prevent damage to the chip.

In order to quantitavely determine the location of the waist, a setup designed to explicitly measure the size and location of the waist was introduced. An thin razorblade was attached verically to a rod that could be moved back and forth through the beam while a photodiode monitored the power. Once the razorblade started to block the beam, the razor blade was moved in steps of approximately 1 μm, while the recorded power on the PD was monitored. The output yields an integrated Gaussian, that could be fitted in order to determine the waist. The measurement was carried out multiple times in order to determine the location of the waist. As the beam was focused down to approximately 1.4 μm, the measurement was diffraction limited, meaning that the resolution of the measurement was limited. The waist measure gave a waist size of 2.89 $\pm$0.06 μm, indicating that the beam should be match the input aperture. The fit and data is shown in Fig. 73.

The MOPA had to be temperature stabilized in order to work properly. The manufacturer

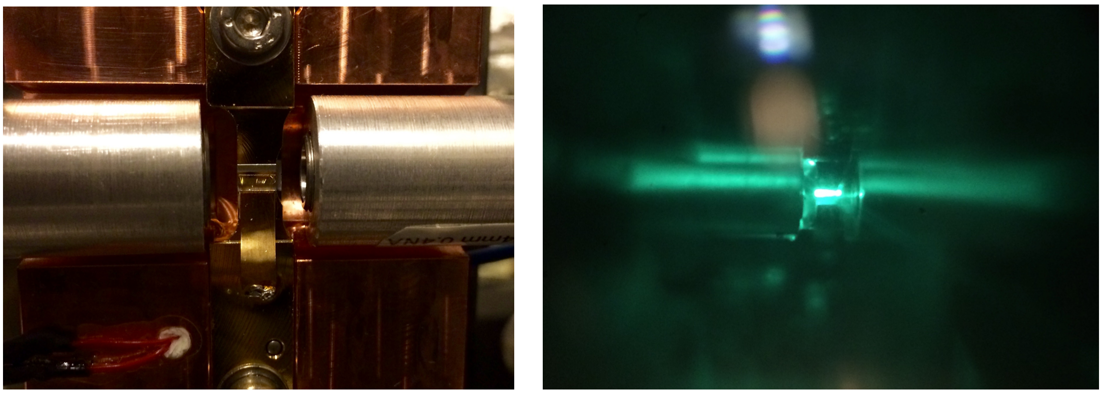

(a) (b)

Figure 72: a) The TA-chip placed in between the in-coupling and out-coupling lenses. The in-coupling lens is adjusted using a high precision micrometer mount to ensure the best coupling efficiency. b) The TA-Chip and focusing lenses as seen through the IR-viewer. The light across the chip stem from ASE. Rough aligment was done by visually overlapping the seed laser and the ASE. Once rough alignment had been acheived, fine adjustments were made using the built-in micrometer screws on the lense mount that covered a range of 300 μm in both the x-, y-, and z-direction

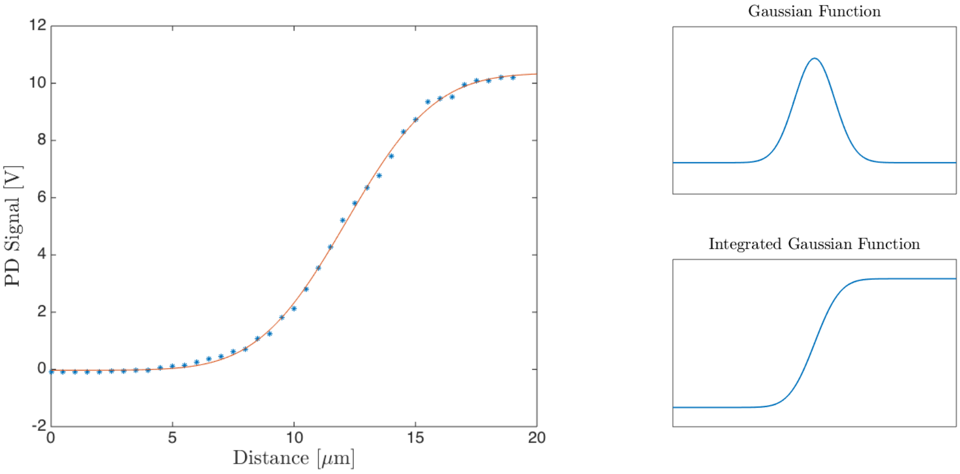

(a) (b)

Figure 73: a) The data obtained from direct measurement of the waist size. The blue dots show the data, and the orange curve show the fit. The fit gave a waist size of 2.89 ±0.06 μm. This should be reasonalble for coupling light into the cavity. The measurement is diffraction limited. b) a plot showing a Gaussian function and an integrated Gaussian.

had succesfully acheived an ouput of 1.5 W at a temperature of 20 °C. Therefore, the MOPA was placed in a large copper block to work as a heat sink. The temperature was controlled using a Thorlabs TEC2000 and a peltier element. Unfortunately, the peltier element could not keep up with the heat dissipating in the copper once coupling was acheived, and whole system would drift every time power was coupled into the MOPA. Therefore, no amplification was seen despite coupling 40% through the MOPA. For future usage, a faster and more robust temperature control system should be included in order to compensate for the heat that arises when the power is coupled through the MOPA.

7.4 Resonance Circuit for the EOM

In order to boost the NICE-OHMS signal, a resonance circuit was designed and tested a resonance circuit, also known as a tank circuit. A tank circuit can be used to move the corner frequency of a circuit. The tank circuit was designed to effectively amplify the voltage applied to the EOM, and thereby increase the modulation index δ.

As mentioned in Sec. 3.2, the EOM works by having a crystal placed inbetween two metal plates working as a capacitor. Therefore, if one takes into account the 50 Ω resitance in the wires, the EOM will work as a low pass filter. The capacitance of the EOM used in this work was 12.4 pF. This gives a corner frequency of 256 MHz, i.e., frequencies higher than 256 MHz are attenuated.

As the experiment was carried out at around 500 MHz, this meant that the generated sidebands used in the NICE-OHMS detection scheme was very small. Therefore a tank circuit was designed in order to boost the voltage across the crystal in the EOM at higher frequencies and thereby increase the modulation index. This will result in a larger sideband amplitude. The initial design was very simple and is summarized along with the measured improvement in peak height in Fig. 74.

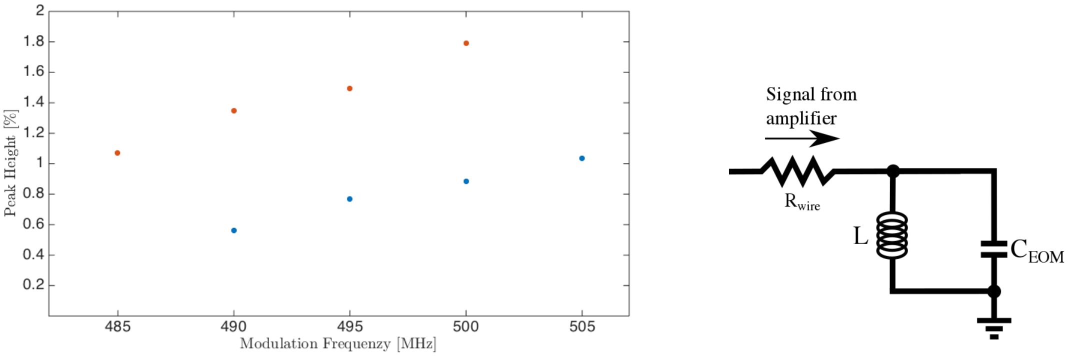

(a) Sideband height improvement

(b) Circuit design

Figure 74: Improvement of sideband height in the vincinity of 500 MHz (a) alongside the simple tank circuit design (b). The inductor had an inductance of 8.9 nH, while the capacitance of the EOM was 12.4 pF. The circuit roughly improved the sideband height by a factor of two.

The improvement of the signal at 500 MHz did however come at a price. When the circuit was used the sidebands at lower frequencies, i.e., the ones used for locking the cavity, were extinguished. Therefore the tank circuit could not be used in practice. A proposal for a future circuit design is shown in Fig. 75. The Bode plot of this design is shown in Fig. 76.

The Bode plot show gain both in both the lower ∼ 10-20 MHz regime, and in the ∼ 500 MHz regime. This would allow for generating a PDH locking signal and a NICE-OHMS signal simultaneously.

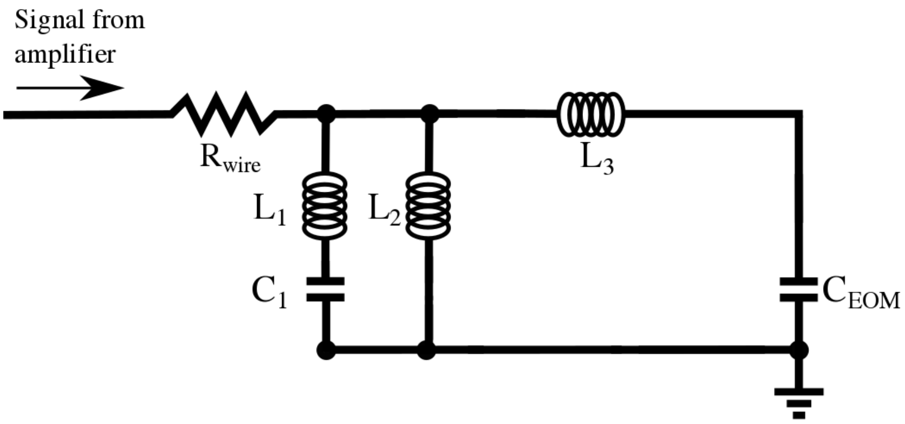

Figure 75: Proposal for a new tank circuit design that should support frequencies in the regime used for PDH cavity locking and in the NICE-OHMS at the same time. A simulated Bodeplot is shown in Fig.76.

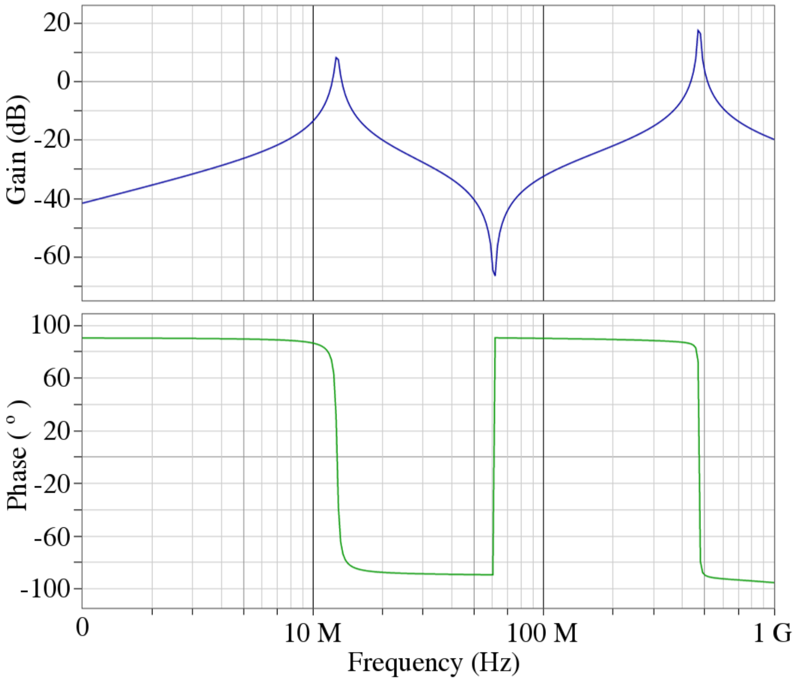

Figure 76: A simulated Bodeplot of the circuit desing shown in Fig. 75. The component values used are: $R_1 = 50\ \Omega$, $L_1 = 1$ nH, $L_2 = 22$ nH, $L_3 = 8.2$ nH, $C_1 = 6.8$ nF and $C_{EOM} = 12.4$ pF. The position of the peaks in the Bodeplot can be varied by changing the component values. Due to the peaks being quite narrow, this circuit can only be implemented once the exact frequencies intended for NICE-OHMS and PDH locking is determined.

8 Conclusion

Despite the lack of any concrete results from the NICE-OHMS measurements, the experiments performed has paved the way for the future realization of a working, thermal molecular clock.

The setup itself has been improved greatly, as the laser has been stabilized and the new sample seemingly is pure, and should deliver results in the near future.

The experiment performed on iodine in this kind of setup is, moreover, the first to be demonstrated in the world. The setup has allowed for measurements being performed at much lower pressures than in conventionel experiments with sample lengths of a comparable size as the one used in, e.g., [7]. The reduction in vapor pressure has served to reduce broadening effects. Though no hyperfine transitions were present in the data collected due to a contaminated sample, it is fair to conclude that the realization of the setup itself is a success.

The design and realization of the beam expander cavity has also been a world first in terms of designing such a compact setup supporting a waist that is a factor of 10 larger than in conventional cavities. The great compliance of the predicted finesse and the finesse measured further emphasize the success of the realization of the beam expander cavity. The current results are promising, as a future beam expander cavity should be able to support an even higher finesse, when better optical components are used.

The characterization of the cavity-cell system has set the foundation for future optimization. The current limitations stem from the poor incoupling, which can be improved by optimizing the impedance matching of the cavity-cell system. It is however recommended that a new sample cell is bought. The degrading in optical quality sets the current limitation to the finesse achievable in the impedance matched cavity.

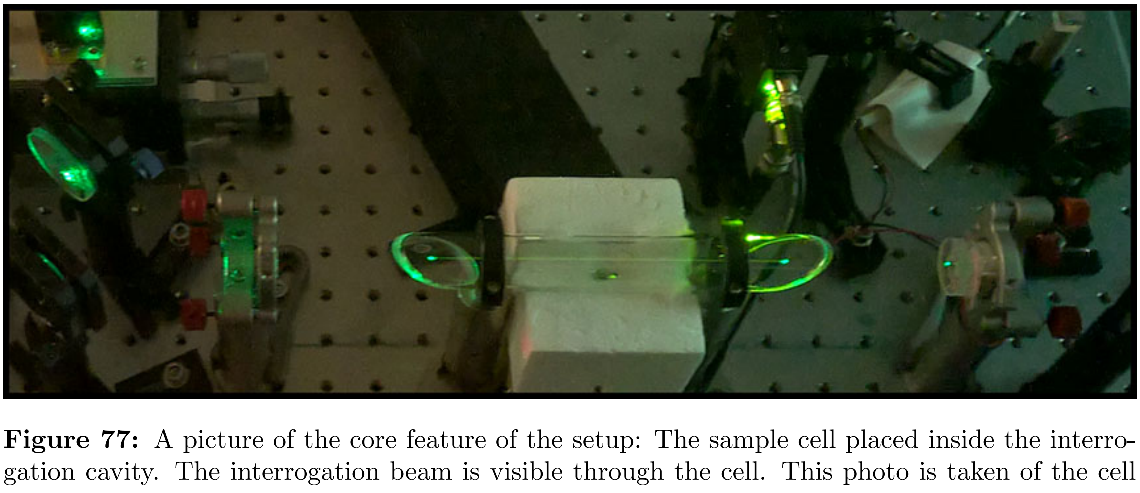

Figure 77: A picture of the core feature of the setup: The sample cell placed inside the interrogation cavity. The interrogation beam is visible through the cell. This photo is taken of the cell with Sample 1, i.e., before the optical quality of the cell was degraded. The cell is sitting on top of a block of styrofoam, that covers the cooling tower used to control the coldfinger temperature.

References

[1] Lisheng Chen, *High-Precision Spectroscopy of Molecular Iodine: From Optical Frequency Standards to Global Descriptions of Hyperfine Interactions and Associated Electronic Structure*, PhD Thesis

[2] Jun Ye and Theresa W. Lynn, *Applications of Optical Cavities in Modern Atomic, Molecular, and Optical Physics*, ADVANCES IN ATOMIC, MOLECULAR, AND OPTICAL PHYSICS, VOL. 49

[3] www.bipm.org, *Recommended Values of Standard Frequencies for Applications Including the Practical Realizations of the Metre and Secondary Representations of the Defition of the Second*

[4] Mohinder S. Grewal, Lawrence R. Weill, Angus P. Andrews, *Global Positioning Systems, Inertial Navigation, and Integration*

[5] B. Argence, H. Halloin, O. Jeannin, P. Prat, O. Turazza, E. de Vismes, G. Auger, and E. Plagnol, *Molecular laser stabilization at low frequencies for the LISA mission*, PHYSICAL REVIEW D 81, 082002 (2010)

[6] A. Goncharov, A. Amy-Klein, O. Lopez, F. du Burck, C. Chardonnet, *Absolute frequency measurement of the iodine-stabilized Ar laser at 514.6 nm using a femtosecond optical frequency comb*, Appl. Phys. B 78, 725–731 (2004).

[7] R. J. Jones, Wang-Yau Cheng, K. W. Holman, Lisheng Chen, John L. Hall, and Jun Ye, *Absolute-frequency measurement of the iodine-based length standard at 514.67 nm*, Appl. Phys. B 74, 597–601 (2002)

[8] E. J. Zang et al, *Realization of four-pass I2 absorption cell in 532 nm frequency standard*, IEEE Trans. Instrum. Meas. 56 673-676 (2007)

[9] Peter W. Molonni and Joseph H. Eberly, *Laser Physics*, Wiley, 2010. ISBN: 9780470409701

[10] Fritz Riele *Frequency Standards - Basics and Applications*, Wiley, 2004: ISBN 3527402306

[11] S. A. Schäffer, S. S. Adsersen, B. T. R. Christensen, and J. W. Thomsen, *Large Waist Cavity for Ultra-narrow Transition Spectroscopy*, in IEEE proceedings of IFCS-EFTF, IEEE, 2015.

[12] W. DemtrÖeder , *Laser Spectroscopy vol. 1: Basic Principles, Fourth Edition*, Springer 2008. ISBN: ISBN 978-3-540-73415-4.

[13] Wagner Nagourney: *Quantum Electronics for Atomic Physics and Telecommunication (Secon Edition)*, Oxford University Press, 2014. ISBN: 978-0-19-966548-8.

[14] John Bechhoefer: *Feedback for physicists: A tutorial essay on control*, Rev. Mod. Phys. 77, 783 (2005)

[15] Susanne Picard et. al: *Comparison of* $127I_2$*-stabilized frequency-doubled Nd:YAG lasers at the Bureau International des Poids et Mesures*, 2003 Optical Society of America OCIS codes: 120.0120, 300.6460, 300.1030, 140.3500.

[16] Karsten Rottwitt and Peter Tidemand-Lichtenberg, *Nonlinear Optics - Principles and Applications*, CRC Press, 2015. ISBN: 978-1-4665-6583-8.

[17] Jean-Pierre Wallerand, Lennart Robertsson, Long-Sheng Ma and Massimo Zucco: *Absolute frequency measurement of molecular iodine lines at 514.7 nm, interrogated by a frequency-doubled Yb-doped fibre laser* Metrologia 43 (2006) 294–298.

[18] Jan W. Thomsen, *A First Course in Optics*, Lecture Notes

[19] Jesper Lægsgaard *Introduction to dielectric wave guides*, lecture notes

[20] David R. Lide, *Handbook of Chemistry and Physics 84th Edition*, CRC Press, 2003. ISBN: 0-8493-0484-9.

[21] B.H. Bransden & C.J. Joachain, *Physics of Atoms and Molecules, 2nd Edition*, Pearson Education, 2003. ISBN: 978-0-582-35692-4.

[22] Warren Nagourney *Quantum Electronics for Atomic Physics and Telecommunication*,Oxford University Press, 2014. ISBN: 978-0-19-966548-8.

[23] Christopher J. Foot, *Atomic Physics*, Oxford University Press, 2005. ISBN: 978-0-19-850695-9.

[24] T. Kessler, C. Hagemann, C. Grebing, T. Legero, U. Sterr, F. Riehle, M. J. Martin, L. Chen & J. Ye *A sub-40-mHz-linewidth laser based on a silicon single-crystal optical cavity*, Nature Photonics 6, 2012.

[25] Theresa A . Maldonado, *Handbook of Optics Ch. 13: Electro Optic Modulators*

[26] C. W. Chou, D. B. Hume, J. C. J. Koelemeij, D. J. Wineland, and T. Rosenband *Frequency Comparison of Two High-Accuracy* Al^+ *Optical Clocks*, PRL 104, 070802 (2010).

[27] B. P. Abbott et al.*Observation of Gravitational Waves from a Binary Black Hole Merger*, PRL 116, 061102 (2016).

[28] S. Droste, F. Ozimek, Th. Udem, K. Predehl, T. W. Hänsch, H. Schnatz, G. Grosche, and R. Holzwarth1,: *Optical-Frequency Transfer over a Single-Span 1840 km Fiber Link*, PRL 111, 110801 (2013)

[29] Stefan Alaric Schäffer: *Studies of Collective Effects in Atomic Strontium*, Master Thesis

[30] B. T. R. Christensen, M. R. Henriksen, S. A. Schäffer, P.G. Westergaard, J. Ye, M. J. Holland, and J. W. Thomsen*Non-linear Spectroscopy of Sr Atoms in an Optical Cavity for Laser Stabilization*

[31] *https://techcrunch.com/2016/02/05/new-air-force-satellites-launched-to-improve-gps/*

A Cavity Transmission and Hermite-Gaussian Modes

Cavity Transmission: In Fig. 10 in Sec. 3.1, a simple representation of an optical cavity is made. Here, two flat mirrors, each with reflectance and transmission coeffiecients r_1 , t_1 and r_2, t_2 for mirror 1 and 2 respectively. An electrical field denoted E_0 is coupled into the cavity, where it is reflected back and forth. The field transmitted by the cavity can be expressed by collecting the terms shown on the RHS of mirror 2. By including the phase factor obtained at each roundtrip, $\exp(-ikr) = \exp(-i2L\omega/c)$:

$$\begin{aligned} E_T &= E_0 t_1 t_2 e^{-i\omega L/c} + E_0 t_1 r_2 r_1 t_2 e^{-i\omega 3L/c} + E_0 t_1 r_2^2 r_1^2 t_2 e^{-i\omega 5L/c} + ... \\ &= E_0 e^{-i\omega L/c} \left(1 + t_1 t_2 + t_1 r_2 r_1 t_2 e^{-i\omega 2L/c} + t_1 r_2^2 r_1^2 t_2 e^{-i\omega 4L/c} + ...+\right). \end{aligned} \tag{A.1}$$

This can be re-written using the following geometrical series:

$$\sum_{i=0}^{\infty} q^i = \frac{1}{1-q} \tag{A.2}$$

q is identified as $q = r_1 r_2 e^{-i\omega 2L/c}$. Substituting intor eq. (A.1), we find:

$$E_T = E_0 \frac{t_1 t_2 e^{-i\omega L/c}}{1 - r_1 r_2 e^{-i\omega 2L/c}} \tag{A.3}$$

Multiplying numerator and denominator in eq. (A.3) with the complex conjugated denominator, we find:

$$\begin{aligned} E_T &= E_0 \frac{t_1 t_2 e^{-i\omega L/c}}{1 - r_1 r_2 e^{-i\omega 2L/c}} \frac{1 - r_1 r_2 e^{i\omega 2L/c}}{1 - r_1 r_2 e^{i\omega 2L/c}} \\ &= E_0 \frac{t_1 t_2 \left(e^{-i\omega L/c} - r_1 r_2 e^{i\omega L/c}\right)}{1 + r_1^2 r_2^2 - 2 r_1 r_2 \cos(\omega 2L/c)}. \end{aligned} \tag{A.4}$$

This is exactly eq. (3.1).

Hermite-Gaussian modes constitute a different solution to the paraxial waveequation presented in Sec. 3.1. Again, a trial solution to the equation is given:

$$\varepsilon = A g \left[\frac{x}{w(z)}\right] h \left[\frac{y}{w(z)}\right] e^{iP(z)} e^{-k(x^2+y^2)/2q(z)}. \tag{A.5}$$

Two independent variables can be introduced as:

$$\begin{aligned} \xi &= \frac{x}{w(z)} \\ \eta &= \frac{y}{w(z)}. \end{aligned} \tag{A.6}$$

From this, the partial derivatives of g and h can be rewritten

$$\begin{aligned} \frac{\partial g}{\partial x} &= \frac{dg}{d\xi} \frac{\partial \xi}{\partial x} = \frac{1}{w(z)} \frac{dg}{d\xi} \\ \frac{\partial^2 g}{\partial x^2} &= \frac{1}{w(z)}{}^2 \frac{d^2 g}{d\xi^2} \\ \frac{\partial g}{\partial z} &= \frac{dg}{d\xi} \frac{\partial \xi}{\partial z} = \frac{-x}{w(z)^2} \frac{dw}{dz} \frac{dg}{d\xi}, \end{aligned} \tag{A.7}$$

with a similar derivation for $h(\eta)$. Plugging this into the paraxial wave equation, eq. (3.7), we get:

$$\frac{1}{g(\xi)}\left(\frac{d^2g}{d\xi^2}-4\xi\frac{dg}{d\xi}\right)+\frac{1}{h(\eta)}\left(\frac{d^2h}{d\eta^2}-4\eta\frac{dh}{d\eta}\right)+\left(\frac{2ik}{q(z)}-2k\frac{dP(z)}{dz}\right)w(z)^2=0. \tag{A.8}$$

Each term on the LHS of the equation depends on individual parameters, and the equation thus only be fulfilled if each term is separately constant. In [9], the solutions to $g(\xi)$ and $h(\eta)$ is found to be:

$$\begin{aligned} g[\xi] &= H_m\left[\xi\right] \\ h(\eta) &= H_n\left[\eta\right]. \end{aligned} \tag{A.9}$$

$H_{i\in n,m}$ are the Hermite polynomials of the i'th order. The solution to $P(z)$ is found to be [9]:

$$P(z)=i\ln\left(\sqrt{1+\frac{z^2}{z_0^2}}\right)-(m+n+1)\tan^{-1}(z/z_0). \tag{A.10}$$

Using this, the solution to the paraxial wave equation reads:

$$\begin{aligned} E_{m,n}(x,y,z) = {} & \frac{Aw_0}{w(z)}H_m\left[\sqrt{2}\frac{x}{w(z)}\right]H_n\left[\sqrt{2}\frac{y}{w(z)}\right]e^{i\left[kz-(m+n+1)\tan^{-1}(z/z_0)\right]} \\ & \times e^{ik(x^2+y^2)/2R(z)}e^{-(x^2+y^2)/w^2(z)}, \end{aligned} \tag{A.11}$$

$E_{m,n}$ is the *order* of the Hermite-Gaussian mode and A is the field amplitude and H_m are Hermetian polynomials of m'th order. The orders of the mode will have different spatial field profiles and be separated in frequency. This is again equivalent to playing different musical notes on a guitar string, but this time not being separated by one octave or one FSR. The frequency spacing of the differen modes is given by:

$$v_{qmn}=\frac{c}{2L}\left[q+\frac{1}{\pi}(m+n+1)\cos^{-}1\left(\sqrt{(1-\frac{L}{R_2})(1-\frac{L}{R_2})}\right)\right] \tag{A.12}$$

If we let z = 0 in eq. (A.11), we find that $w(z)=w_0$, $\tan^{-1}(0)=0$ and $R(0)=\infty$, reducing the expression to

$$E_{m,n}(x,y,z=0)=AH_m\left[\sqrt{2}\frac{x}{w_0}\right]H_n\left[\sqrt{2}\frac{y}{w_0}\right]e^{-(x^2+y^2)/w_0^2} \tag{A.13}$$

In Fig. 78 the first four TEM-modes of a Gaussian beam described by A.13 is plotted. TEM_{00} is equivalent to the fundamental E_{00} mode. The example of a cavity output shown in Fig. 12 has assumed that only the fundamental E_{00} mode is present. If other modes are supported by the cavity, i.e., the cavity is not aligned well, more fringes will show up in the cavity transmission. Cavity alignment and cavity mode matching is discussed in the following section.

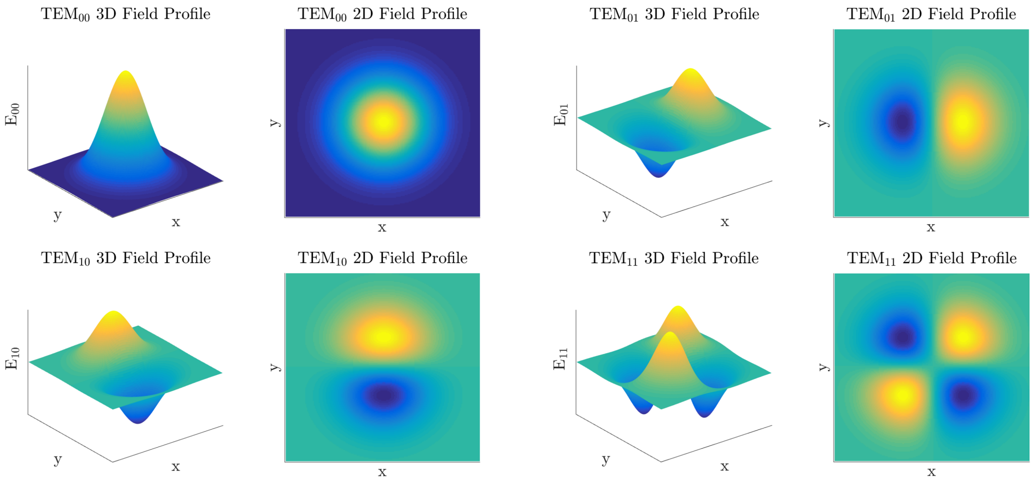

Figure 78: Different example of TEM$_{\mathrm{m,n}}$ field profiles. The first four modes of a Gaussian beam. The fundamental mode, in the top left corner, has an circular intensity profile. When aligning a cavity, rough alignment can be acheived by visually looking for the circular mode. The TEM$_{01}$ and TEM$_{10}$ modes show up as two elliptical dots, where as the TEM$_{11}$ mode show up as four small dots. These were directly observed in Fig. 21.

B Second Harmonic Generation

Second harmonic generation is a second order nonlinear effect where light passes through a nonlinear medium, and two identical photons are combined to generate a new photon at twice the energy, i.e., twice the frequency thus at half the wavelength. Overall, nonlinar effects can be described as special cases where the presence of a field modulate the field itself, i.e., the induced polarization works as a source term. The theory behind SHG is thoroughly described in [16] and [9], and only the basic characteristics used in the experimental setup is presented in this thesis.

The phase matching parameter is introduced in [16]:

$$\Delta k = k_3 - (k_1 + k_2) \xrightarrow{SHG} k_2 - 2k_1, \tag{B.1}$$

where k_2 is the k-vector of the second harmonic, and k_1 is the k-vector of the input field. From this, the nonlinear conversion efficiency as function of crystal lenght can be derived, [16]:

$$\left| \int_0^L e^{(-i\Delta k z)} dz \right|^2 = L^2 \frac{\sin^2(\Delta k L/2)}{(\Delta k L/2)^2}. \tag{B.2}$$

This is holds true for small Δk and small L ($\approx \mu m$). The expression in eq. (B.2) is shown in Fig. 79.

The *coherence length* $l_c = 2\pi/\Delta k$ is defined as the length at which a 2π phase shift occurs between the induced polarization and the real field. When the field has propagated half a coherence length through the crystal, back conversion will happen instead of continous power build-up [16]. This is due to the phase matching condition no longer being fulfilled, and the induced polarization and the real field gets out of phase and cancel each other.

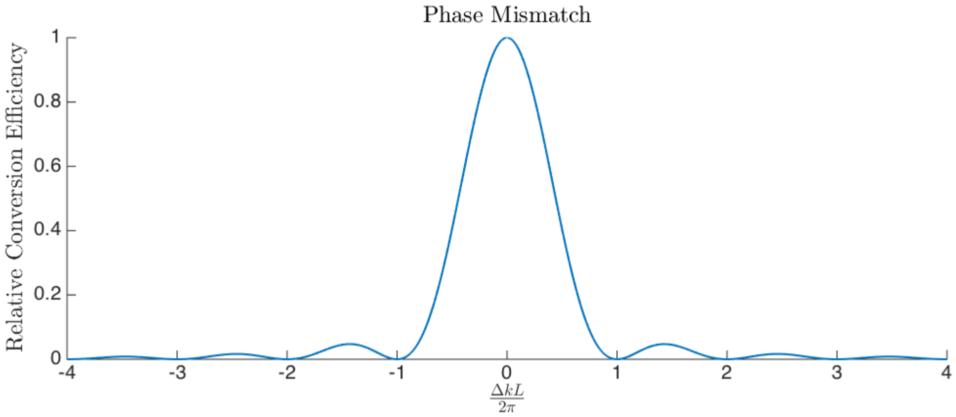

Figure 79: Phase matching in SHG crystal.

The crysal has a macroscopic length (15mm), i.e., L > l_{coh}. Thus, in order to suppress the cancellation, a periodicity of length Λ is introduced in the crystal, such that the mismatch parameter is rewritten as:

$$\begin{aligned}\Delta k &= k_3 - k_1 - k_2 \pm k_{qpm} \xrightarrow{SHG} k_2 - 2k_1 \pm k_{qpm}\\ k_{qpm} &= \frac{2\pi}{\Lambda}.\end{aligned} \tag{B.3}$$

k_{qpm} is known as the quasi-phasematching parameter. The periodicity serves to counteract the back conversion and secure continous power build-up.

The power of the second harmonic is dependent of the field strength of the fundamental field. The scalar equation for a single component E of the electric field is [9]:

$$\nabla^2 E - \frac{1}{c^2}\frac{\partial^2 E}{\partial t^2} = \mu_0 \frac{\partial^2 P}{\partial t}, \tag{B.4}$$

where P is the induced polarization. E is assumed to be a plane, monochromatic wave:

$$E = \frac{1}{2}\left[E_{2\omega} e^{-i(2\omega t - k_{2\omega} z)} + c.c.\right]. \tag{B.5}$$

$k_{2\omega}$ is the k-vektor at 2ω. Applying SVEA (slowly varying envelope amplitude), the LHS of eq. (B.4) reads:

$$\nabla^2 E - \frac{1}{c^2}\frac{\partial^2 E}{\partial t^2} \approx \left[ik_{2\omega}\frac{dE_{2\omega}}{dz} - \frac{1}{2}\left(k_{2\omega}^2 - \frac{4\omega^2}{c^2}\right)E_2\right] e^{i(2\omega t - k_{2\omega} z)}. \tag{B.6}$$

The polarization on the RHS of eq. (B.4) contains both linear- and nonlinear terms:

$$\begin{aligned}P &= \frac{1}{2}\left[P_{2\omega}^{(L)} e^{-i(2\omega t - k_{2\omega} z)} + P_{2\omega}^{(NL)e^{-2i(\omega t - k_\omega z)}} + c.c.\right]\\ \Rightarrow \mu_0 \frac{\partial^2 P}{\partial t^2} &= -2\mu_0\omega^2\left[P_{2\omega}^{(L)} e^{-i(2\omega t - k_{2\omega} z)} + P_{2\omega}^{(NL)e^{-2i(\omega t - k_\omega z)}} + c.c.\right].\end{aligned} \tag{B.7}$$

Stitching the whole equation together it reads:

$$\left[ik_{2\omega}\frac{dE_{2\omega}}{dz} - \frac{1}{2}\left(k_{2\omega}^2 - \frac{4\omega^2}{c^2}\right)E_2\right]e^{i(2\omega t - k_{2\omega}z)} = -2\mu_0\omega^2 P_{(2\omega)}^{(L)}e^{-i(2\omega t - k_{2\omega}z)} \\ -2\mu_0\omega^2 P_{(2\omega)}^{(NL)}e^{-i2(\omega t - k_\omega z)} \tag{B.8}$$

Re-writing $P_{2\omega}^{(L)}$ and $k_{2\omega}^2$ in terms of the linear susceptibility $\chi(2\omega)$, the expression reduces to:

$$\frac{dE_{2\omega}}{dz} = i\omega\sqrt{\frac{\mu_0}{\epsilon_{2\omega}}}P_{2\omega}^{(NL)}e^{i\Delta kz} \tag{B.9}$$

$e^{i\Delta kz}$ and Δk are expressions familiar from eq. (B.2). Exploiting the fact that the induced nonlinear polarization is can be expressed as:

$$\begin{aligned} P_{2\omega}^{(NL)} &= K(-2\omega;,\omega,\omega)\chi^{(2)}(-2\omega;,\omega,\omega)E_\omega^2 \\ &= \frac{1}{2}\chi^{(2)}(-2\omega;,\omega,\omega)E_\omega^2 \\ &= \bar{d}E_\omega^2, \end{aligned} \tag{B.10}$$

where we have used that $K(-2\omega;,\omega,\omega) = 1/2$ for SHG [16], and $\chi^{(2)}(-2\omega;,\omega,\omega)$ is the second order nonlinear susceptibility. We thus arrive at the final differential equation to be solved:

$$\frac{d^2E_{2\omega}}{dz^2} = i\omega\sqrt{\frac{\mu_0}{\epsilon 2\omega}}\bar{d}E_\omega^2 e^{(i\Delta kz)}. \tag{B.11}$$

Assuming little depletion in the input field, i.e., the field oscillating at ω does not lose amplitude while propagatring through the meadium such that $E_\omega(0) \approx E_\omega(z = L)$, and that $E_{2\omega}(z = 0) = 0$, the equation is solved:

$$E_{2\omega}(z) = i\omega\sqrt{\frac{\mu_0}{\epsilon_{2\omega}}}\bar{d}E_\omega^2(0)e^{i\Delta kz/2}\left(z\frac{\sin^2(\Delta kz/2)}{\Delta kz/2}\right). \tag{B.12}$$

The measurable quantity is however not the field inside the medium, but rather the intensity or power of the generated light. To evaluate this expression against something measurable, the power output after propagation distance L is given by:

$$\begin{aligned} |E_{2\omega}|^2 &= \frac{\mu_0\omega\bar{d}^2}{\epsilon_{2\omega}}|E_\omega(0)|^4\left(L^2\frac{\sin^2(\Delta kL/2)}{(\Delta kL/2)^2}\right) \\ &= \gamma\,|E_\omega|^4. \end{aligned} \tag{B.13}$$

In the second line all constants are collected in to one single constant, γ, and perfect phase matching is assumed, i.e., $L^2\frac{\sin^2(\Delta kL/2)}{(\Delta kL/2)^2} = 1$, see Fig. 79.